THE UNIVERSITY OF QUEENSLAND

AUSTRALIA

Experimental Study of Hypersonic Wing/Fin Root Heating at Mach 8

Mr Arman Schwarz

BEng Hons 1A, MSc, GradCert

A thesis submitted for the degree of Master of Philosophy at

The University of Queensland in 2014

School of Mechanical and Mining Engineering

Abstract

The junction between wings or fins and the body of supersonic flight vehicles generate complex vortical structures and shock impingements. In hypersonic flight this interaction can lead to high localised heating rates. While the general topology of this flow has been established, confidence in the heating rates predicted by computational simulation is not high. This study utilises a dense set of heat transfer measurements on a model consisting of a flat plate and a cylinder with an adjustable sweep angle to help better understand and quantify flow features and heating rates on a swept protruding wing in hypersonic flight. Tests were conducted in the T4 shock tunnel facility at the University of Queensland Centre for Hypersonics at conditions simulating Mach 8 flight at 30km altitude. The resulting data is intended to help better understand flow topologies over wing-root junctions at hypersonic speeds, where relatively little testing has been conducted.

A series of tests were conducted at both “low” and “high” pressure conditions, representing approximate atmospheric conditions at Mach 8 (total enthalpy ca. 3 MJ/kg) and a higher pressure case respectively, the latter being tested with the intention of inducing turbulence and measuring the effects of higher enthalpy and total pressure (a flow trip was later designed to ensure transition of the upstream boundary layer). The present study succeeded in correlating heating rates to empirical equations in the flat plate region upstream of the interaction, where the flow could be modelled as a simple flat plate of known Reynolds number.

Correlation to theory, where applicable, was good. The use of a trip successfully caused flow to consistently transition from laminar to turbulent. Schlieren images were used to successfully match measured heating peaks with observed shock impingements.

The present work was able to demonstrate the effectiveness of a trip in triggering turbulence. It demonstrated a correlation between flat plate heating and sweep angle, as well as providing a profile of heating rates along the centreline of a wing protruding from a wing root. Schlieren images added further insight by demonstrating positive the relationship between recirculation region size and peak heating rates.

Future work should focus on obtaining more reliable data for the scenarios studied herein, particularly on the wing, where peak heating is expected to significantly exceed heating rates observed on the flat plate.

Declaration by the Author

This thesis is composed of my original work, and contains no material previously published or written by another person except where due reference has been made in the text. I have clearly stated the contribution by others to jointly-authored works that I have included in my thesis.

I have clearly stated the contribution of others to my thesis as a whole, including statistical assistance, survey design, data analysis, significant technical procedures, professional editorial advice, and any other original research work used or reported in my thesis. The content of my thesis is the result of work I have carried out since the commencement of my research higher degree candidature and does not include a substantial part of work that has been submitted to qualify for the award of any other degree or diploma in any university or other tertiary institution. I have clearly stated which parts of my thesis, if any, have been submitted to qualify for another award.

I acknowledge that an electronic copy of my thesis must be lodged with the University Library and, subject to the General Award Rules of The University of Queensland, immediately made available for research and study in accordance with the *Copyright Act 1968*.

I acknowledge that copyright of all material contained in my thesis resides with the copyright holder(s) of that material. Where appropriate I have obtained copyright permission from the copyright holder to reproduce material in this thesis.

Publications during candidature

No publications.

Publications included in this thesis

No publications included.

Contributions by others to the thesis

No contributions by others.

Statement of parts of the thesis submitted to qualify for the award of another degree

None.

Acknowledgments

This thesis would not have been possible without, foremost, the support of my supervisors, Professor Michael Smart and Professor Richard Morgan. I thank them for their guidance, support and eagerness to dispense with their knowledge. I am indebted to Erich Walth, who developed the initial designs for the model on which my work was based.

I would also like to extend my sincere thanks to our T4 Technician, Keith Hitchcock, whose craftsmanship, patience and experience were pivotal to every step of the campaign. I am thankful also to Barry Allsop and Brian Loughrey, whose guidance and assistance in designing the sensors on the model were invaluable.

I would like to extend my sincere thanks to my colleagues at the Centre for Hypersonics, in no particular order; Luke Doherty, Dylan Wise, Kevin Basore, Philippe Lorrain and Hadas Porat, all of whom dispensed their valuable time, knowledge and experience without hesitation.

Finally, a deserved thanks goes to Stefan Brieschenk for devoting many afternoons to setting up the optics system and producing the schlieren images.

Keywords

Wing root, heat transfer, hypersonic, turbulence

Australian and New Zealand Standard Research Classifications (ANZSRC)

090107 Hypersonic Propulsion and Hypersonic Aerodynamics, 100%

Fields of Research (FoR) Classification

FoR code: 0901 Aerospace Engineering, 100 %

Table of Contents

List of Figures

List of Tables

List of Symbols

Variables

α	Blassius skin friction coefficient (0.0228 unless specified otherwise)
c_f	Local skin friction coefficient
C_H	Stanton Number
C_P	Constant-pressure specific heat (1004.9 $J.kg^{-1}.K^{-1}$ unless specified otherwise)
γ	Specific heat ratio of air (1.4 unless specified otherwise)
h	Enthalpy ($J.kg^{-1}$)
h_D	Atomic dissociation energy times atom mass fraction in external flow
k	Heat transfer coefficient ($q_w/(T_{aw} - T_w)$)
κ	Thermal conductivity ($W.m^{-1}.K^{-1}$)
l	Reference length (m)
Λ	Sweep angle (degrees)
M	Mach Number
μ	Dynamic viscosity ($Pa.s$)
n	Blassius skin friction exponent (4 unless specified otherwise)
ν	Kinematic viscosity ($m^2.s^{-1}$)
p	Pressure (Pa)
q	Heat flux ($W.m^{-2}$)
Pr	Prandtl Number
Re	Reynolds Number
ρ	Density ($kg.m^{-3}$)
T	Temperature (K)
u	Velocity ($m.s^{-1}$)
x	Spanwise position (m)

Subscripts

aw	Adiabatic wall conditions
e	Boundary layer edge
∞	Free-stream conditions
0	Isentropic stagnation conditions
r	Reference condition (wall condition unless specified otherwise)
s	Stagnation point
w	Wall conditions

CHAPTER 1

Introduction

Heating is arguably the most pervasive engineering problem in the field of hypersonics, and yet it remains largely a poorly understood physical phenomenon, particularly in more complex flow interactions. This is particularly true for flow interactions at the junction between wings and vehicle bodies, and at the root of struts and fins where boundary layers, vortical flow structures and bow shocks can interact to form complex flow topologies. At supersonic speed these flows begin to have a large impact on aerodynamic loads, and at hypersonic speeds localized regions of high heating can also be produced, ultimately becoming a critical design consideration in fully hypersonic flight regimes.

The first major attempt to realise manned hypersonic flight was probably the United States' X-15 program of the 1950s and 1960s, which heralded the age of manned space flight but also brought to light several limitations in the materials science and engineering practices of that time. It quickly became evident that it would be heating, not mechanical load (as was the hurdle for a previous generation of engineers attempting to break the sound barrier) that would limit our extended access to hypersonic flight regimes.

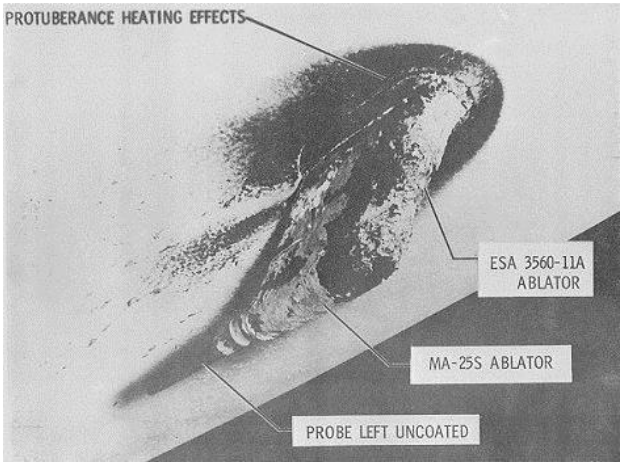

Figure 1-1: Photograph of a fin-shaped telemetry antenna on the body of the X-15 following hypersonic flight at up to Mach 6.7 [1]

While the sound barrier presented a phenomenal hurdle to a previous generation of engineers, once Mach 1 could be safely reached that speed could be surpassed thereafter with relative ease. However, unlike the sound barrier problem, heating rates increase substantially and continuously as flight velocities increase into the hypersonic regime (generally agreed to be flight speeds exceeding Mach 5). The *heating problem* of hypersonic flight therefore differs from

the *sound barrier problem* in that it represents an ever-increasing severity of heating which must be endured by hypersonic vehicles. It is for this reason that the challenges faced by the engineers of the X-15 and other hypersonic programs of the post-war era continue to exist in much the same form today, despite the strides that have been made in our understanding of aerothermodynamics and materials since that time.

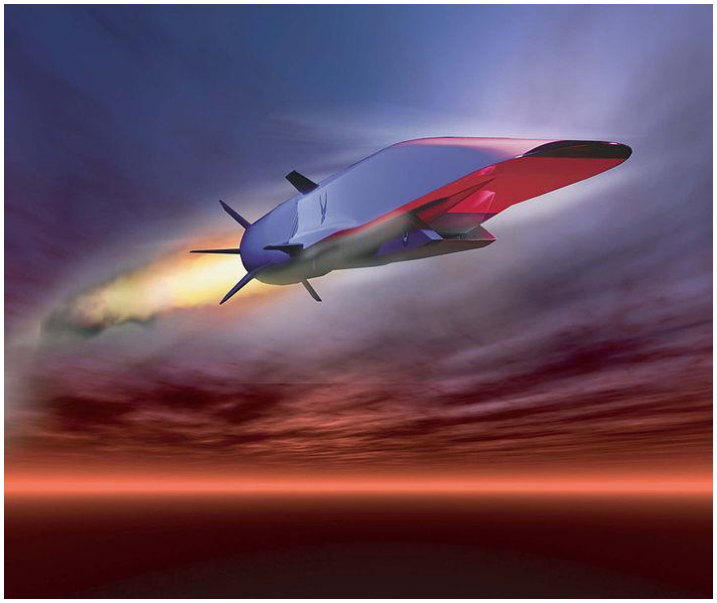

Figure 1-2: Artist's rendition of the Boeing X-51A Waverider, an unmanned hypersonic scramjet test vehicle designed in cooperation with the US Air-Force and flight-tested in 2010. The image shows some of its 10 fins protruding from the vehicle body [2].

While aerodynamic heating is a broad field unto itself, the present study concerns itself with the heating experienced at the roots of fins and wings. These regions, along with the leading edge and within the engine itself, are the zones of a hypersonic flight vehicle most impacted by aerodynamic heating. Due to the complex interaction between the bow shock forming along the wing and the significant recirculation region which forms at higher wing elevation angles (lower sweep angles), the heating rates experiences at the bases of wings and fins are also among the most difficult to predict.

For the successful design of hypersonic vehicles that fly for sustained periods in the atmosphere, the localised high heating rates due to these kinds of interactions need to be understood and quantified. Current practice involves the use of simplified heating calculations with empirical amplification factors to account for localized 3-dimensional features.

1.1 Aim of Thesis

The study described in this thesis originated out of questions raised during the design of hypersonic waverider vehicles for the HIFiRE program. Specifically, the study aimed to shed light on the heating rates likely to be experienced at the wings and fins of a HIFiRE waverider in the course of typical hypersonic flight.

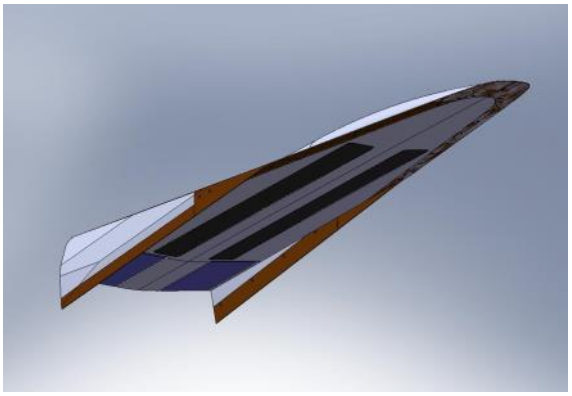

Figure 1-3: Computer-generated image of the HIFiRE IV hypersonic waverider [3].

The present study aimed to not only measure, but also help better understand, the heating rates and flow topologies experienced by a HIFiRE hypersonic vehicle during its nominal flight conditions of Mach 8 at 30km altitude.

1.1.1 Research Questions

Heating rates in the vicinity of wing-roots were expected to be dictated broadly by 4 major components of the flow;

1. Skin-friction on the flat plate of the body of the vehicle
2. The size and shape of stagnation regions forming at the base of the wing
3. Stagnation and skin-friction within the bow shock formed about the wing itself
4. The effects of impinging shock-waves formed from flow interacting with the recirculation region

To better understand the effects of each of these interactions, and to verify the degree to which they materially affect the magnitude of heating, the study aimed to address two core research questions:

1. *How do the significant features of the flow vary with experiment configuration?*
2. *How do the flow features affect peak heating rates?*

To successfully explore these questions a model composed of a flat plate and circularly blunt wedge was designed. The flat plate and protruding wedge would represent the body and wing in close proximity to the wing root. The model would be designed to have a variable wing sweep angle ranging from the lowest elevation of 65° of sweep up to its highest elevation at 45° of sweep[1].

[1] *Sweep* is defined as the complement of the acute angle formed by the incoming flow and elevated cylinder or wing.

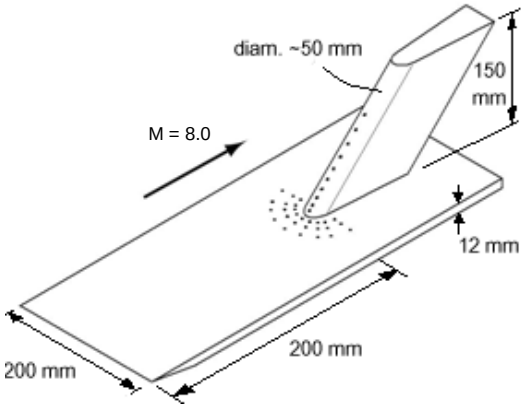

Figure 1-4: Conceptual model design, indicating dimensions and proposed gauge locations [4]

The model would be designed to fit within the test section of the T4 shock tunnel facility at the University of Queensland, and would be fitted with a series of heat transfer gauges in critical regions of the wing root.

The model would then be tested at several Mach 8 test conditions in the T4 shock tunnel which resemble conditions similar to those experienced by a flight vehicle travelling at an altitude of 30km. The resulting heat transfer data and schlieren imagery would then be compared against heat transfer predictions from theory and qualitative expectations of flow topology.

1.2 Thesis Structure

1.2.1 Chapter 2: Literature Review

The next section of the report will attempt to place both the theoretical and experimental methods employed in the present study into the context of the recent research landscape. It explores common and empirically reliable theoretical tools for quantifying heat transfer, and presents some experimental studies which have studied the effects of hypersonic aerothermodynamic heating on models with similar features to those of the wing-root model of the present study.

1.2.2 Chapter 3: Experimental Apparatus and Methodology

In this section the experimental apparatus utilised in the present study are broadly described. Specifically, this section describes 3 major components of the experimental component of the study;

1. the T4 shock tunnel facility at the University of Queensland, in which the model is tested,
2. the model itself, and the design considerations involved in its construction, and
3. the design, construction and calibration of heat transfer equipment used to measure the extremely fast variations in surface temperature (which are in-turn used to infer heat transfer rates).

1.2.3 Chapter 4: Results and Discussion

The results are presented in this section for all relevant flight conditions and wing configurations for which valid data was received. This aim of this section is not to provide a concise response to the research questions, but rather represent as completely as possible the outcomes of the experimental study against known analytical relations discussed in the previous section. This section will also outline briefly some of the hurdles encountered and will defer to relevant sections in the Appendix for discussions about equipment failures and other unexpected or unverifiable results.

1.2.4 Chapter 5: Summary and Conclusions

This section aims to use the results obtained in the previous section to refer back to the research questions outlined in this introduction. Some concluding remarks will be presented and recommendations for future studies will be made.

CHAPTER 2

Literature Review

2.1 Boundary Layer Heating

A boundary layer is best defined as;

> *"A layer of fluid, close to the surface of a body placed in a moving stream, that is distinguishable from the main airflow by distinctive flow characteristics of its own caused by friction." [5]*

As free stream flow is decelerated inside the boundary layer, the friction is converted to heat. The temperature inside this boundary layer rises in proportion to the square of the Mach number, and as it is in close proximity to the body of the flight vehicle this rise in temperature causes heat to flow into the body of the aircraft. In his landmark paper on aerodynamic heating, Van Driest begins with the most basic representation of boundary layer heating, agnostic to the stability of the flow, as a simple adaptation of Newtonian's Law of Cooling [6];

$$\mathrm{q_w} = \mathrm{k}(\mathrm{T_r} - \mathrm{T_w}) \tag{2.1}$$

Where $\mathrm{q_w}$, k, $\mathrm{T_r}$ and $\mathrm{T_w}$ represent heat flux at the wall, heat transfer coefficient, and reference and wall temperatures respectively. As a matter of convention the heat transfer coefficient is commonly represented by the dimensionless *Stanton Number*, C_H, which is itself typically represented via the Reynolds analogy, $\frac{c_f}{2s}$, where c_f is the local skin friction coefficient and s is the Reynolds analogy factor;

$$C_H = \frac{k}{\rho_e u_e C_p} = \frac{c_f}{2s} \tag{2.2}$$

Where C_p is constant-pressure specific heat and ρ_e and u_e represent density and speed of the flow respectively. The recovery temperature, $\mathrm{T_r}$, is commonly related to the boundary layer edge temperature by a recovery factor, r, as shown in Equation 2.3 below:

$$T_r = T_e\left[1 + r\frac{(\gamma - 1)M_e^2}{2}\right] \tag{2.3}$$

Where γ represents the specific heat ratio of the fluid and M_e represents boundary layer edge Mach number. The basic wall heat transfer relationship obtained by substituting the Stanton Number and recovery temperature into the modified Newtonian heat transfer equation from Equation 2.1 is shown in Equation 2.4.

$$q_w = C_H \rho_e u_e C_p \left[T_e \left(1 + r \frac{\gamma - 1}{2} M_e^2 \right) - T_w \right] \quad 2.4$$

The recovery factor does not vary substantially between laminar turbulent flows, so the *Aerodynamic Heating Problem*, as described by Van Driest, is essentially reduced to the problem of finding the local skin friction coefficient (the only remaining unknown in Equation 2.4). In solving this problem, the approaches for laminar and turbulent flows diverge somewhat, broadly into the fundamental and experimental, respectively. This is largely due to the fact that laminar flows are uniform and amenable to a theoretical approach, whereas turbulent flows are governed by vortical structures and larger-scale momentum exchanges better modelled by either numerical approaches or simply by empirical relationships.

2.1.1 Laminar Boundary Layer Heating

In order to solve Equation 2.4, both the recovery factor, r, and Stanton numbers must be derived.

In *On the Boundary Layer with Variable Prandt Number*, Van Driest solves the momentum and energy equations simultaneously for the boundary layer to obtain a recovery factor as a function of a host of properties such as density, viscosity, Prandtl number and specific heat [7]. He concludes that the variation of this quantity is so small (in the range 0.82 to 0.85) that simply approximating it as $\sqrt{Pr_e}$, or 0.85, is sufficient for the range of applications within which the present study is concerned.

As with the recovery factor, the Stanton number can also be computed precisely for laminar flow. Eber provides the following empirical relationship between Stanton number and Reynolds Number for compressible, laminar flow [8];

$$C_H = 0.295 Re^{-0.5} Pr^{-2/3} \quad 2.5$$

Van Driest [6] confirmed that solving Equation 2.4 with Eber's equation (Equation 2.5) and with 0.85 for the recovery factor yields sufficiently accurate results for flat plate heat transfer rates in laminar flows up to at least Mach 10.

2.1.2 Turbulent Boundary Layer Heating

Turbulent flows cannot be modelled exactly by analytical relationships, due simply to the fact that the mechanisms of momentum exchange are neither uniform nor precisely known. Simplifying assumptions are therefore made in adapting Equation 2.4 to turbulent flows. By making the simplifying assumption that the shear distribution is linear as a function of wall distance, Von Karman [9] arrived at a relationship for the recovery factor as a function of laminar and turbulent Prandtl numbers.

Van Driest adapted these derivations to produce a relationship between Mach number, temperature, Reynolds number and the skin friction coefficient [6]. The result of this derivation is shown in Equation 2.6.

$$\frac{0.242}{{c_f}^{1/2}\left(\frac{\gamma-1}{2}M_e^2\right)^{1/2}}\left(\sin^{-1}\alpha+\sin^{-1}\beta\right)=0.41+\log\left(Re_x c_f\right)-f(n)\log\frac{T_w}{T_e} \qquad 2.6$$

where

$$\alpha=(2A^2-B)/(B^2+4A^2)^{1/2}$$

$$\beta=B/(B^2+4A^2)^{1/2}$$

$$A^2=\left(\frac{\gamma-1}{2}M_e^2\right)\Big/\left(\frac{T_w}{T_e}\right)$$

$$B=\left[\left(1+\frac{\gamma-1}{2}M_e^2\right)\Big/\left(\frac{T_w}{T_e}\right)\right]-1$$

Root-finding algorithms can be used to solve for c_f, as is done in the present report where analytical turbulent flat plate heating rates are required.

$f(n)$ represents a function of the exponent n in the power viscosity law ($\mu=cT^n$), and depends on the law assumed for the mixing length model. It can be shown that $f(n)=n=0.76$ for the Von Karman mixing length model, and this simplification will be used in the present study [6].

The recovery factor for turbulent flow is typically found experimentally, and various methods for deriving it appear to arrive at a rather consistent figure in the vicinity of 0.88. Perhaps the earliest and simplest is Squire's $r=Pr_L^{1/3}=0.892$, which will be used here [10].

By using a simple root-finding algorithm to derive the skin-friction coefficient and substituting the (assumed constant) value for the turbulent recovery factor, there is sufficient information to solve Equation 2.4.

2.2 Heat Transfer in Wing-root Interactions

An overview of research observing swept-surface hypersonic heating can be broadly divided into computational and experimental studies. Existing literature in experimental studies of this kind of interaction are confined to supersonic and "near hypersonic" conditions, with one experimental study observing interactions at Mach 3 [11], the highest velocity for this kind of investigation to the Author's knowledge. Hung et. al [12] reported good correlation between numerical solutions to the Navier-Stokes equations for supersonic flows over a wedge at zero yaw, although this particular study did not address heat transfer measurements.

McMaster et al. [15] extended the study of Hung et. al to include a numerical study of the effects of sweep on pressure distribution and surface shear at Mach 2.95.

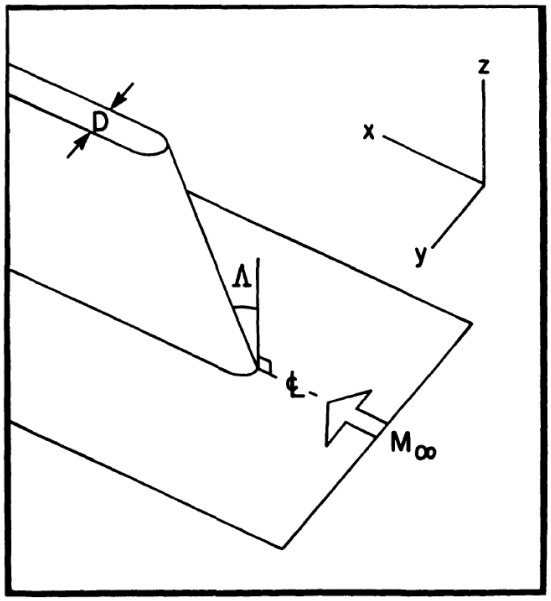

Figure 2-1: Diagram of the swept blunt wedge on a flat plate as simulated by McMaster et al. [13]

McMaster et al. were able to numerically calculate the expected flow topology past a blunt wedge at sweep angles ranging from 30° to 68°. They noted that flow topology bifurcates at sufficiently high angles of sweep (68° for the studied conditions), with a noted reduction in upstream influence of the flow field and weakening of the horseshoe vortex formed about the wedge.

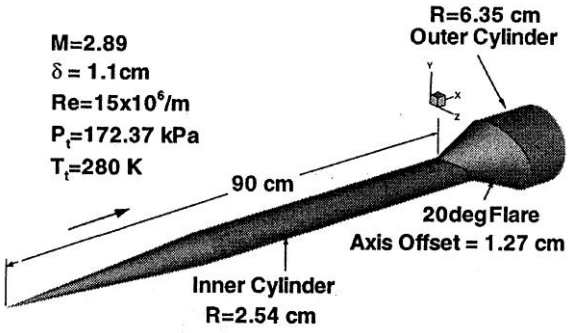

Figure 2-2: Cylinder/offset flare model from [11]

The Wideman, et al. [11] study was carried out at the NASA Ames Research Center, utilising Laser Interferometric Skin-Friction (LISF) [12] to quantify skin friction. It confirmed the general topology of this flow involved the interaction of a cylinder/offset flare combination with an incoming turbulent boundary layer, by visualising the oil patterns. Due to a reported lack of accurate skin-friction data for inclined wedges and flares at high velocities, the study focused on obtaining such data. Through oil flow patterns visualised through LISF, and measurements of

pressure and skin friction taken at Mach 3 with the model shown in Figure 2-2, this work showed the presence of a separation that began at the leading portion of the flare and swept around the cylinder with influence well upstream of the cylinder/offset flare junction.

Based on skin friction measurements, Gaitonde & Shang [13] found that the LISF method suggested flow separation beginning at 17.8mm upstream of the wedge in the lower symmetry plane (as indicated by marker S4 in Figure 2-3). Pressure measurements, carried out using an electronic scanning pressure system, suggested the onset of separation 5.0mm downstream at 18.3mm, correlating well with the LISF measurements. Oil flow patterns, however, indicated that separation occurred significantly upstream at 15.3mm, but did not provide an explanation as to why this discrepancy occurred. Interestingly, flow reattachment was observed to occur at 8.2mm downstream of the wedge incline, in perfect agreement with the oil flow patterns.

While this experiment did not directly reveal information regarding heat flux, the Reynolds analogy can be used in correlation with CFD results to correlate the skin friction measurements obtained from the above study with future heat flux measurements from the present work.

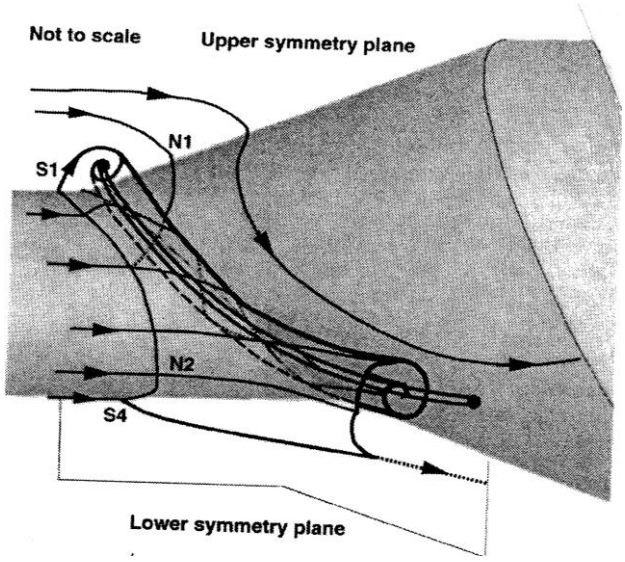

Figure 2-3: Flow topology of interaction [13]

Further separating the report of Widemann et al. [11] from the present work is the fixed flare angle of 20 degrees used in that study. The present work will utilise a varying wing angle experiment to obtain measurements of flow topology with respect to angle, as opposed to the fixed topology utilised by Wideman et al. The 20 degree fixed angle of the flare represents the higher end of sweep angles used in the present work. Combined with the relatively lower Mach number of 3 compared with a Mach number of 8 proposed for the present work, the Widemann et. al [11] paper will serve only as a guide for the expected topology as well as possibly providing additional insight into how higher Mach numbers affect these types of flow topologies.

A detailed CFD study of the Wideman et al. experiment was conducted by Gaitonde & Shang [13], who recognised the problems with unsteadiness inherent in the physical results of the Wideman

et al. study and produced a computerised model. It predicted the topology and scale of the interaction quite well, and supplied a useful representation of the flow field (including the principal vortical structure) shown in Figure 2-3 [13]. While the cylinder/offset flare geometry is somewhat different to a wing root, this flow topology is representative of the wing-root problem when the sweep angle of the wing or fin is low enough to produce a separation of the vehicle surface boundary layer.

The flow topology, as represented in Figure 2-3, clearly shows the formation of vortical structures, created during the separation of incoming flow, which relax as they pass over the inclined region. An analogous pattern is expected for the present study, where vortical structures will form at the upstream end of the wedge incline and extend past the body of the wing.

The study by Gaitonde & Shang [13] defines the upstream boundary condition turbulence parameters based on skin friction measurements obtained from the aforementioned experimental study by Wideman et al. . The CFD study observed a shock angle of 31.5°, in agreement with their analytical analysis for such a topology.

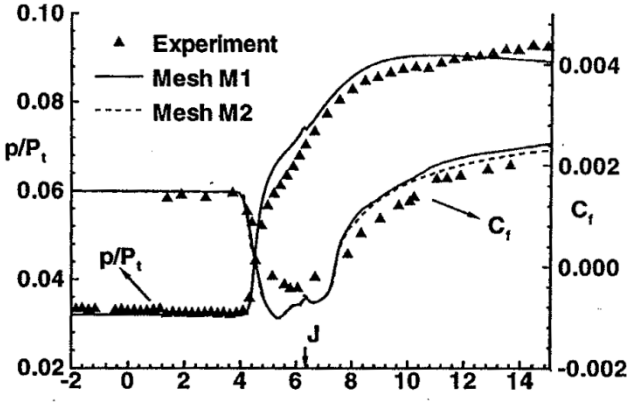

Figure 2-4: Comparison of streamwise surface pressure and coefficient of friction (C_f) at the lower symmetry plane with the k-ε model. J represents the juncture location [13].

While many of the aspects of this study cannot be compared directly with the present work due to the slightly different topologies, it might be possible to draw some comparative conclusions from measurements of skin friction as a function of streamwise location. The CFD study by Gaitonde & Shang [13] achieved very good correlations between surface friction coefficients for the experimental and CFD studies, as illustrated in Figure 2-4.

The studies mentioned above focus on a slower flow regime and place an emphasis on skin friction and surface pressure, as opposed to heat flux in the present study. There are however some analogous behaviours against which the results of the present study can be validated. These include the vortical structures observed at the separation region (as seen in Figure 2-3) and the skin friction behaviour as seen in Figure 2-4, which can be related to heat flux via the Reynolds analogy.

2.3 Blunt Cylinder Heat Transfer

Heating along the centre lines of blunt cylinders (at the line along the cylinder where the surface of the cylinder is farthest upstream) is among the physical situations more amenable to analytical solutions than the previously discussed wing-root interactions. The solution to the 0° sweep case is a relatively simple stagnation point problem at large distances from the wing, as the heating is analogous to that of a semi-infinite cylinder extended perpendicularly to the flow.

By combining the Newton's Law of Cooling with the understanding that stagnation point heating is essentially a process of flow stagnation causing a temperature differential, Van Driest (1956) was able to derive a semi-empirical relationship for laminar stagnation point heating as a function of flow conditions, as shown in Equation 2.7;

$$q_w = 0.57 Pr^{-0.6} (\rho_e \mu_e)^{1/2} \sqrt{\frac{du_e}{dx}} (h_{aw} - h_w) \tag{2.7}$$

where $\frac{du_e}{dx}$ represents the first derivative of spanwise velocity in the spanwise direction. This corresponds simply to spanwise acceleration at the stagnation point, $x = 0$, for which;

$$\left(\frac{du_e}{dx}\right)_s = \frac{1}{R} \sqrt{\frac{2(p_e - p_\infty)}{\rho_e}} \tag{2.8}$$

By accounting for the effects of dissociation energy and atomic diffusion, Fay and Riddell [14] were able to adapt the Van Driest solution[2] for stagnation point heat transfer for a dissociated gas.

$$q_w = 0.57 \left(\frac{4}{3}\right)^j Pr^{-0.6} (\rho_e \mu_e)^{0.4} (\rho_w \mu_w)^{0.1} \sqrt{\frac{du_e}{dx}} (h_0 - h_w) \left[1 - (Le^{0.52} - 1) \frac{h_D}{h_0}\right] \tag{2.9}$$

Equation 2.9 shows the Fay & Riddell solution for stagnation point heating in an equilibrium boundary layer, where j = 0 for 2D flow and j = 1 for axisymmetric flow. While neither the Van Driest nor the Fay and Riddell solutions present a direct analytical solution to the heating rates to be expected in the experiments of the present study, they do present a foundational solution to blunt wedge heating. These equations were subsequently used to solve for swept blunt bodies such as the subject of the present study. These will be discussed in the following section.

[2] The Van Driest solution is shown in equation 2.7

2.4 Swept Blunt Cylinder Heat Transfer

By making assumptions about the boundary layer development around a swept cylinder at various sweep angles, Beckwith was able to provide approximate semi-analytical solutions, based on the works of Fay and Riddell and Van Driest, to the heating problem for varying angles of sweep [15]. As we do not need to make any assumptions about boundary layer edge conditions for the stagnation case, the solutions developed by Beckwith are exact for the laminar case.

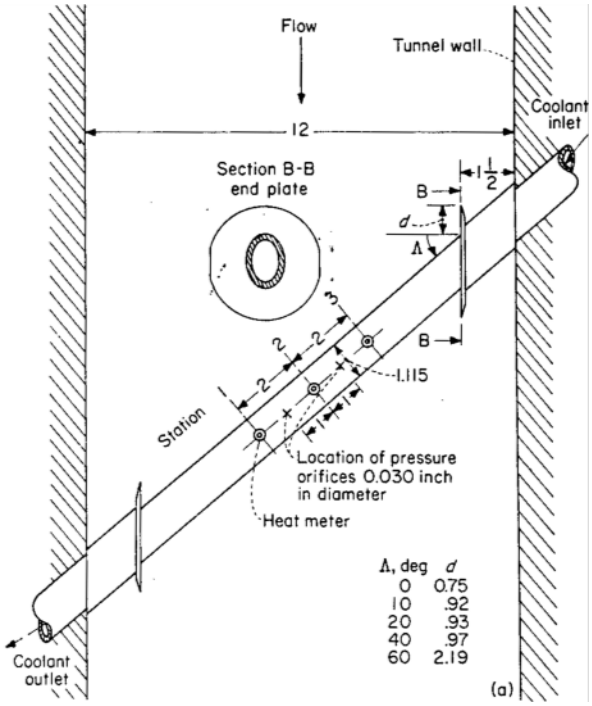

Figure 2-5: Experimental setup for heat flux measurements over a swept cylinder at Mach 4.15 [15]

Beckwith recognised that chordwise flow can be considered independently of spanwise flow in a chordwise uniform fluid flow. This observation has the very useful implication that the stagnation point heating equations of Van Driest and Fay and Riddell can in fact be applied to swept, semi-infinite cylinders by considering for a swept cylinder the chordwise-normal component of flow as one would the incoming flow under a perpendicular orientation. In order to validate the semi-analytical solution that resulted from these observations, an experiment was conducted using a cylindrical body at varying angles of sweep, as shown in Figure 2-5.

Beckwith arrived at the following solution for the Nusselt number;

$$\frac{k_s l}{k_\infty} = Pr^{1/3}\left(\frac{u_{R,\infty} l}{\nu_\infty}\right)^{\frac{n}{1+n}}\left(\alpha\frac{p_s}{p_\infty}\frac{\mu_r}{\mu_o}\frac{T_\infty}{T_r}\right)_s^{\frac{n}{1+n}}(\sin\Lambda)^{\frac{n-1}{1+n}}\left(\frac{49}{376}\frac{\mu_o}{\mu_\infty}\cos\Lambda\frac{l}{u_\infty}\frac{du_e}{dx}\right)_s^{\frac{1}{1+n}} \qquad 2.10$$

where $k_s l/k_\infty$ is the Nusselt number and is directly correlated to surface heat flux via the known temperature parameters of the heat transfer coefficient at the stagnation point, k_s. This equation is essentially an empirical adaptation to the observation that the Van Driest solution[3] varies with the sine of sweep angle. While this equation, which does not consider the effects of chordwise flow on heat generation, fails at high sweep angles, it provides a robust and tested benchmark against which to verify experimental measurements.

2.5 Instrumentation

While not trivial due to the extremely short test times of the T4 shock tunnel facility in which the present study was conducted, solutions for the measurement of surface heat transfer in shock tunnels are well documented.

In their seminal whitepaper on techniques for measuring heat transfer in hypersonic facilities, Schulz & Jones (1973)[4] outline a 1-Dimensional heat transfer analysis, in which the heat transfer rate is deduced from a surface temperature reading, provided some pivotal assumptions hold true. They documented the derivation of transient heat flux from surface temperature readings from the differential equation governing heat flow into a 1D medium;

$$\frac{\delta^2 T}{\delta x^2} = \frac{1}{\alpha}\frac{\delta T}{\delta t} \tag{2.11}$$

where T is temperature, x is the position in the 1D medium, and α is the thermal diffusivity of the material, which can be quantified as $\alpha = \kappa/\rho C_p$, where κ, ρ and C_p are the thermal conductivity, density and constant-pressure specific heat of the material respectively. Schulz & Jones showed that if a sensor is able to measure temperature at the surface of such a medium, and assuming that;

1. the sensor does not have a significant effect on the effective properties of the material,
2. the medium behaves as a 1D semi-infinite substrate for the duration of the measurement, and
3. the distribution of temperature through the medium at time $t = 0$ is both known and uniform.

then Equation 2.11 can be used to derive an analytical solution to the transient heat flux, as shown in Equation 2.12.

[3] The Van Driest solution is shown in Equation 2.7
[4] See reference [21]

$$\dot{q}_s(t) = \sqrt{\frac{\rho C \kappa}{\pi}} \left[\frac{T(t)}{\sqrt{t}} + \int_0^t \frac{T(t) - T(\tau)}{(t-\tau)^{3/2}} d\tau \right] \quad 2.12$$

Schulz & Jones note that the singularity at $t = \tau$ is a source of error in numerical solutions. While this was a serious concern at the time their report was published, extremely small step sizes allow a modern numerical solution to simply ignore the final steps which are not computationally representable in the applicable floating point domain. The result is that Equation 2.12 is readily solvable to within precision well above that of the instrumentation on which the data was collected.

Schulz & Jones derived the entire set of equations required to solve surface heat flux from surface temperature, noting that Equation 2.12 is applicable to any temperature sensor operating under a regime approximately analogous to a 1D, semi-infinite substrate for the applicable testing conditions. The decision to utilise thin film and thermocouples for the present study was therefore only a consideration of physical suitability.

CHAPTER 3

Experimental Apparatus and Methodology

3.1 T4 Free-Piston Reflected Shock-Tunnel

Experimental testing was conducted in the Centre for Hypersonics T4 Shock-Tunnel at the University of Queensland. The T4 Shock-Tunnel is a free-piston driven, reflected shock tunnel [16].

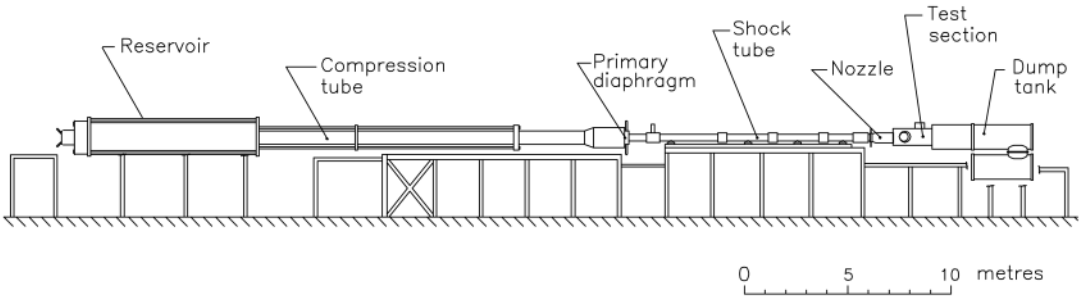

Figure 3-1: T4 Schematic [17]

The conceptual layout of the T4 Shock Tunnel facility and its components is shown in Figure 3-1. The compression tube, which the piston traverses during a shot, is 26m long with an internal diameter of 229mm. As the piston approaches the downstream end of the compression tube during a shot it compresses the driver gas, a mixture of argon and helium, causing the primary diaphragm to rupture and transmit a compression wave through the shock tube, which is 10m in length, has an internal diameter of 76mm and is filled with the test gas (dry air for the present study, although nitrogen is also commonly used). The primary diaphragm is a mild steel sheet with widths ranging from 1mm to 6mm, which correspond to burst pressures of 12.5 to 75MPa, subject to the material used.

Before reaching the test section, the test gas first ruptures a smaller secondary diaphragm, composed of 0.1mm Mylar material of negligible burst pressure, located at the throat of the nozzle. The purpose of this diaphragm is to separate the test gas in the shock tube from the test section and dump tank, which are evacuated prior to a shot.

3.1.1 Operational principle

The operational principle of T4 is summarised in Figure 3-2, with an $x - t$ diagram showing the propagation of shock waves through the shock tube section of T4 during an experiment.

With reference to Figure 3-2, the annular reservoir surrounding the compression tube is filled with pressurised air prior to an experiment. The experiment is initiated by releasing the air from the reservoir into the launcher section of the compression tube, where it forces the 87kg piston

to release from its starting position in the launcher and travel through the compression tube, causing the test gas to compress behind the primary diaphragm. As the piston accelerates through the compression tube, it causes near-isentropic compression of the test gas. As the primary diaphragm ruptures, it forces a shock wave through the shock tube, compressing the test gas and forcing it to accelerate toward the downstream end of the shock tube. As the downstream end of the shock tube is almost entirely sealed, with only an 8 to 20mm throat opening, it causes the initial shock wave to reflect back into the shock tube. This reflection effectively stagnates the flow at the downstream end of the shock tube. As the secondary diaphragm ruptures, the high pressure / high temperature gas at the nozzle throat expands into the nozzle and passes over the model in the test section.

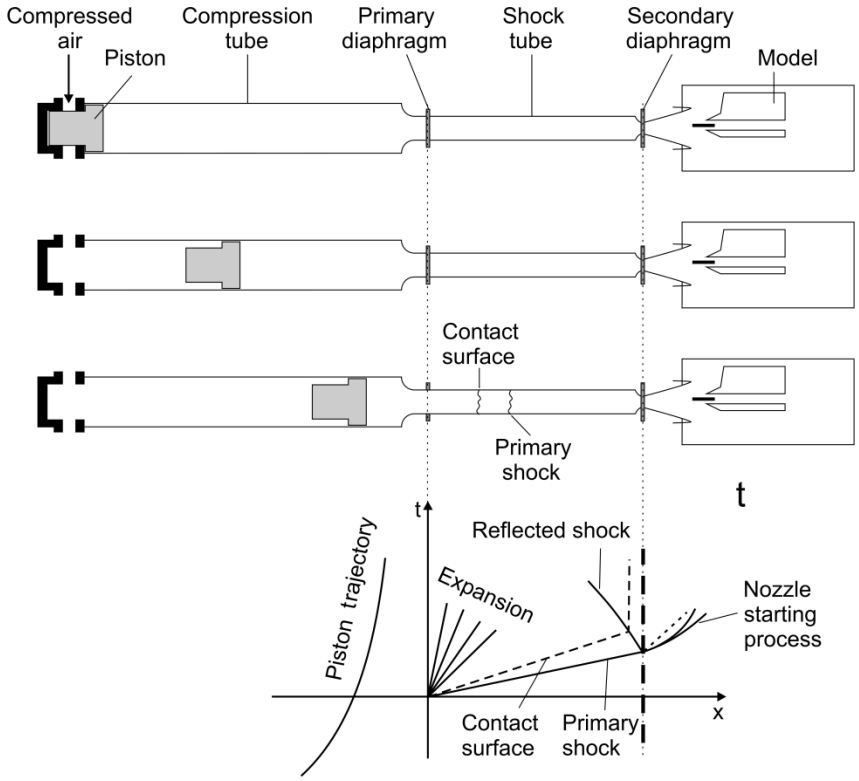

Figure 3-2: Operational principle of a free piston reflected shock tunnel [18]

As shown in Figure 3-2, the contact surface represents the interface between test gas and driver gas. In practice, this interface is not discrete, consisting instead of a finite region in which the gas transitions from test gas to driver gas. While the duration of an experiment is theoretically limited by the arrival of expansion waves which distort the supply pressure of the shock tube to the nozzle, for certain conditions the limit factor becomes the arrival of driver gas in the test section. The modes of operation of the tunnel are categorised as *tailored*, *undertailored*, or *overtailored*. When the tunnel is tailored, the pressure ratios and velocity distributions are identical on either side of the contact surface, thereby allowing shock waves to traverse the contact surface without causing secondary shock waves. If the tunnel is undertailored, expansion waves are produced as the reflected shock wave crosses the contact surface, resulting in a faster than desirable drop in nozzle-supply pressure. In an overtailored experiment,

compression waves are produced as the reflected shock traverses the contact surface, causing an increase in the supply pressure to the nozzle and facilitating driver gas contamination of the test section.

An additional consideration in free piston driven shock tunnels is *tuning*, which refers to the choice of compression tube gas and the fill pressures of both the compression tube and reservoir. These parameters are manipulated to ensure that the piston continues to move downstream following rupture of the primary diaphragm, maintaining driver gas pressure as the shock wave compresses the shock tube test gas.

3.1.2 Mach 8 nozzle

The Mach 8 nozzle used for the present study is shown in Figure 3-3. This nozzle was initially designed to produce Mach 7.6 flow at nozzle-supply enthalpies of 3.5 MJ/kg. For the conditions of the present study, nozzle exit Mach numbers fell within a 7.0 - 7.5 range for the entire set of conditions.

The nozzle has an inner diameter of 270mm at the nozzle exit. The inner radius of the wall is almost constant near the exit, alleviating some of the design constraints as the leading edge of the model could be placed inside the nozzle to ensure that the wing root itself was placed where ideal flow conditions are expected to develop.

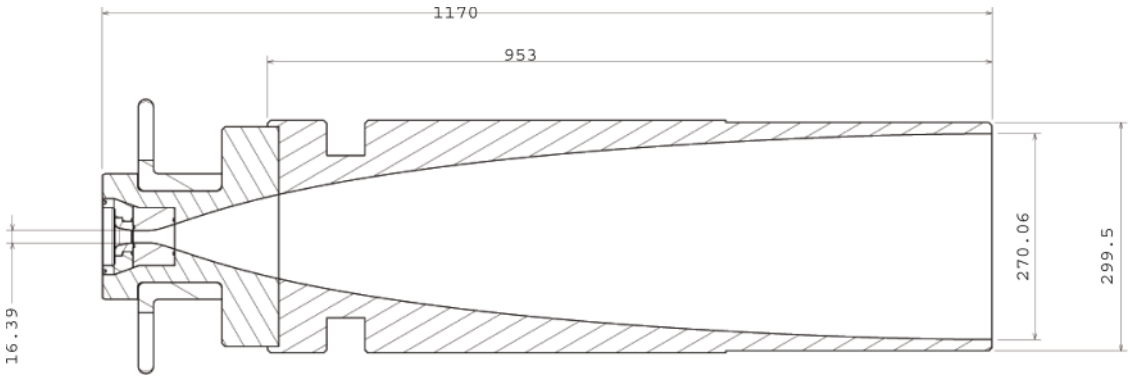

Figure 3-3: Mach 8 nozzle schematic [17] (Dimensions in millimetres)

3.2 Model Design and Manufacture

The design of the wing-root experiment began with an assessment of design considerations for the experiment and the parameters of the T4 shock tunnel facilities. A CAD image of the model is shown in Figure 3-4.

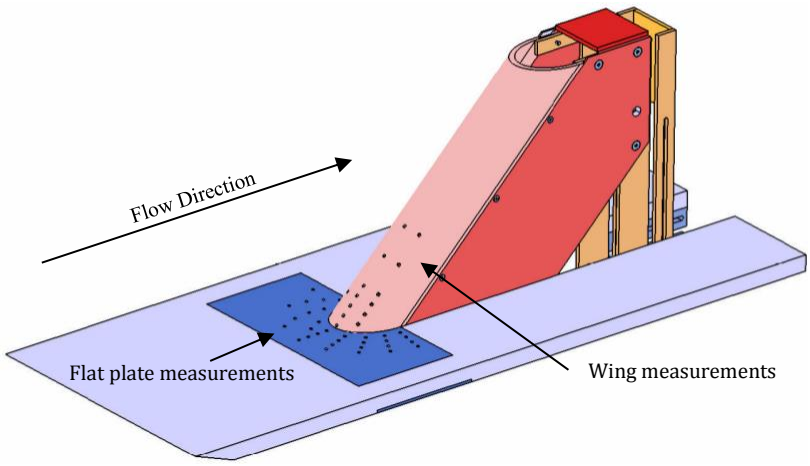

Figure 3-4: Isometric view of the model design at 45° sweep angle (small surface dots represent gauge recesses)

The cylinder representing the wing or fin of a hypersonic vehicle was designed to allow for continuously varying from 45° to 70° of sweep[5]. The flat plate and leading edge, which represent the body of the hypersonic vehicle, were required to have a length sufficient to allow for the development of a turbulent incoming boundary layer, with consideration for the space limitations of the test section in the T4 shock tunnel facilities. The leading edge precedes the wing-root intersection by ca. 200mm (varying as much as 4mm for different configurations), and the plate is 200 mm wide. The span length is 240mm, although the effective length varies slightly depending on configuration, as a certain fraction of the wing will be inside the body for lower sweep angles.

RTV sealant was used to ensure that the gaps forming between the blunt wedge and the elliptical slot in the flat plate would not cause flow to leak into the model and out of the recirculation region. This was necessary as the slot was shaped to suit a 45° swept wedge and provided an imperfect fit for all other configurations.

The final design of the wing-root experiment is further illustrated in Figure 3-5, showing key dimensions.

[5] Where *sweep* is defined as the angle between the axis perpendicular to the body of the vehicle and the axis formed by the leading edge of the wing (see θ in Figure 3-5).

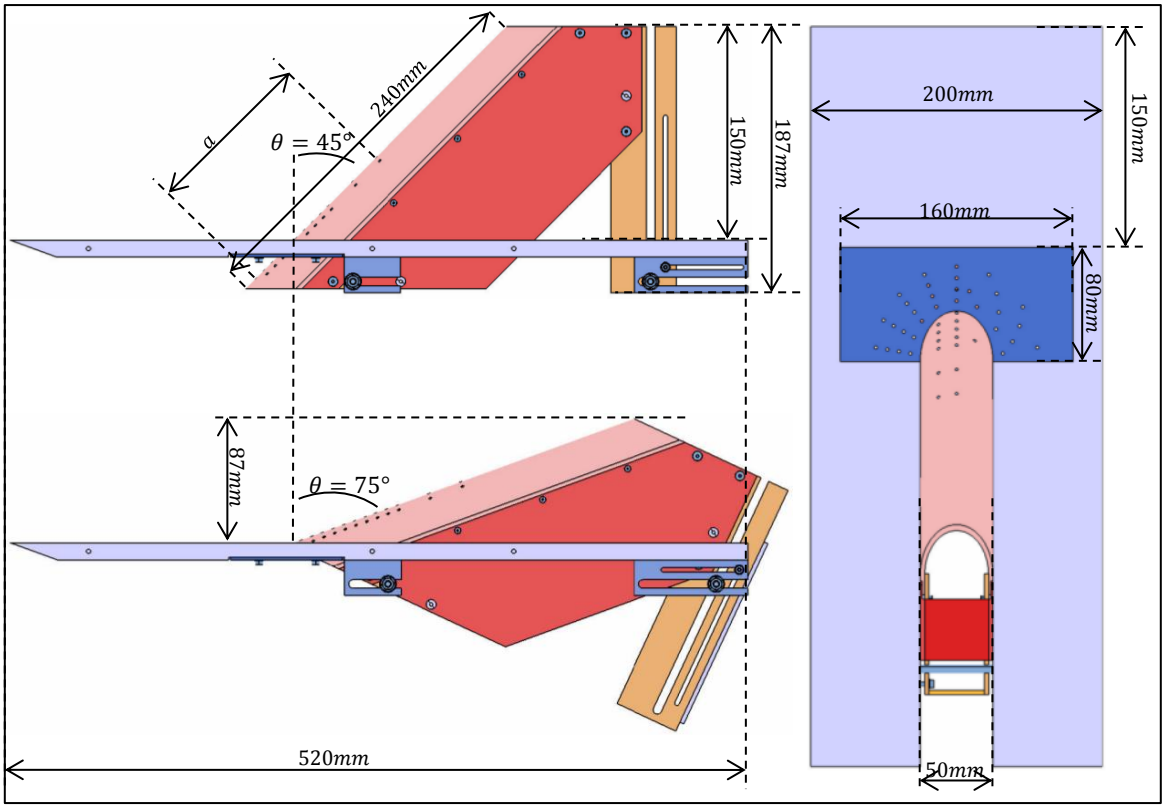

Figure 3-5: Model design showing 45° and 75° sweep angle configurations (top and bottom left respectively), and relevant dimensions, including the distance between thermocouple gauges (a) and sweep angle (θ)

The model is also inverted in the actual experiments to allow for more stable and efficient mounting into the T4 test section. However, for the purpose of images in the present report, the wing will be shown protruding upwards.

Figure 3-6 shows the final model after all thin film gauges and thermocouples have been inserted, and the model has been placed in the tunnel. Note that the photo has been inverted, as the actual model was placed in the tunnel with the wing protruding downward. All images are shown with the wing extending upward for consistency.

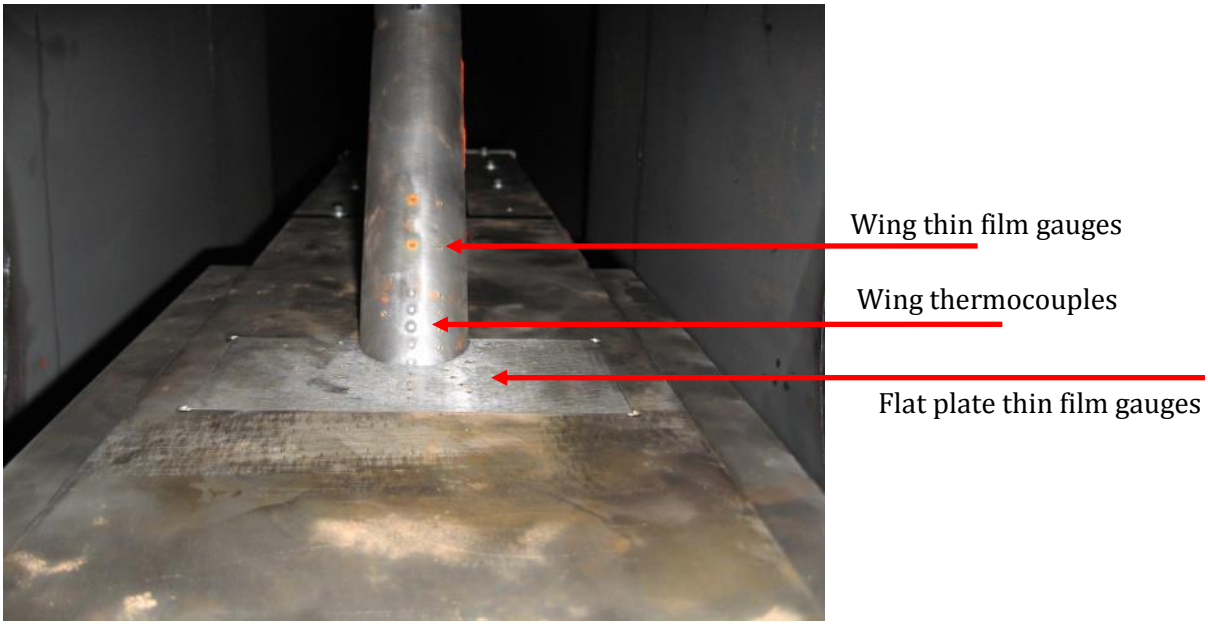

Figure 3-6: View of the model after insertion into the tunnel, and prior to the first shot

A significant portion of the experimental preparation involved the design of shielding components (Figure 3-7), thin film gauges and thermocouples. The aim of the shielding is essentially to protect the internal components of the instrumentation while allowing the flow to pass over the model as freely as possible, so as to ensure that any perturbations caused by it do not interfere with the measurements. Experimental results did not suggest that any interference took place during the tests.

The final model, as mounted prior to the first shot, is shown in Figure 3-7.

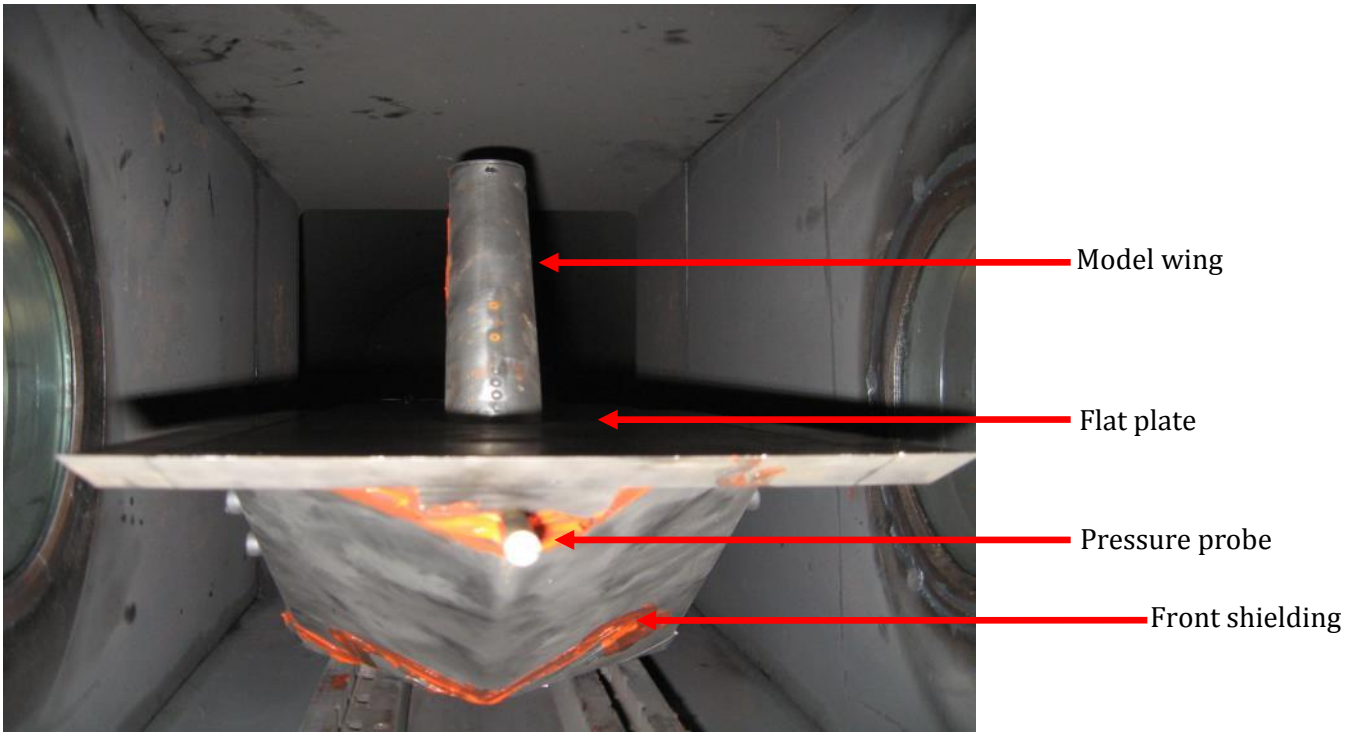

Figure 3-7: Final model configuration prior to the first shot, showing the wing, flat plate, stagnation pressure sensor and front wedge shielding. Note that this image has been vertically inverted for consistency with other representations of the model.

Measurement of heat flux during the experimental campaign was conducted with the use of thin film gauges and thermocouples, using 2mm cylindrical substrates. These sensors were mounted on the cylinder and flat plate, at expected points of interest near the wing-root junction (see Figure 3-4). To avoid any interference with the flow great care was taken to mount the gauges flush with the surface of the wedge and flat plate[6]. A total of 31 flat plate recesses were arranged in a distribution thought to produce the most useful information about the flow regime, while taking into account practical limitations. The resulting final configuration used in the campaign is shown in Figure 3-8 and Figure 3-9.

[6] Further detail on the design of the thin film and thermocouple gauges can be found in Appendix Section 6.1

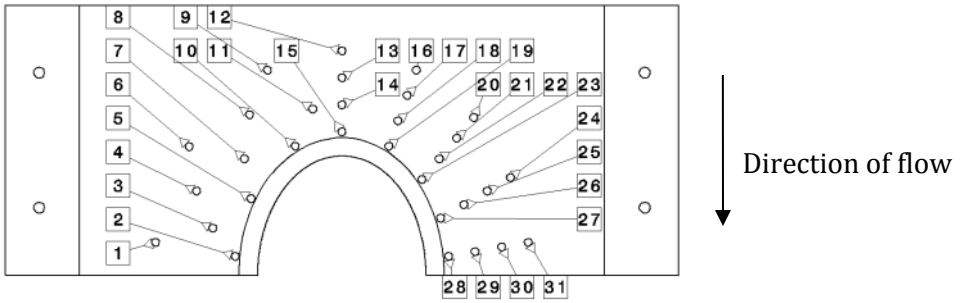

Figure 3-8: Flat plate recess numbering (all recesses are used for thin film gauges)

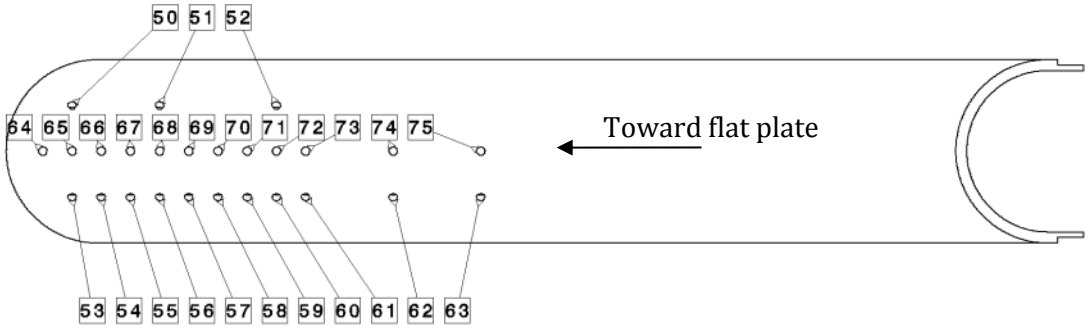

Figure 3-9: Wing recess numbering (recesses 50-63 used for thin film gauges, and recesses 68-73 used for thermocouples; the remaining recesses were sealed)

Note that the gauge recesses are asymmetrically distributed; this is the case on both the blunt wedge (the wing) and the flat plate (the vehicle body) to take advantage of flow symmetry, allowing for the gauge responses to be superimposed onto both sides. This was done to allow for mapping of the resulting heat fluxes at a higher spatial resolution than would otherwise be possible due to the size and minimum achievable distance between each of the 2mm gauges.

3.2.1 Trip design

After the initial low and high pressure shots failed to demonstrate clear turbulence, a trip was manufactured to attempt to induce turbulence in the boundary layer. Prior analysis and experimental results for flat-plate hypersonic tests conducted in the same facility at analogous flight conditions suggested that a saw-blade trip raised at 2mm would be sufficient to induce flow transition [19].

The trip was therefore constructed from a saw blade, with a span-wise oriented 2mm edge raised perpendicular to the flat plate, 50mm downstream of the flat plate leading edge (ca. 150mm upstream of the wing-root intersection, varying slightly with configuration). The trip was attached to the flat plate using Araldite© 2-part epoxy adhesive.

3.3 Heat Transfer Sensors

While it was initially thought that thin film gauges might be sufficient for measuring heat flux on the wing-root model, it was later decided to use thermocouples on the wing centreline. This was done to ensure that in the event of the more sensitive thin film gauges failing, the thermocouples would still be able to provide heat flux data on the wing. This section is therefore divided into a discussion on the thin film gauges used on the surface of the flat plate and outer regions of the wing, and the thermocouples used along the wing centreline (referred to as the stagnation line in reference to the stagnation of the spanwise component of flow).

3.3.1 Thin-Film Gauges

Thin-film gauges were chosen to measure the heat flow due to both their ideal suitability (fast response) and the availability of suitable equipment at the Centre for Hypersonics for manufacturing these gauges.

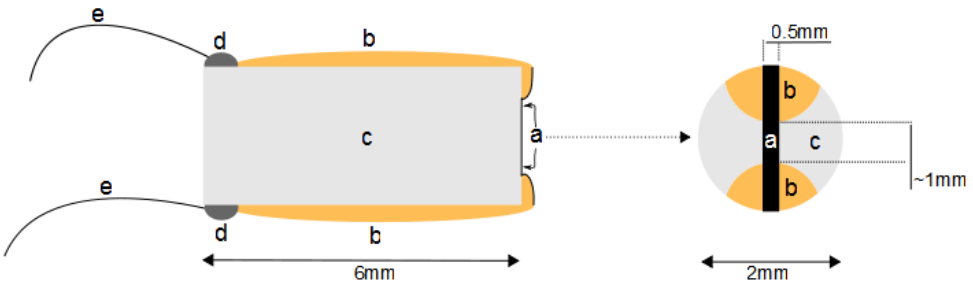

Figure 3-10: Conceptual Representation of a Thin Film Heat Flux gauge, showing the thin nickel strip (a), gold conducting strips (b), Quartz substrate (c), soldered junction (d) and electrical leads (e).

The Auto 500 Sputtering system at UQ is an automated sputtering machine capable of producing extremely thin layers of metal and ceramic coating required to produce high quality thin film gauges. The gauges are typically composed of a ceramic substrate, on which a thin layer of metal is deposited via sputtering. Changes in electrical conductivity of the metal occur in response to changes in material temperature, and by modelling both the thickness of the film and the state and conductive properties of the ceramic substrate, it is possible to derive extremely accurate and rapid heat flux measurements from the surface of the model. A conceptual representation of a thin film gauge is shown in Figure 3-10.

The electrical resistance of the nickel surface (at *a* in Figure 3-10) is derived from the known material properties of nickel. Since we now effectively have surface temperature as an input, we can derive the heat flux providing that we know the flow of heat leaving the surface and entering the substrate itself. As the flow of heat is closely approximated as being perpendicular to the gauge surface, a 1D approximation of the gauge will suffice, as is shown in Equation 2.12, from which we can derive a numerical analogue that will model the conditions at each time step:

$$\dot{q}(t) = \sqrt{\frac{\rho C K}{\pi}} \left[\sum_{i=1}^{n} \frac{T(t_i) - T(t_{t-1})}{\sqrt{(t_n - t_i)} + \sqrt{(t_n - t_{i-1})}} \right] \quad 3.1$$

An important fundamental distinction between the implementation of gauges operating on the semi-infinite heat transfer principle (such as thermocouples and thin film gauges) and other pressure and temperature probes is that the entire history of surface temperature measurements leading up to the current time, *t*, is required in order to obtain a reading of heat flux at that time. This is in contrast to most pressure probes where a reading is only taken for the period where the flow has stabilised.

Gauge resistances during experiments were measured as the excitation voltage when the gauges of known steady-state resistance were placed in series with a 70 ohm resistor and subject to 1.7 volts in a slow-response voltage regulator.

3.3.2 Thermocouples

Based on the expectation that the sub-micron thickness of the silicon dioxide layer used to protect the conductive element of the thin film gauges would not be sufficient to protect them during the test time if the surface were directly facing the flow (as would be the case for gauges on the wing), it was decided to replace the centreline of thin film gauges with thermocouples to ensure usable data. This decision was later vindicated by the rapid loss of the thin film gauges that were still kept on the wing during the tests. Due to the limited availability of thermocouple gauges, only 6 were installed in gauge recesses 64-69.

Once the material properties of the electrodes were defined, it was possible to convert the thermocouple voltage response into a surface temperature reading, by means of multiplying the voltage reading by the sensitivity of the gauge. In order to convert the surface temperature into a heat flux reading, as per Equation 3.1, it is necessary to obtain density, heat capacity and conductivity values for the cross-sectional properties of the thermocouple. Due to tapering of the constantan electrode[7], the cross-sectional properties of the thermocouple are not constant in the axial direction (direction of heat flux). In order to simplify the modelling of the thermocouple, the cross-section expected to be most representative given the experimental conditions will be used. It will be assumed that incident heat by the end of the test time does not penetrate a significant distance into the thermocouple, and that the thermal properties with respect to Equation 3.1 can be satisfactorily modelled by taking the average properties of the two metals at the surface of the thermocouple. The density, heat capacity and conductivities of constantan and chromel are illustrated in Table 3.1.

[7] See Figure 6-12 for a schematic view of the thermocouple design.

Property	Value
Constantan:	
ρ (kg.m^{-3}) [8]	8920
C (J.kg^{-1}.K^{-1}) [7]	401.0 (@273K)
κ (W.m^{-1}.K^{-1}) [8]	21.171 (@373K)
Chromel:	
ρ (kg/m^{3}) [8]	8730
C (J.kg^{-1}.K^{-1}) [7]	473.0 (@373K)
κ (W/m.K) [8]	19.2464 (@373K)

Table 3.1: Thermal properties of thermocouple materials Chromel, Constantan and Araldite, with values corresponding most closely to expected test conditions of ~300K.

In order to now obtain an effective thermal product, $\left(\sqrt{\rho C \kappa}\right)_e$, for the thermouple materials, the thermal products for each of the constituent materials are averaged:

$$\left(\sqrt{\rho C \kappa}\right)_e = \frac{\left(\sqrt{\rho C_p \kappa}\right)_{const} + \left(\sqrt{\rho C_p \kappa}\right)_{chrom}}{2} = 8808.47\, J.m^{-2}.s^{-1/2}.K^{-1} \qquad 3.2$$

Subscripts *const* and *chrom* in Equation 3.2 refer to constantan and chromel materials respectively. The thermocouples were constructed by Brian Loughrey, a technician at the facility experienced in the manufacture of this type of gauge. For a full discussion on the construction, calibration and quality control of the gauges refer to Appendix Section 6.1.2.

CHAPTER 4

Results and Discussion

This chapter presents the experimental data collected during the experimental test campaign. The experimental campaign consisted of a total of 22 shots, representing the University of Queensland T4 Hypersonics facility shots 11043 to 11064[8]. All references to the wing, flat plate and direction of flow are with respect to Figure 3-4. Flows are presented as occurring from left to right for cross-sectional views, and from top to bottom for flat plate measurements.

Section 4.1 presents the derived flow conditions for the various flight configurations simulated throughout the test campaign.

Schlieren imagery is presented in Section 4.2. Schlieren photographs were taken at millisecond intervals, and provide a snapshot of the flow features for every shot conducted during the campaign. These images were also calibrated to allow for accurate measurement of the distance and location of flow features of interest.

Heating data obtained on the wing of the model is presented in Section 4.3. As this data is obtained along the centre-line of the wing, it can be readily plotted as against distance from the wing root[9]. As both the wing measurements and schlieren images provide information about a cross-sectional view of the model, we can superimpose the wing root heating data over the wing photograph of the schlieren images to illustrate how the shock impingements and flow features coincide with measured heating values on the wing, as shown in Figure 4-16.

Finally, Section 4.4 presents and discusses the heating measurements taken on the flat plate of the model. These measurements provide valuable insight into both the flow behaviour inside the recirculation regions occurring at the base of the wing and the conditions within the boundary layer forming over the leading edge of the model. By comparing analytical theory with flat plate measurements upstream of the recirculation region, Figure 4-17 and Figure 4-18 demonstrate that the observed conditions are broadly in line with theoretical conditions for similar topologies. The observation that flat plate measurements can be used to accurately detect the presence of unperturbed flow conditions (by comparing the heating values to theoretical conditions on a completely flat plate) is then used to predict the location and perimeter of the bow shock forming around the wing.

[8] See Appendix Section 6.2 for a discussion of fill conditions and details of individual shots.
[9] See Figure 4-10 for a visual representation of how distance from the wing-root is measured

4.1 Flow Conditions

While exact conditions could not be measured directly for each shot, they were calculated using the measured pressure at the end of the shock tube, just prior to flow expansion over the model in combination with the known topology of the nozzle used to expand the flow. Calculations were performed using the NENZFr program [19]. The resulting conditions alongside the standard conditions, based on Mach 8 flow at 30km altitude, are shown in Table 4.1. The values represent the mean of all shots excluding the first shot for the given condition (therefore excluding shots 11043 and 11053), with the tolerances indicating the absolute maximum deviation from the mean observed.

	Low Pressure Condition	High Pressure Condition	Standard Conditions
Temperature (K)	294.7 ± 27.8	376.9 ± 16.8	226.5
Pressure (kPa)	2.54 ± 0.10	4.89 ± 0.27	1.841
Density (kg/m^3)	0.026 ± 0.001	0.045 ± 0.002	0.0184
Total Enthalpy (MJ/kg)	3.31 ± 0.32	4.05 ± 0.16	2.91
Mach No.	7.37 ± 0.06	7.09 ± 0.18	8
Unit Reynolds Number (10^6/m)	3.6 ± 0.1	5.65 ± 0.15	2.92

Table 4.1: Test conditions for the low and high pressure condition, shown against atmospheric conditions at 30km altitude (summarised from Table 6.6).

The relative stability of observed conditions across the cumulative "low" and "high" pressure shots confirms repeatability of the tunnel and conditions, as well as demonstrating that tunnel conditions are an unlikely source of large discrepancies in results. Shots were selected for analysis based on the reliability of the data and repeatability of the shot[10]. The initial aim of the test campaign was to observe turbulent flow. After the initial low and high pressure shots failed to demonstrate clear turbulence, a trip was designed to attempt to induce turbulence in the boundary layer[11]. Shots were then repeated with the trip, until a complete set of low and high pressure shots had been conducted for low and high pressure conditions, and for sweep angles of 45°, 55° and 65°.

Figure 4-1 demonstrates graphically the effect of flow conditions on free-stream Mach and Reynolds numbers. It also demonstrates, based on Bushnell's criterion, that it would be unlikely for turbulence to develop at the low pressure regime, despite the presence of disturbances [23].

[10] See Appendix Section 6.2.3 for a discussion of shots selected for review.
[11] See Section 3.2.1 for trip specifications.

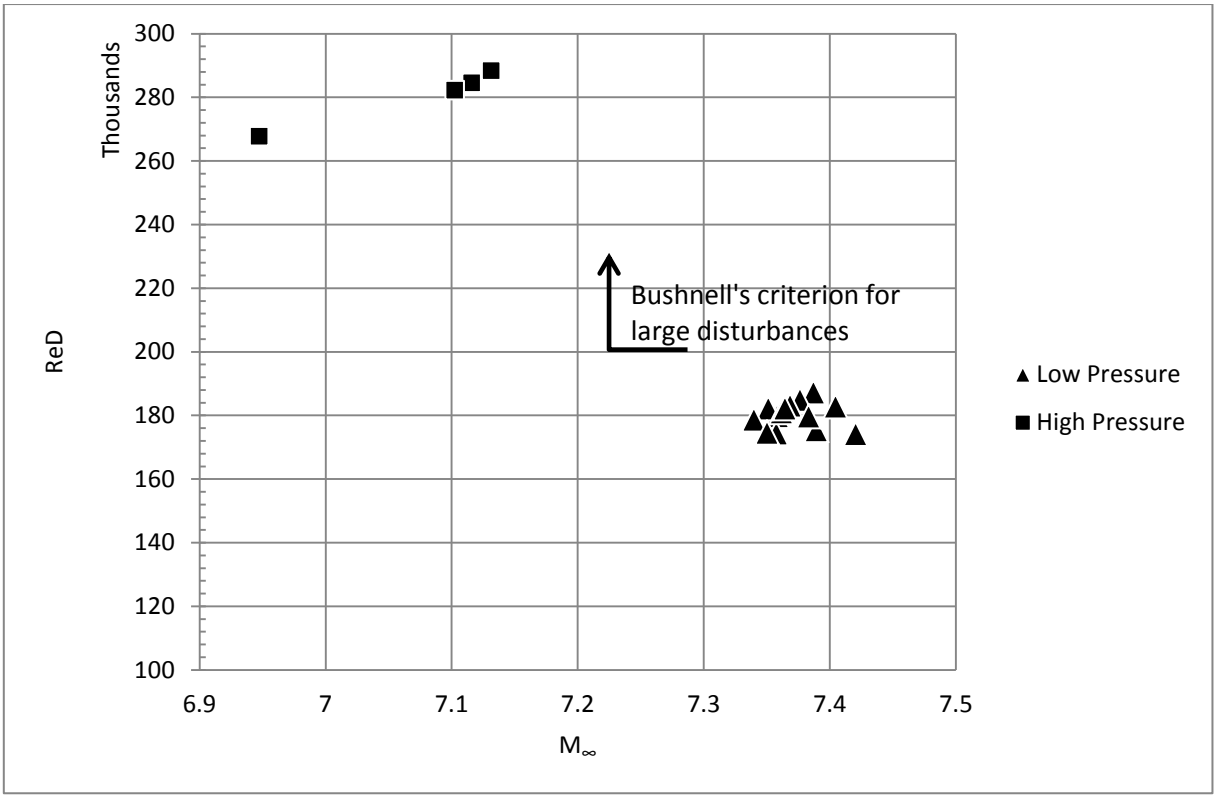

Figure 4-1: Scatterplot of free-stream Mach number against Reynolds number based on blunt wedge diameter (50mm). Bushnell's criterion for turbulent flow with large disturbances ($ReD = 0.2 \times 10^6$) is also shown [23]

4.2 Schlieren imagery

Schlieren images were taken through a window inside the test section, and show a cross-sectional view of the model during the test time. To fully utilise the limited pixel density of resulting images (1280×800 pixels), only the region in the immediate vicinity of the wing root interaction were photographed.

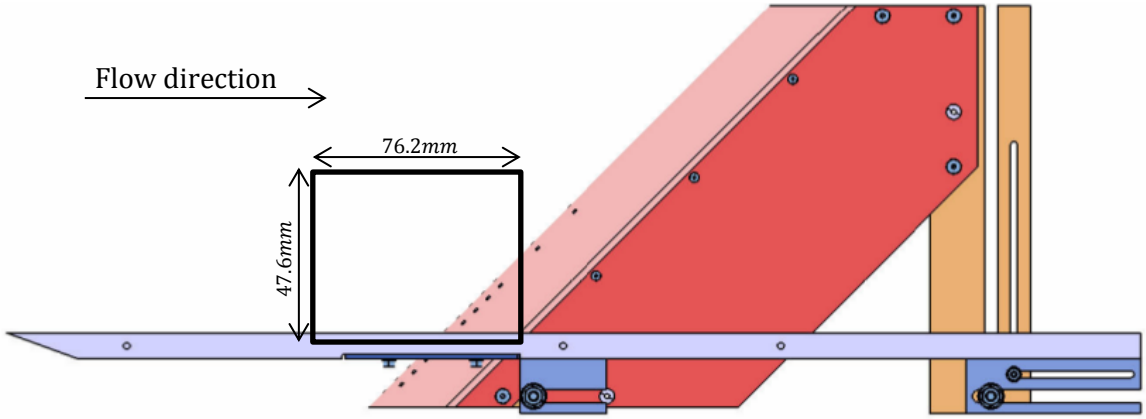

Figure 4-3: Cross-sectional size and location of the region captured by the schlieren photographs.

Schlieren images were taken at millisecond intervals over the test time. A catalogue of representative 45°, 55° and 65° shots at high and low pressure conditions is given in Figure 4-4, with each image taken at the respective test time for that shot. Note that due to vibrations, varying forces acting on the model mounts during the test time, and small changes in camera and lens position between shots there are small variations in the position of the viewport. The location represented in Figure 4-3 is based on the schlieren photograph obtained for shot #11063. The size legends in Figure 4-4 and subsequent measurements are configured individually for each shot based on reference photographs taken prior to each new shot configuration.

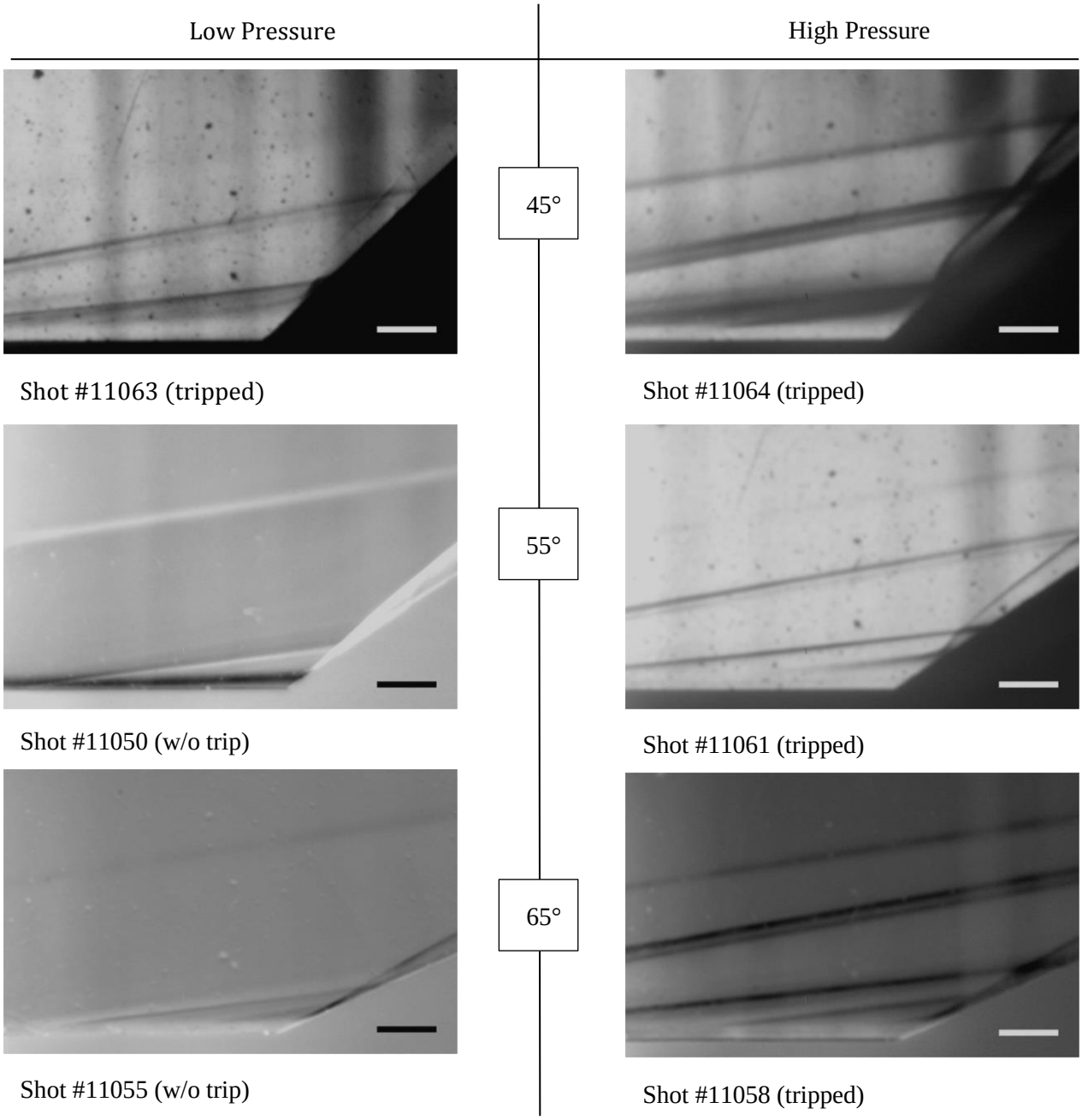

Figure 4-4: Schlieren images of test time for shots at each angle and pressure condition. The horizontal bar indicates dimensions of $10 \times 1\ mm$. Image negatives are provided where this improves image clarity.

The schlieren images provided valuable insight into the flow behaviour. To better understand the components of the images presented in Figure 4-4, Figure 4-5 identifies the features common to most of the images taken, using shot #11058 as a template.

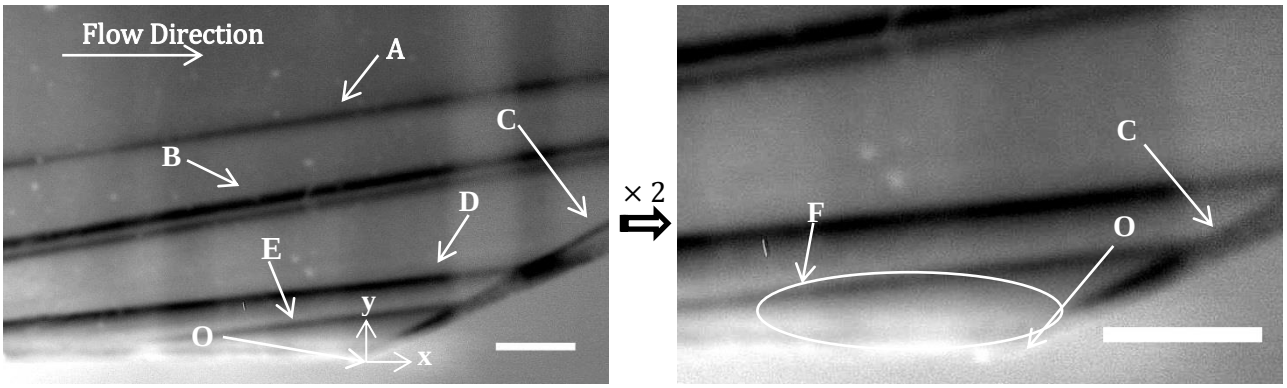

Figure 4-5: Schlieren image taken during test time of Shot #11058 (high pressure, 65° sweep, tripped) showing significant flow features. The features are; A) viscous interaction shock from leading edge, B) wave propagation from trip, C) bow shock across wing cylinder, D) wave generated by the flat plate insert[12], E) wave from recirculation region, F) approximate location of the recirculation region) and O) The location of the wing-root junction relative to which distances are measured. A rectangle indicating a region of size 10×1 mm and a x,y coordinate system are also shown.

Shock waves A, B and D are likely caused by the leading edge, trip and flat plate recess[12] respectively. Assuming that the images are geometrically consistent and that lens distortions are negligible, we can trace the locations of the oblique shock waves to help identify the source. The angle of each oblique shock wave is derived based on pixel locations in Figure 4-5. The angle of weak waves generated from surface imperfections or leading edges will propagate at an angle of $= \sin^{-1}\left(\frac{1}{M}\right)$. The free-stream Mach number implied by free-stream wave feature A, which appears at an angle of 8.22° to the horizontal, is 7.0. The measured free-stream Mach number for shot #11058 (depicted in Figure 4-5) was calculated at 7.1[13]. This small discrepancy of 1.4% is a good indication both that free-stream conditions were as expected and that the schlieren images are geometrically consistent.

At a sweep angle of 65° (as is the case in the image depicted in Figure 4-5), the wing does not perfectly align into the flat plate insert, and the wing-root junction is therefore approximately 5mm downstream of the theoretical location as per the design drawings (Figure 3-5). The leading edge of the flat plate is therefore ca. 205 mm from the apparent location of the junction in Figure 4-5. The distance of the shock source based on the apparent angle of shock wave A is 209 mm upstream, and within 2 % of the actual value. Feature B appears to originate from the trip, as it is not visible in tests where the trip was removed. Wave B appears to originate 131 mm upstream of the junction. The trip is located 140 mm upstream of the junction, and is therefore within less than 10 %. Given that the shock formations from the trip, as well as the

[12] See Figure 6-15 in Appendix Section 6.2.5 for an image of the backward facing step present on the flat plate insert.
[13] Derived flow conditions are shown in Table 6.6.

geometry of the trip itself, are complex, it is not expected that a visually observed shock wave could pinpoint the location of the trip with any greater accuracy.

Features A and B are therefore concluded to have been caused by the leading edge and trip respectively. The flat plate insert begins at 51 *mm*, and the distance between the apparent source of wave D and the spanwise backward facing step caused by the flat plate insert (as shown in Figure 4-5, feature A) is 16 *mm*; an error of 30 %. This suggests perhaps the RTV material used to seal the manufacturing defects (feature B in Figure 4-5), which extends several millimetres upstream of the backward facing step, could be responsible for this shock feature.

At the interaction of the bow shock (C in Figure 4-5) with the recirculation region (F in Figure 4-5), heat transfer on the wing surface is expected to peak. This region will be referred to as the primary shock impingement region. As the interaction of flow features C and F is relatively clear in almost all of the schlieren photographs, we can approximate the regions at which the recirculation region ends and the bow shock begins to form, as has been done in Table 4.2. Figure 4-6 illustrates how these measurements were obtained, with shot #11064 as an example. As can be seen from this figure, the exact locations of these features are often not clear, and the regions between the primary shock impingement and recirculation region could instead be taken to represent upper and lower bounds of where the shock impingement might is expected to have taken place across the test time.

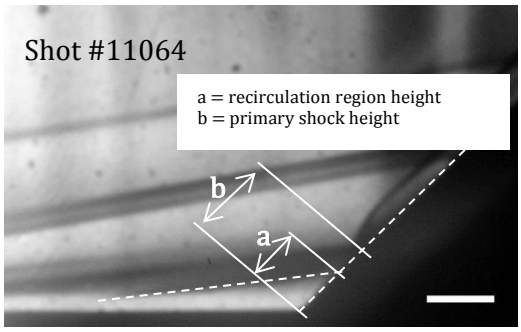

Figure 4-6: Illustration of how the recirculation region height and "primary" shock height are measured, using shot #11064 as an example. Results are shown in Table 4.2.

Shot #	Sweep Angle	Pressure	Trip	Recirculation region height	Primary shock height
11044	45°	Low	No	4.7mm	9.8mm
11063	45°	Low	Yes	7.3mm	14.5mm
11064	45°	High	Yes	5.4m	11.9mm
11050	55°	Low	No	4.9mm	10.1mm
11062	55°	Low	Yes	7.9mm	15.1m
11061	55°	High	Yes	6.5mm	14.8mm
11055	65°	Low	No	6.6mm	13.6mm
11060	65°	Low	Yes	9.1mm	17.9mm
11058	65°	High	Yes	7.7mm	16.3mm

Table 4.2: Approximate primary shock impingement location and recirculation region size based on analysis of schlieren photography.

Several interesting observations can be drawn from the results of Table 4.2. The pressure of the flow appears to reduce the recirculation region size for tripped flows at any given sweep angle. Conversely, for a given pressure, the inclusion of the trip significantly increases the recirculation region size. These effects are clearly illustrated in Figure 4-7, which plots the recirculation region size for all conditions listed in Table 4.2. We can also confirm the increased size of the recirculation in the images of Figure 4-4, which show a clear increase in recirculation region size for a given condition when a trip is added to the model.

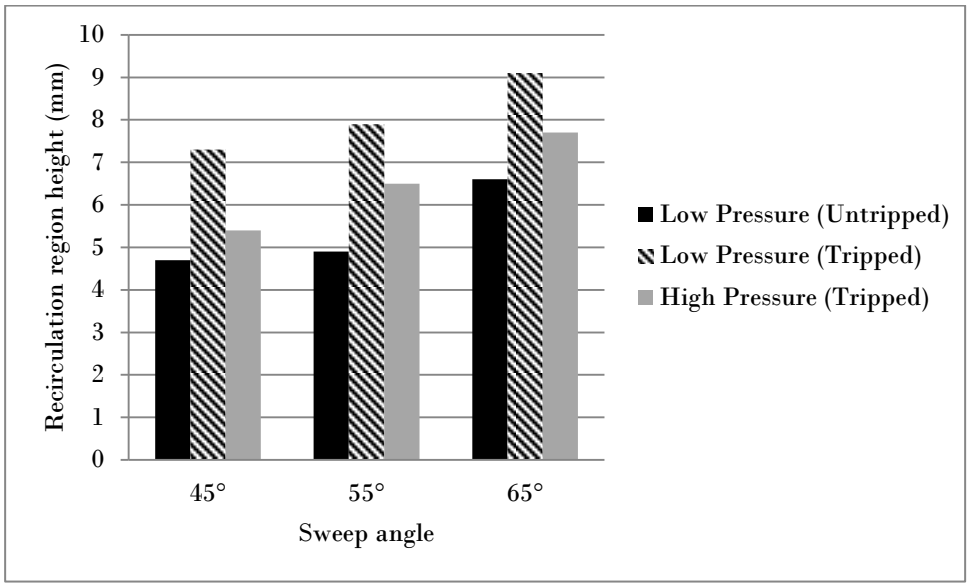

Figure 4-7: Recirculation region size (from Table 4.2)

As can be seen in Figure 4-8, the effects of both pressure and tripped conditions on the primary shock impingement position are similar to those observed for the recirculation region size. Sweep angle increases the impingement location, inclusion of a trip substantially increases it, and higher pressure slightly reduces its size. As the primary mechanism for fluid transfer past the blunt wedge is the vortical structures observed as recirculation regions in the schlieren imagery, the above result correlate closely with the expectation that decreasing sweep angles should correspond to larger recirculation regions.

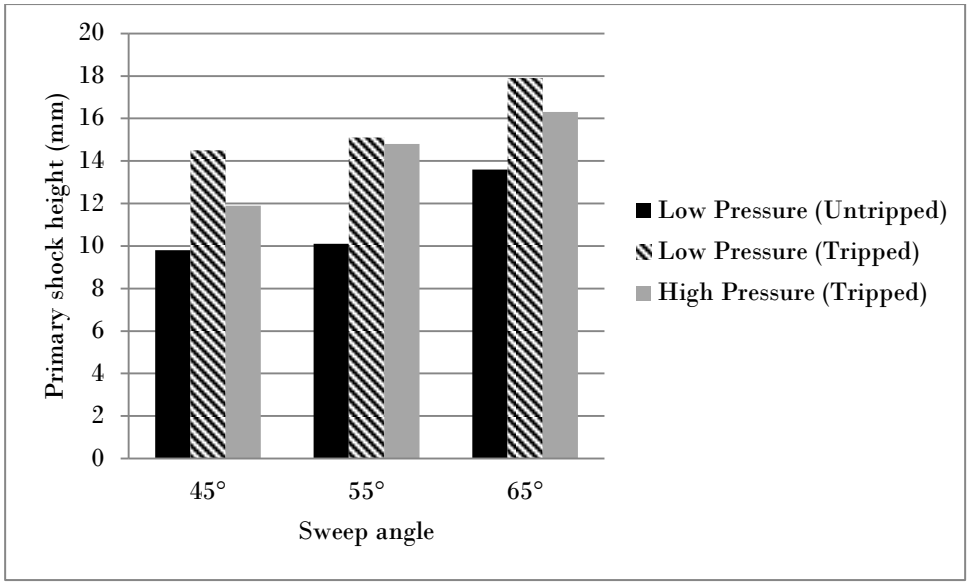

Figure 4-8: Primary shock impingement location (from Table 4.2)

Similar patterns are observed for the location of the shock impingement, as would be expected since the shock is formed by flow passing over the recirculation region.

It should be reiterated however, that while the figures shown in Table 4.2 and plotted in Figure 4-7 and Figure 4-8 provide some insight into the effect of experiment conditions on the size of the recirculation region, they are somewhat subjective.

The following section will attempt to reconcile the observations made from the schlieren imagery with wing heating data.

4.3 Wing Heating Data

This section will discuss results obtained from measurements on the wing itself. Measurements on the flat plate (the blue region in Figure 4-9) will be discussed in Section 4.4.

The thermocouples mounted on the model wing proved to be more resilient to high heat flux and debris than the thin film gauges, and provided relative heat transfer data for all of the 6 data points for most shots[14]. Due to configuration faults, the data obtained from gauges on the wing could only be used to obtain relative values, and no absolute heat transfer measurements could be obtained[15]. Additionally, a directly linear relationship between two relative wing heating values cannot be assumed.

[14] For a discussion on why only relative values are included here refer to Appendix Section 6.1.2.3.
[15] See Appendix Section 6.1.2.3 for a discussion on thermocouple gauge failure.

With only the thermocouples producing usable data on the wing surface, the only remaining data from the wing is in a linear configuration along the centreline. These thermocouple locations represent gauge recesses 64-69[16] and are represented on the model at a 45° sweep configuration in Figure 4-9. The relative position of the gauges relative to the wing changes with each sweep configuration, and the exact locations of heat transfer data are therefore represented individually for each shot. Note that gauge recess 64 is underneath the flat plate at the 45° sweep configuration and therefore not visible in Figure 4-9.

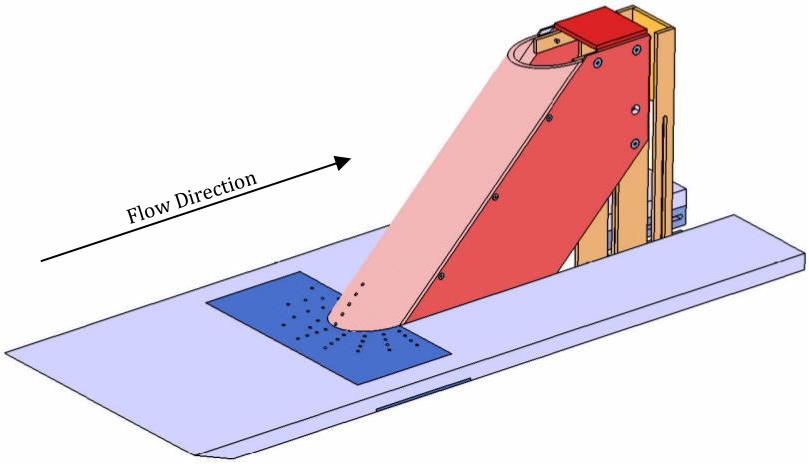

Figure 4-9: Isometric view of the model design at 45° sweep angle excluding thin film wing recesses (the gauges in these recesses, as visualised in Figure 3-4, were destroyed within the test time of the first shot)

As relative gauge locations on the wing depend on sweep angle, the heating profile along the wing is plotted against the distance from the wing root for each sweep configuration. This allows for meaningful comparison of thermocouple data across multiple configurations and against the schlieren images.

[16] See Figure 6-12 in the appendix for gauge recess locations on the wing

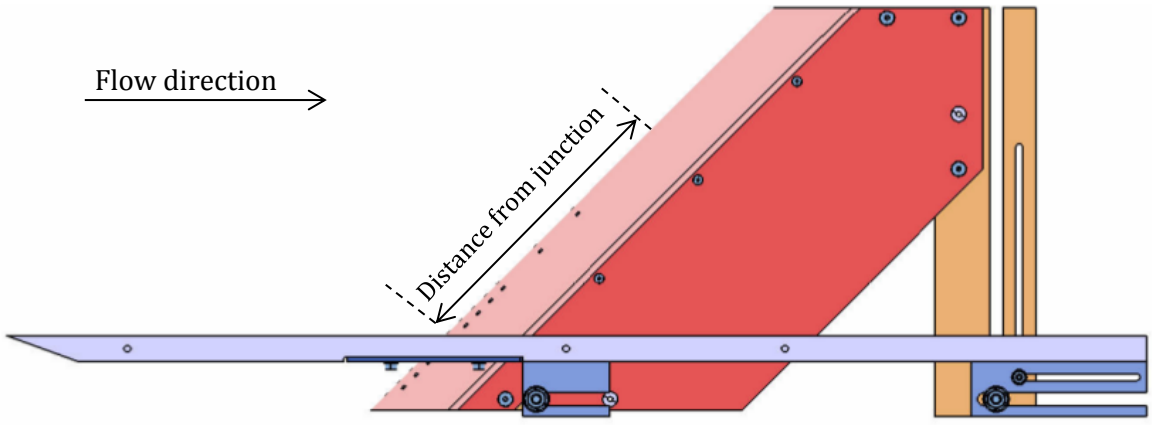

Figure 4-10: Illustration of how the distance from the wing-root is obtained for plotting thermocouple data in Figure 4-13 and Figure 4-15.

We can now superimpose these locations over the wing heating rates obtained from thermocouple data, plotted on an axis of distance from the wing-root junction (as per Figure 4-10).

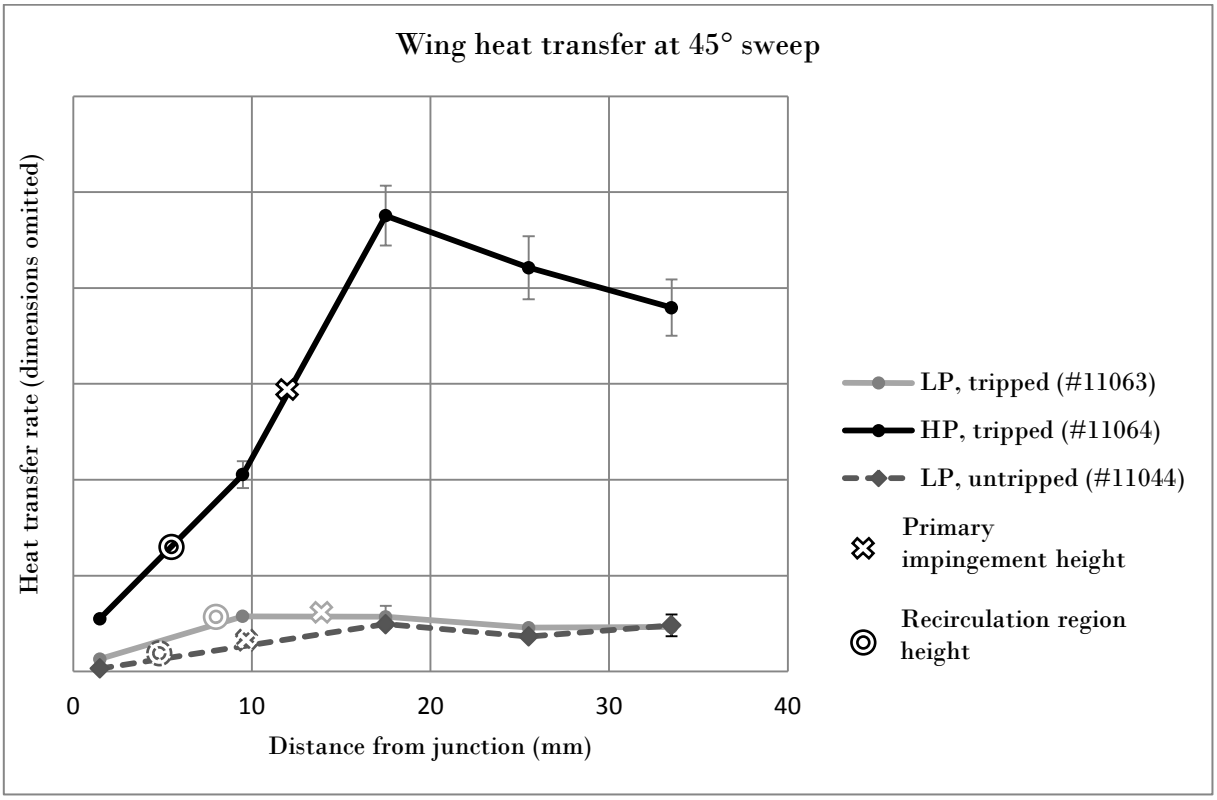

Figure 4-11: Wing heat transfer data at 45° sweep, showing the location of the primary impingement and recirculation region as per Table 4.2. Note that the thermocouple at 9.8mm failed for shot #11044.

The impact of conditions on wing heating data is illustrated in Figure 4-11, which shows low pressure tripped, high pressure tripped, and low pressure untripped heat transfer data. The stark difference in heating rates between the low and high pressure condition is immediately apparent and expected, given that the stagnation enthalpy of the high pressure flow is substantially higher. The difference between tripped and untripped flows for the low pressure condition is not particularly noticeable as we move away from the junction. This confirms that the effect of the trip is limited to the vicinity of the junction by the Mach wave propagation rate. For the tripped, low pressure condition the 2nd thermocouple failed during the test, resulting in a missing data point for this series. It is interesting to note that the primary shock impingement occurred directly at the location of that thermocouple, perhaps explaining why it failed.

The primary shock impingement always occurred in the vicinity of the highest thermocouple reading, demonstrating that the shock impingements were likely responsible for the peak readings observed in their vicinity.

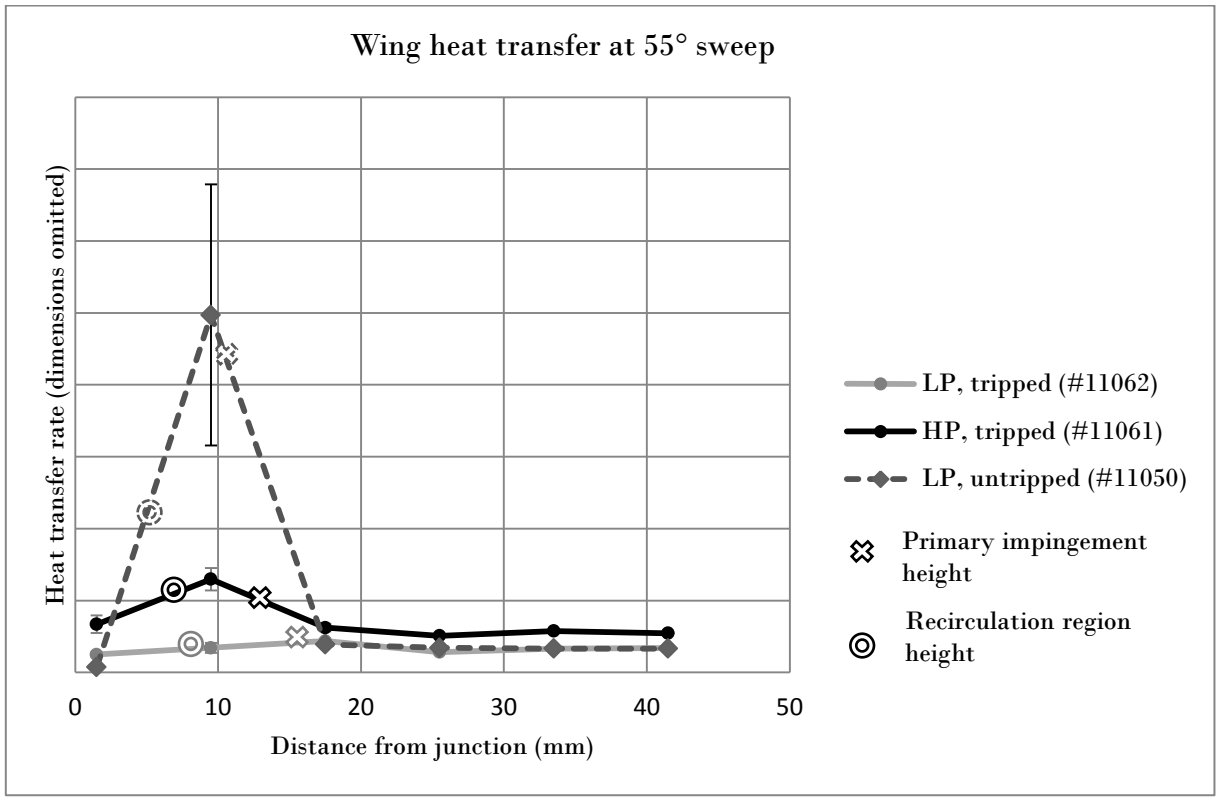

Figure 4-12: Wing heat transfer data at 55° sweep, showing the location of the primary impingement and recirculation region as per Table 4.2.

The wing heat transfer readings at 55° demonstrate, again, that heat flux at large distances from the junction do not vary substantially by the inclusion of the trip. As the trip does not appear to

affect upstream wing heat transfer, and since the trip is shown to trigger transition under the low pressure condition[17] based on flat-plate heat transfer measurements, these results suggest that flow is turbulent on the wing under all conditions (as turbulent flow on the flat plate would be unlikely to transition to a laminar regime as it passes over the wing).

An interesting observation from Figure 4-12, however, is the very large peak heating rate in the vicinity of the primary impingement location at the low pressure, untripped condition. The observation that other shots where the impingement was close to the thermocouple did not register such high readings demonstrates that a shock impingement is likely responsible for the heating. Additionally, the very high standard deviation of the signal suggests that the shock was not stable and instead intermittently passing over the gauge. A wave formed over a recirculation region would exhibit this behaviour.

Unfortunately, the primary shock impingement locations do not match precisely with the peak heating rates. This could be due to imperfect image geometry of the schlieren images from which these locations were extracted, or small, unaccounted differences in geometry of the model. Particularly, at sweep angles above 45° the wing has about 1-2mm of space to slide along the axis of flow direction.

The shock features inferred from the schlieren images could be readily matched with the model or flow feature from which they originated[18]. Due to the limited window size it was not possible to infer details of the shock interaction regime from these images.

[17] See Figure 4-19 for the effects of the trip on flow transition.
[18] See Section 4.2 for a review of schlieren data.

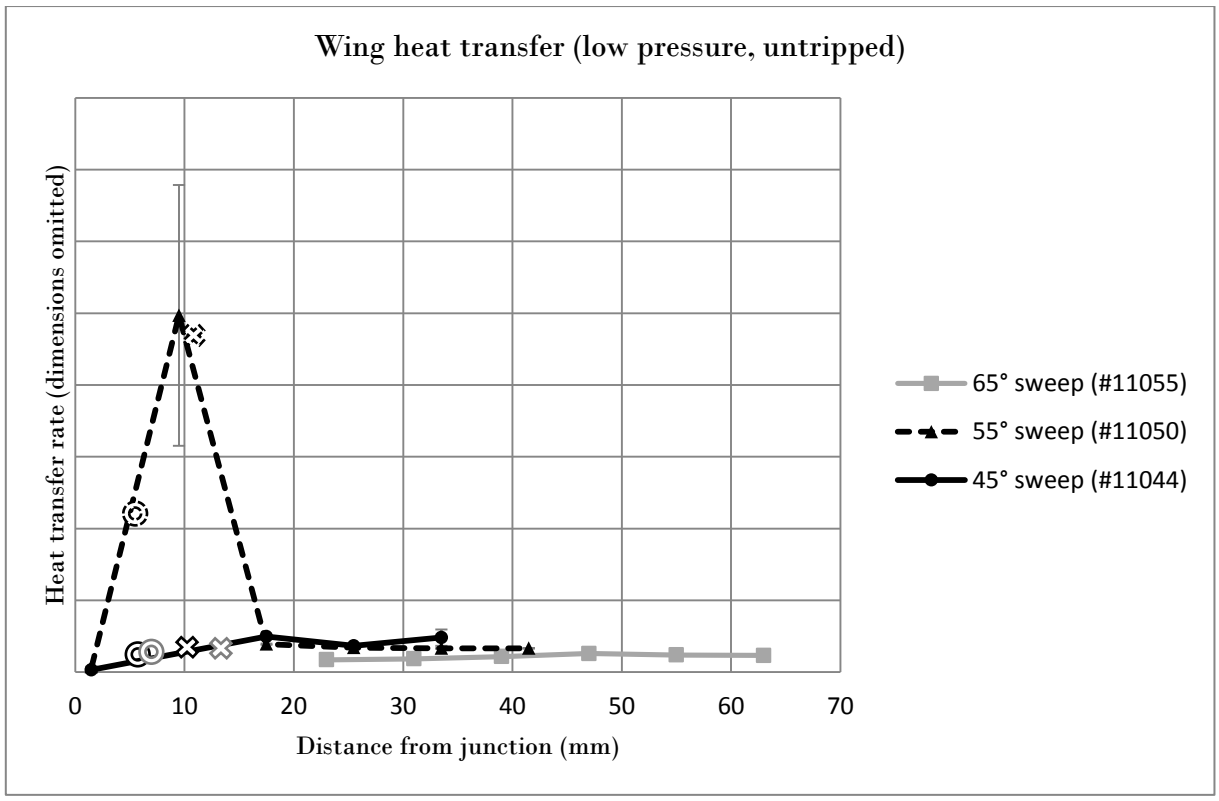

Figure 4-13: Wing heat transfer and signal standard deviation readings for low pressure, untripped conditions at various sweep angles, superimposed with the location of recirculation region and primary impingement heights (from Table 4.2).

The behaviour of the heat transfer profile for low pressure, untripped conditions (as illustrated in Figure 4-13 is broadly as expected, with the heat transfer profile settling at a rate in inverse proportion to the sweep angle. The prominent feature, however, is the substantially larger heat transfer rate observed for the 55° sweep case, which could also be seen in previous charts[19]. This is almost certainly due to a coincidental location of the thermocouple at the primary shock impingement region for that condition. To highlight this, Figure 4-14 shows the wing heat transfer for the two low pressure, untripped, 55° sweep conditions at which all thermocouples remained intact for the duration of the shot.

[19] Figure 4-12 also shows this prominent heat transfer rate for the 55°, low pressure, untripped case.

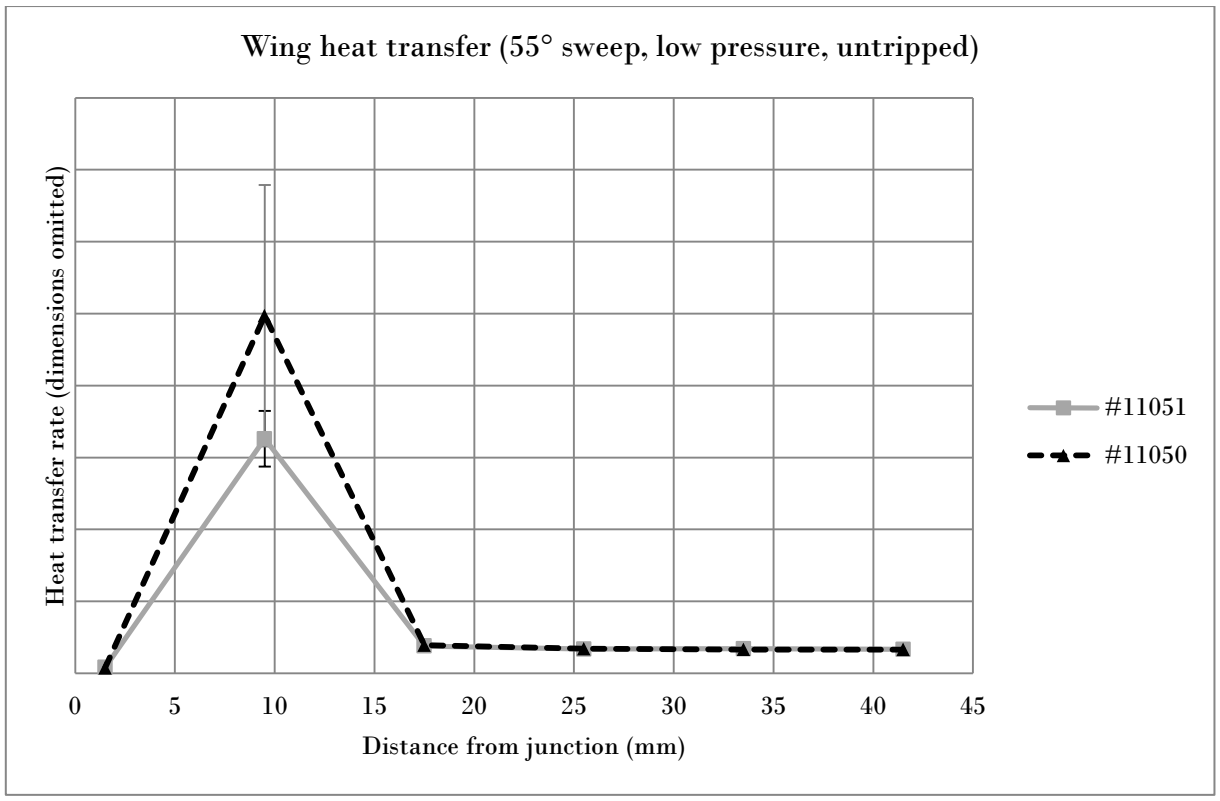

Figure 4-14: Wing heat transfer and standard deviation readings for low pressure, untripped, 55° sweep angle shots.

The extremely tight correlation at high distances from the junction suggests that the flow is steady and repeatable at this condition. The significant variation seen at 10mm (at the point of the primary shock impingement as per Table 4.2) indicates substantial variance in the size of the recirculation region, both in within a single test (as indicated by the large standard deviation in the signal) and between shots (as indicated by the variation between shot #11050 and #11051).

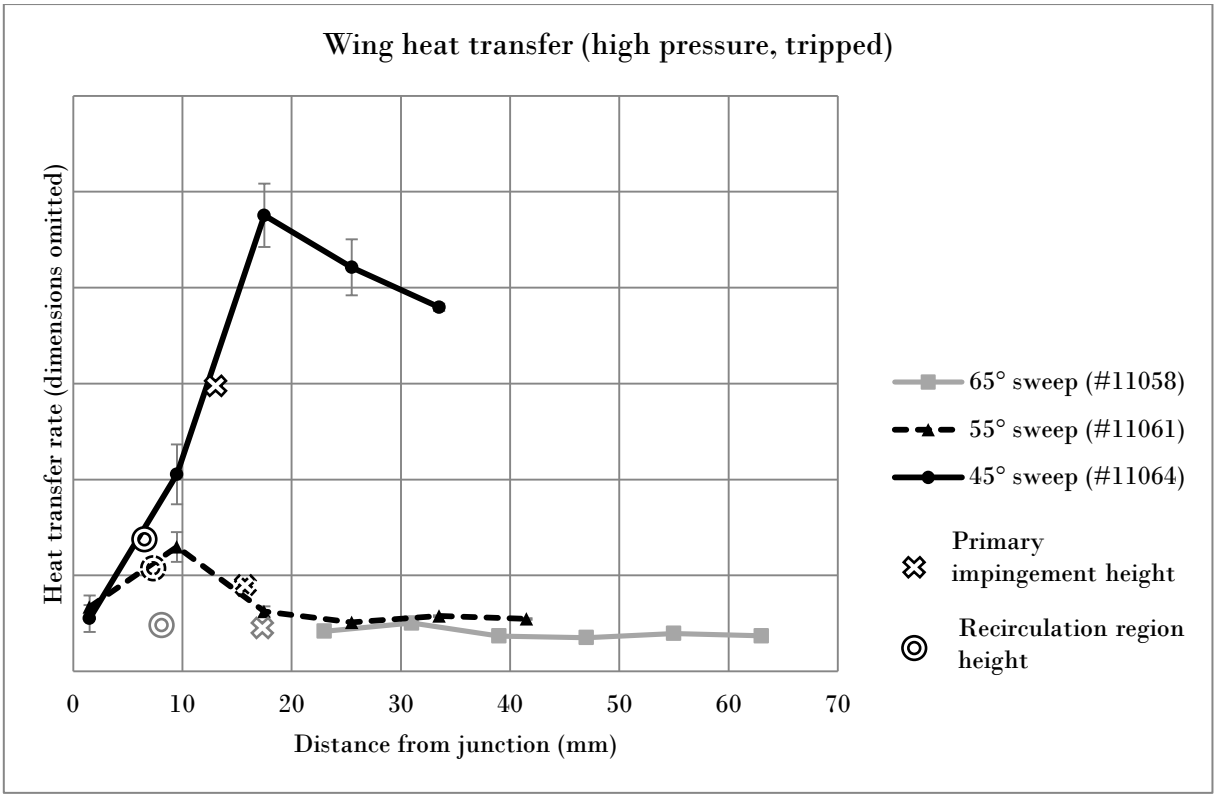

Figure 4-15: Wing heat transfer readings for high pressure, tripped conditions at various sweep angles, superimposed with the location of recirculation region and primary impingement heights (from Table 4.2).

Several observations can be made about the results obtained from heat transfer data on the wing in conjunction with the recirculation region data obtained from schlieren imagery:

1. Increasing sweep angle increases the distance of shock impingement from the junction.
2. Higher pressure conditions consistently reduce the size of the recirculation region.
3. Within the recirculation region, measurements are consistent with heating rates increasing as we move away from the junction, although there are insufficient gauges in several instances to infer this directly.
4. Peak heating occurs due the shock forming over the recirculation region impinging on the wing. The position of this impingement varies in proportion to recirculation region size and sweep angle.
5. Heating rates stabilise with increasing distance away from the junction and shock impingement.

While the lack of confidence in the absolute value of the thermocouple readings is unfortunate, it is certainly interesting to observe the shock impingement location supports the thermocouple

results. Physically, one would expect heating along the wing to be persistently high within the recirculation region, as is strongly observed in both the thermocouple and flat plate readings. Shock impingement would be expected to cause localised peak heating in the vicinity, or slightly upstream of, the bow shock interaction with the "primary" shock[20], with the heating rate decreasing as the bow shock offset increases with larger distances from the wing root [24]. Given that the large spike in heat flux across the discontinuity would almost certainly be missed by the thermocouple (perhaps with the exception of shot #11061 in Figure 4-15), one would expect the shock impingement location as per the schlieren images to occur before peak heating recorded by the thermocouples, except for when the thermocouple records the actual shock impingement (as occurs in shot #11061). As these phenomena are directly observed in Figure 4-13 and Figure 4-15, this suggests that the thermocouple readings are reliable in terms of their relative heat transfer readings, as well as demonstrating that the resolution of the thermocouple spacing is insufficient.

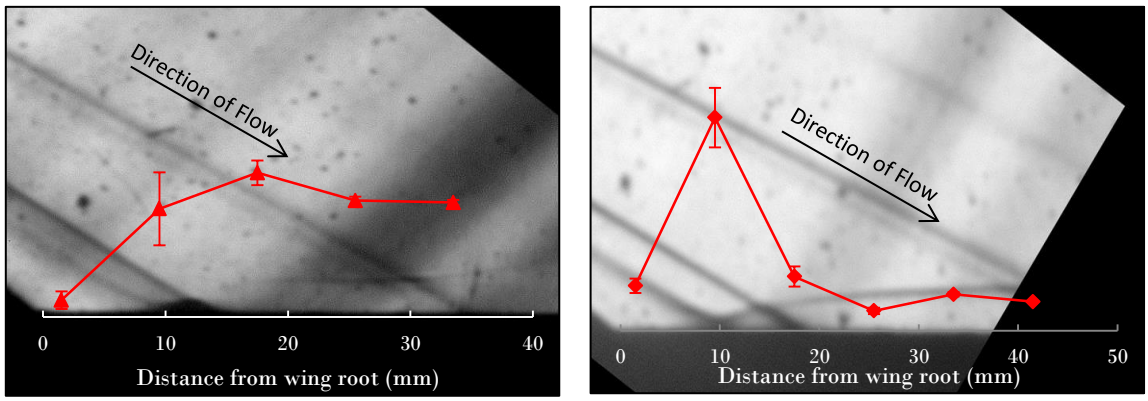

Figure 4-16: Thermocouple heat transfer rate (with dimensions omitted) plotted over schlieren imagery aligned by angle and distance from wing root. Left: Shot #11063 (45° sweep, low pressure). Right: Shot #11061 (55° sweep, low pressure).

The superimposed images of the thermocouple data aligned over the schlieren imagery are shown in Figure 4-16. Note that the schlieren photographs have been rotated clockwise against the sweep angle so that the wing in the photograph aligns with the thermocouple readings. These images further illustrate that the observed heating rates, at least near the recirculation region, depend highly on the distribution of the thermocouples. In Figure 4-16 (left) the thermocouple is located slightly within the recirculation region (at ~10mm), so that it does not measure the effects of the shock impingement. The effect of this impingement is demonstrated Figure 4-16 (right), where a high peak is observed where a shock wave impinges the wing surface very close to where the thermocouple is located.

[20] The primary shock feature originates from the leading edge, which is not visible in the photographs. It is features E in Figure 4-5

4.4 Flat plate measurements

Gauges in the centreline of the flat plate ahead of the recirculation region appeared to provide consistent results throughout the campaign, perhaps due to their relative distance from the surface discontinuities which may have been responsible for the irregularities observed on the port and starboard sides of the model (these will be discussed in Section 0). These centreline gauges, with reference to Figure 3-8, include gauges 12, 13, and at times 14 and 15 – depending on the size of the recirculation region and availability of gauges at any given shot.

The mean heat transfer rates observed over the test time for the flat plate centreline are plotted against Reynolds numbers for low and high pressure shots in Figure 4-17, demonstrating the rather stark effect that the trip had on the heat transfer observed on the surface.

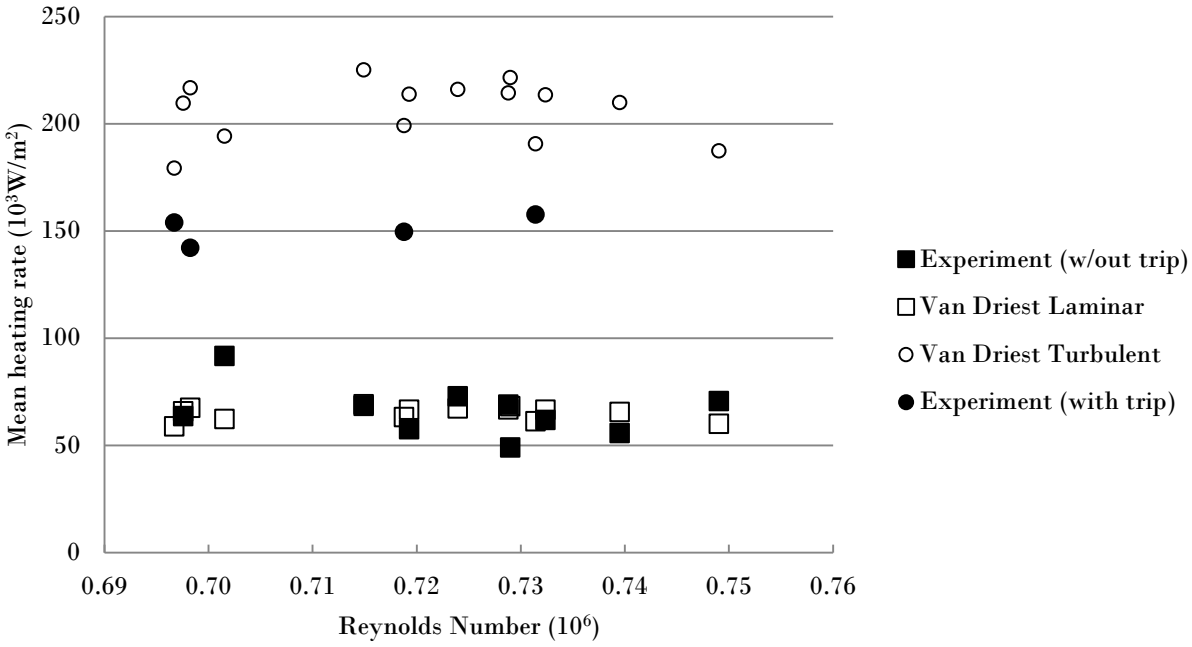

Figure 4-17: Heat transfer along the centre-line of the flat plate plotted against Reynolds number based on leading edge length (200mm) for all low pressure shots, with Van Driest solutions taken from measured flow conditions.

It should be noted that the apparent outlier for the experimental results without a trip (the 2nd black square from the left in Figure 4-17) corresponds to shot 11055: the result of Figure 4-22 where an apparently high heat flux is observed upstream of the interaction. This is more likely due to contaminants on the surface than some unaccounted physical phenomenon.

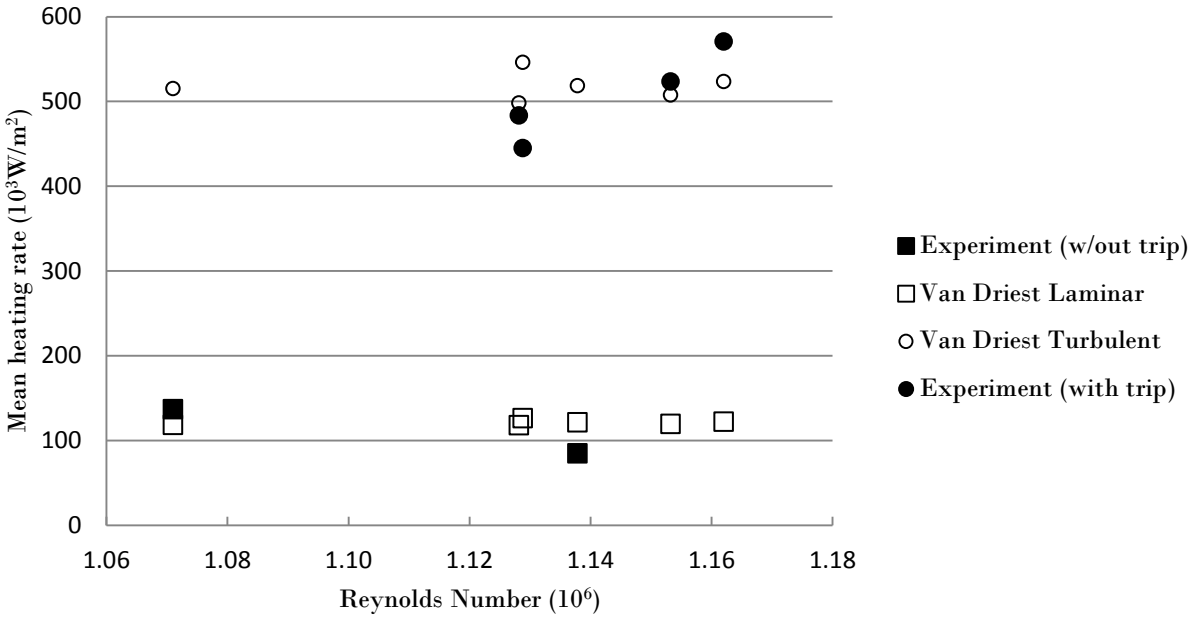

Figure 4-18: Heat transfer along the centre-line of the flat plate plotted against Reynolds number based on leading edge length (200mm)for all high pressure shots, with Van Driest solutions taken from measured flow conditions.

Figure 4-17 and Figure 4-18 present several interesting observations. They demonstrate quite conclusively that the trip has a defined and consistent impact on flow transition. The effect of flow condition (high vs low pressure) is quite limited in terms of its effects on Reynolds numbers, and the fact that the flow appears to remain laminar between low and high pressure conditions therefore does not come as a surprise. While the number of samples is small, it does appear that the heat transfer rates where a trip is employed are very closely aligned to the Van Driest solutions for turbulent flow in the high pressure condition, but consistently below the theoretical solution for the low pressure condition. This might indicate that the flow is transitioning in the low pressure condition when a trip is present.

In order to better visualise the behaviour of the flow leading up to the junction, Figure 4-19 shows the centre-line flat plate heating measurements leading up the junction (gauge recesses 12-15 with respect to Figure 3-8). It was not possible to obtain meaningful plots along the centreline of the flat plate for 55° and 65° sweep configurations (due to the wing physically blocking the wing recesses from underneath the model, making it impossible to install more than 1 or 2 gauges at these configurations).

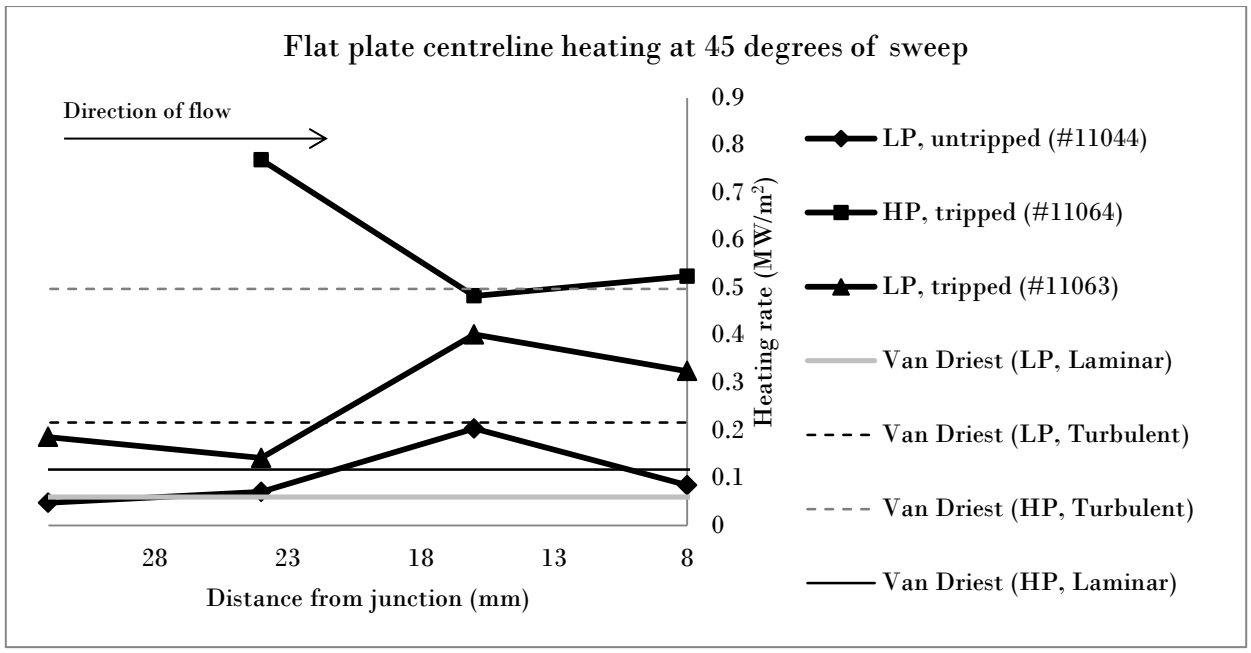

Figure 4-19: Heat transfer along the centreline of the flat plate for various flow conditions at 45° sweep, including Van Driest laminar and turbulent solutions.

While it is difficult to infer clear trends with the limited amount of data available, several observations can be made from Figure 4-19. The low pressure, untripped condition appears to correspond well with the Van Driest solution for the given conditions. At 16mm, a strong peak occurs where the bow shock interacts with the gauge. Afterwards, the heating rate appears to decrease to a heating rate between the laminar and turbulent solution for the free-stream flow. As was already observed from Figure 4-17, the tripped, low pressure flow appears to be in a state of transition, showing a heating rate somewhat below the turbulent solution, again spiking at around 16mm downstream of the junction and subsiding at 8mm. The high pressure, turbulent case exhibited a broken gauge at 32mm. Interestingly, the peak heating rate appears to occur farther downstream than the lower pressure case. This is an unexpected result, although it is possible that this result is an outlier caused by the aforementioned surface imperfections.

4.4.1 Contour-plot representation of untripped surface temperature readings

Due to the symmetrical nature of the model, it was initially expected that heat flux measurements at symmetrically positioned recesses would be similar, thereby allowing us to superimpose the heat flux readings from each side to the other on the resulting images. By observing the time-accurate heat flux at symmetrically located flat plate recesses it was, however, found that only shots prior to the installation of the trip recorded symmetrical heat flux measurements[21]. For this reason, and due also to the relatively low resolution of gauges on the flat plate, only heat flux maps of shots 11044, 11049 and 11055 could be reliably represented visually. While the expected "horse-shoe" shock formation could be visualised, the regions where heat flux was expected to be most severe (closest to the wing root) could not be measured directly as the gauges were not close enough to the wing (this was an unfortunate limitation as gauges too close to the wing would be crushed from underneath by the protruding bottom edge in lower sweep angles (see Figure 3-5). As the recirculation region passes over the wing and toward the downstream region of the flat plate, the formation dissipates and becomes measurable by the downstream gauges. This is well illustrated in the heat flux map of shot 11044, a low pressure condition at 45° sweep (Figure 4-20).

[21] For a discussion on flow asymmetry, likely causes, and the reasons for exclusion of certain test data see Appendix Section 6.2.5.

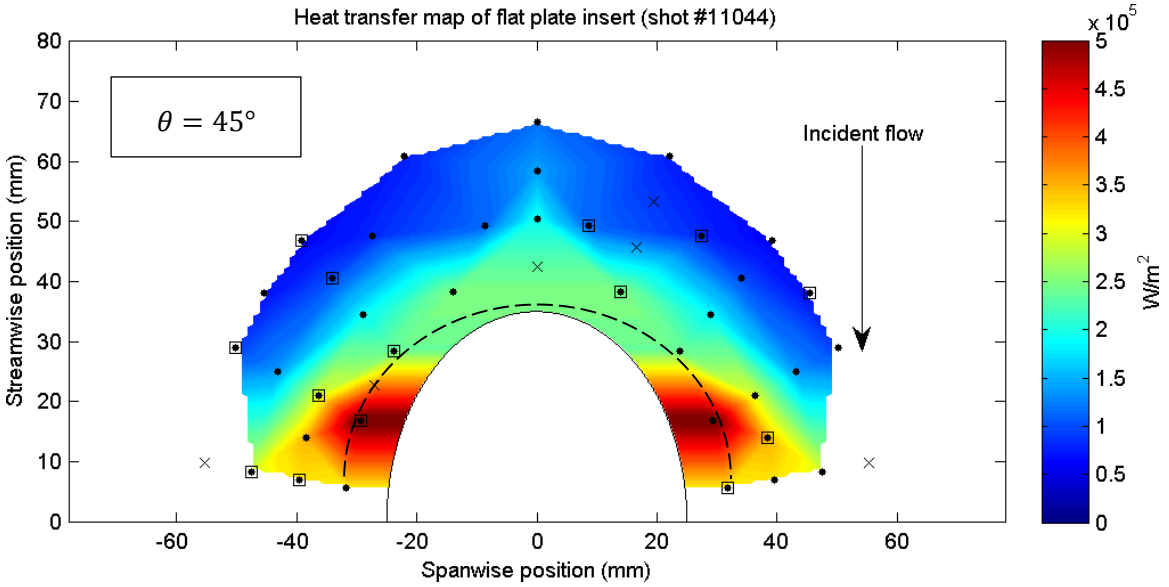

Figure 4-20: Symmetric heat transfer plot of the flat plate section of the model at a low pressure, untripped, 45° sweep condition. Gauge locations (black dots), symmetrically superimposed locations (black dot inside square) and invalid gauges (black cross) are shown. The dashed line represents what a typical "horseshoe" shaped recirculation region might be expected to look like at a wing root.

Higher sweep angles resulted in lower intensity of peak heat flux, as expected. This is reflected quite clearly in the heat flux maps for shots 11049 and 11055, which represented low pressure shots at wing sweep angles of 55° and 65° of sweep respectively. These are shown in Figure 4-21 and Figure 4-22.

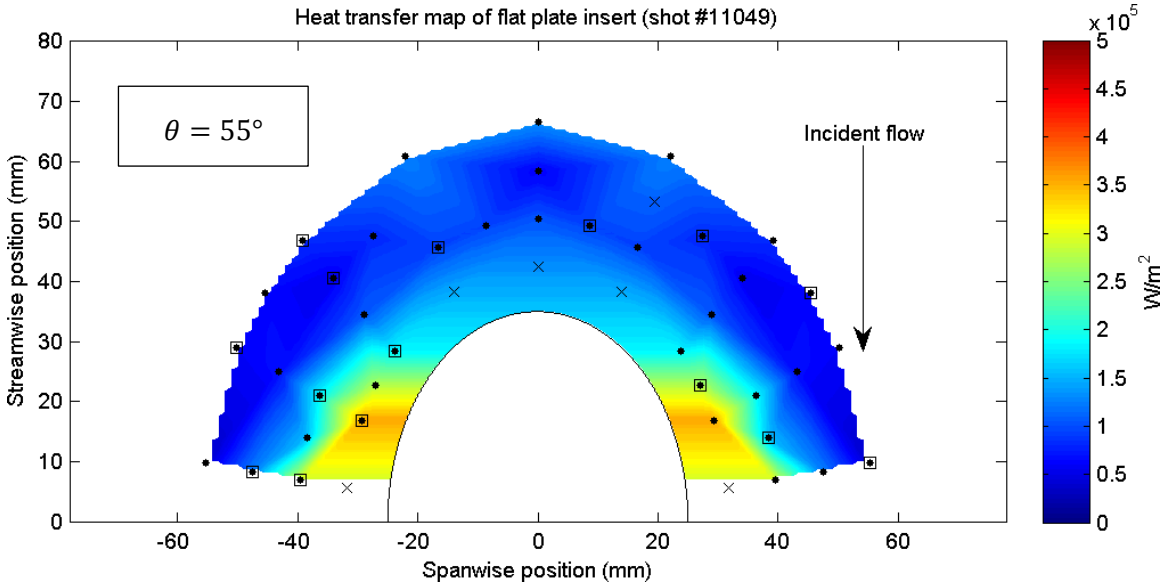

Figure 4-21: Symmetric heat transfer plot of the flat plate section of the model at a low pressure, untripped, 55° sweep condition. Gauge locations (black dots), symmetrically superimposed locations (black dot inside square) and invalid gauges (black cross) are shown.

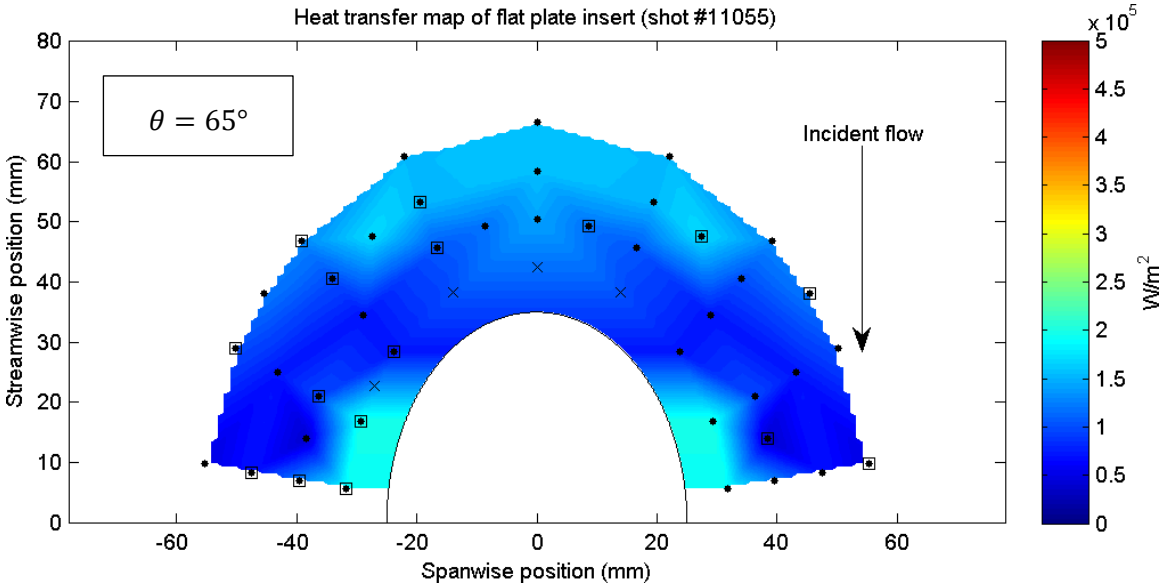

Figure 4-22: Symmetric heat transfer plot of the flat plate section of the model at a low pressure, untripped, 65° sweep condition. Gauge locations (black dots), symmetrically superimposed locations (black dot inside square) and invalid gauges (black cross) are shown.

The increase in heating at the upstream end of the flat plate (most clearly visualised in the upstream gauges of Figure 4-22) was caused by unintentional surface imperfections, which

perturbed the flow and appeared to produce local heating rate increases. Based on the consistently laminar flow conditions and reliability of the trip to trigger transition of the flow (see Figure 4-18) the effects of these surface imperfections appear to be constrained to the gauges in their immediate vicinity[22].

4.4.2 Quantifying bow shock topology

Due to physical constraints, the thin film gauges could not be placed sufficiently close to the wing-root junction at the centreline of the model, and therefore the only region where the gauges would be expected to consistently interact with the peak heating that the plate would experience due to the recirculation region are further downstream (gauges 1-3 and 24-31 with reference to Figure 3-8). While the high intensity heating zones are readily observed, as can be seen in Figure 4-20, the actual peak heating value is rather elusive, as it can only be measured if the bow shock passes over the exact location of the gauge.

With reference to Figure 6-11, gauge recesses 1-3 and 24-31 are exposed to the full spanwise range of the bow shock region as it passes over the downstream section of the flat plate insert. Figure 4-23 and Figure 4-24 show the heating rate of the gauge recording the highest heating rate at any given condition.

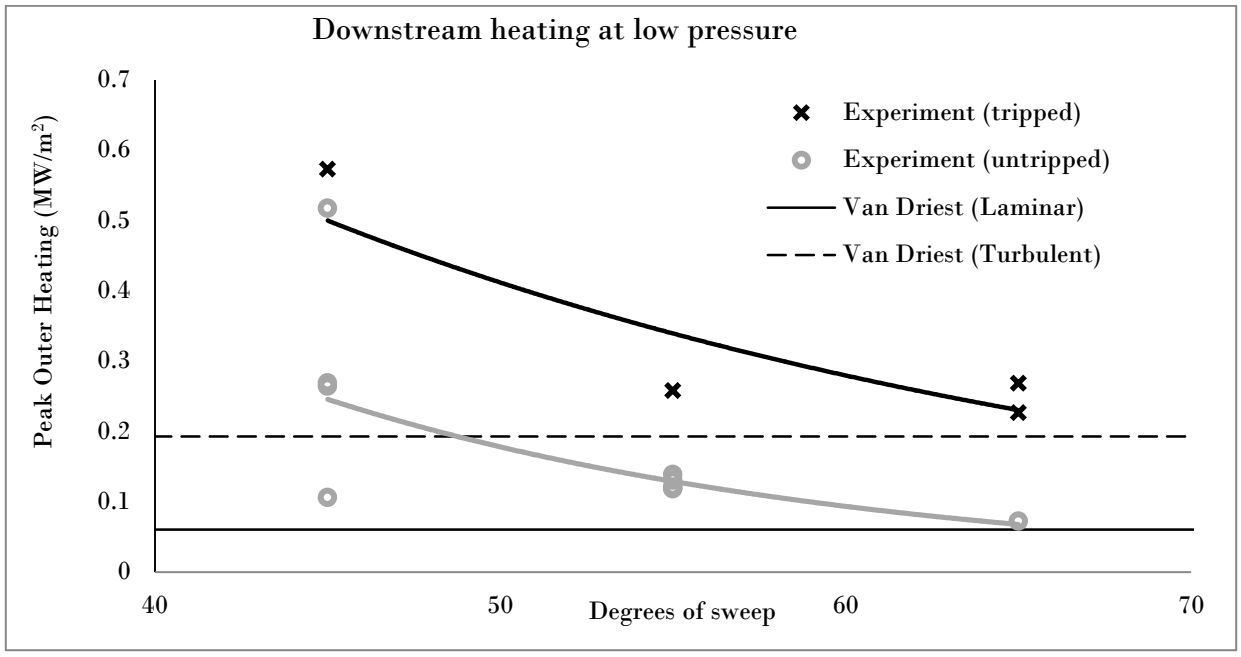

Figure 4-23: Peak flat plate heating from downstream gauges during test time for tripped and untripped low pressure conditions, showing the turbulent and laminar Van Driest solutions for the respective conditions.

[22] For a discussion on the observed asymmetry of the flat plate heat transfer measurements and its causes refer to Appendix Section 6.2.5

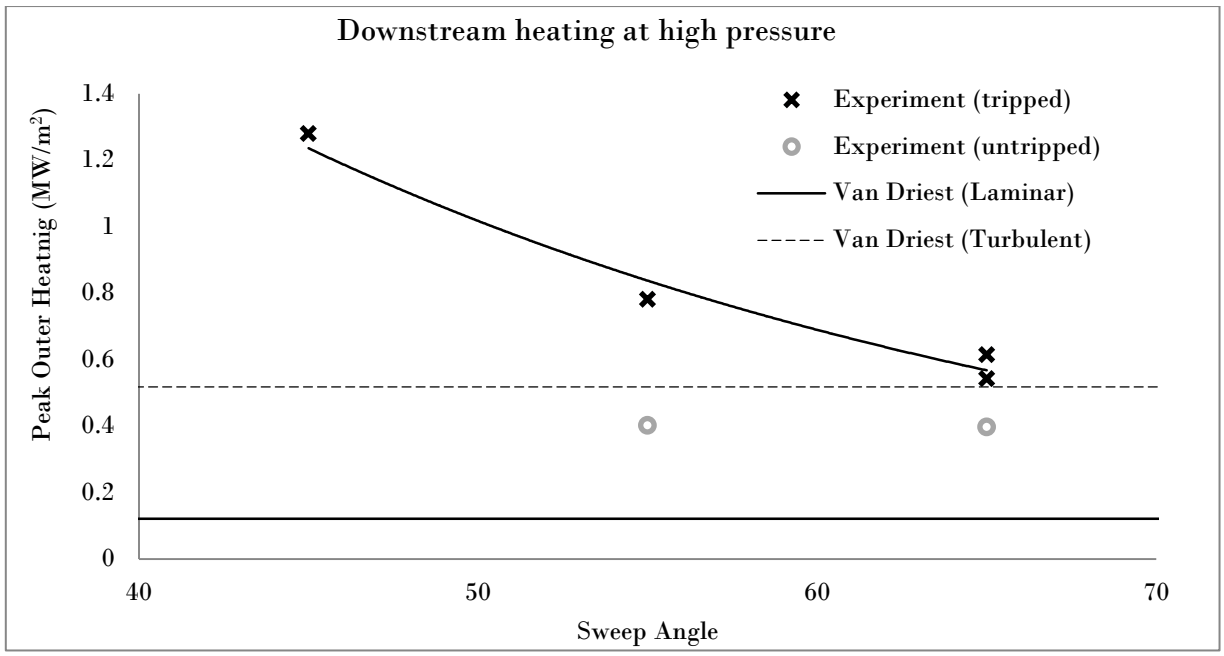

Figure 4-24: Peak flat plate heating from downstream gauges during test time for tripped and untripped high pressure conditions, showing the turbulent and laminar Van Driest solutions for the respective conditions.

The high scattering of the peak heating rates, which is particularly apparent in the untripped, low pressure readings from Figure 4-23, is an unfortunate consequence of the apparently insufficient resolution of the thin film gauges.

As the recirculation region varies in size, we might expect a scattering of peaking heating rates if the width of the feature, as the region subjected to the bow shock will depend highly on flow condition, sweep angle, and the time at which the test time data sample was recorded (the latter accounting for variation between shots of similar flow condition). The peak heating measured will therefore only occasionally reflect actual peak heating. A continuous distribution of surface heat flux gauges would be expected to produce a distribution of heating results varying from the heating rate inside the bow shock to the peak heating experienced at the shock interaction zone.

As sweep angle increases, one would expect the peak heating rate to asymptote to the heating experienced on a flat plate experiment of equal condition. Such heating can be readily calculated for both laminar and turbulent conditions using the Van Driest method of flat plate heating[23].

[23] See Appendix Section 6.3 for a derivation of the Van Driest method for flat plate turbulent boundary layer heaing.

For the low pressure experimental conditions (Figure 4-23) there appears to be a clear trend towards an asymptote at or near the laminar and turbulent Van Driest solution for the untripped and tripped experiments respectively. This confirms the hypothesis that the trip did in fact cause the flow to become turbulent, as was observed from Figure 4-17 and Figure 4-18.

For the high pressure conditions (Figure 4-24) the trend is less apparent although still evident, at least for the tripped experiments. As only 2 experiments were conducted for the untripped high pressure conditions, there is insufficient data to infer a trend. However, given that Figure 4-18 has already demonstrated that the Van Driest turbulent solutions fit very well (within 10%) with experimental data, it seems unlikely that the heating rates observed for the untripped high pressure condition are present in turbulent flow. While a trend cannot be inferred directly from these two datapoints, it seems much more likely that this flow exists in a region *laminar* flow which has been perturbed by imperfections on the upstream surface.

CHAPTER 5

Summary and Conclusions

The experimental campaign of this thesis was able to observe the behaviour, particularly heat transfer rates, resulting from interactions at wing-root junctions at or approximating conditions of atmospheric flight at 30km altitude near Mach 8.

With reference to the research questions proposed in Chapter 1, this section will address the research questions individually, with a view to address them in light of the experimental and analytical results of the present study.

Despite the asymmetries observed in several of the experiments, this study was successful in demonstrating the effectiveness and limitations of the Van Driest solution for laminar and turbulent flow on a flat plate. Specifically, it successfully predicted heating rates for both laminar and turbulent flow at the high pressure condition to within ~15%[24]. The Van Driest laminar solution also performed well at predicting laminar heating rates for the low pressure experimental condition, again to within ~15% with the exception of one outlier[25].

The accuracy and predictive power of the Van Driest solution for those conditions was certainly acceptable, and given that the average values were extremely close to the theoretical values, this suggests that perhaps the discrepancies are rather the product of variation in experimental conditions and measurements than inherent inaccuracies in the Van Driest relations themselves.

Interestingly, the Van Driest solution performed comparatively poorly against the tripped flow at the low pressure condition. There is a consistent tendency of the Van Driest solution to overestimate the heating rate for this condition (see Figure 4-17). A likely explanation for this behaviour is that the trip only generated transitional flow behaviour at the low pressure condition immediately downstream of the trip.

This is supported by the heating rates measured across a variety of conditions, with heating rates consistently either clearly laminar for untripped conditions, or at or below the Van Driest turbulent solution for tripped flows.

The experiments therefore demonstrated that a 2mm saw-blade trip placed spanwise across a flat plate at least 100mm upstream of the region of interest was able to consistently trigger flow transition for the conditions measured, although the low pressure condition might have been

[24] For a graphical representation of the laminar and turbulent heating rates of the high pressure test condition against the Van Driest solutions refer to Figure 4-18

[25] For a graphical representation of the laminar heating rates of the low pressure test condition against the Van Driest solution refer to Figure 4-17.

near the threshold of the flow conditions under which turbulence could be easily triggered, given that the flow appeared to require more than 100mm to achieve turbulence.

5.1 Research Question 1

How do the significant features of the flow vary with experiment configuration?

Schlieren imagery proved immensely useful in understanding the significant features of the flow. By observing the size of the recirculation region and shock impingements we were able to plot the relationship between sweep angle, pressure, and size of the recirculation. Table 4.2, and resulting plots shown in Section 4.2 clearly demonstrate that transition/turbulence has a profound and direct effect on both the size of the recirculation region and the height of the resulting shock impingement on the wing. Conversely, increasing flow pressure reduces the size of these features, compressing the recirculation zone.

Higher sweep angles appeared to increase the location on the wing at which shock impingement and recirculation region contact occurs. This is of course an expected outcome, as the height of a given location on the wing decreases with increasing sweep. The actual size of the recirculation region decreases with increasing sweep angle, as can be observed from Figure 4-4. From an aerodynamic design perspective, this finding demonstrates that impinging shock heating both decreases in magnitude and increases in lateral position with increasing angles of sweep.

5.2 Research Question 2

How do the flow features affect peak heating on the flat plate?

Schlieren imagery obtained during the test time of each experiment was in strong agreement with the profile of heat transfer measured over the wing, with strong indication that the thermocouples were a good indicator of relative heat transfer over several shots, despite the absolute value of their reading likely being incorrect. This suggested that the pixel gradients observed in the schlieren imagery did in fact represent the density gradients of shock waves forming over the recirculation region. The present work was therefore able to visually quantify the effects of turbulence, sweep angle and flow condition on the area and height of the resulting recirculation region at the base of the wing root.

The thermocouple data from the wing did however succeed in providing a relative view of the heat transfer profile along the wing. The profile of heat transfer extending away from the wing root was as expected, with a trough at the base of the wing where surface is insulated by the recirculation region, a peak at the shock impingement and end of the recirculation region, and a stabilisation of the heat transfer at the regions outside of the effects of the wing-root interaction.

On the flat plate, Figure 4-17 and Figure 4-19 demonstrated that the flow was unperturbed at 30mm upstream of the plate for all conditions, with heat transfer rates predicted accurately by the Van Driest solution at these positions. The bow shock causing peak heating appeared to perturb the flow at approximately 16mm upstream of the junction for the low pressure condition. Interestingly, heating rates appeared increase farther upstream for the *higher*

pressure condition. It was difficult to infer whether this is a repeated trend given that the centreline gauges plotted in Figure 4-19 were only installable for the 45 degree sweep configuration.

The transition in the flat plate heating profile observed by Figure 4-20, Figure 4-21 and Figure 4-22 demonstrates that the intensity of heating is substantially affected by sweep at low angles. At 65 degrees of sweep, the magnitude in variation between unperturbed laminar flow and peak heating near the wing is within 20% of the difference in heating between unperturbed laminar and unperturbed turbulent flow.

While the wing data was not used to infer absolute values, it was successful in also demonstrating the response of the heat transfer profile on the wing in response to changes in flow condition and sweep angle. The response was broadly as predicted, with the measured heat transfer response in positive correlation with flow pressure and in negative correlation with sweep angle.

A general observation both on the wing and the flat plate is that heating within the bow shock/recirculation region is higher than the freestream, but actual peak heating varies substantially not only with condition but within a single test, highlighting the fickle relationship between the recirculation region size and the resulting shock impingement on the wing, as was observed by the large standard deviation in signal magnitude of Figure 4-14.

5.3 Closing Remarks

The present study succeeded in qualitatively answering the research questions, although the unfortunate failure of instrumentation on the wing of the experimental model caused a significant quantity of data to be rendered unusable. In addition, surface imperfections on the flat plate of the model caused a second crucial set of measurements – the flat plate heat transfer data – to be partially impacted. These unforeseen sources of error have unfortunately reduced confidence in some of the quantitative results of this study.

Despite these hindrances, sufficient reliable data remained from the test campaign to allow for substantial insight into the effect of heat transfer on various wing configurations and flight conditions.

One of the key lessons learnt in the course of this project is the importance of incremental checks against theoretical solutions throughout gauge construction and during early experimental tests. While the loss of thin film gauges was not unexpected, the difficulties in deriving accurate temperature readings from thermocouples on the surface of the wing could likely have been avoided if the model had been subject to a known heat source prior to conducting the experiment. These results could have been used to verify the accuracy of the measurements and, if inaccuracies were found, assist in the diagnosis of sources of error. Such an analysis is not possible retrospectively, and had such precautions been taken the issues experienced in this study could likely have been avoided. The inconsistencies in heat transfer

rates observed on the surface of the flat plate could have been addressed if thorough heat transfer analyses were conducted after each experiment, as opposed to simple resistance checks.

Future study should focus on a rigorous test campaign to not only isolate and remove the sources of error identified in the present study (namely surface imperfections affecting incoming flow and erroneous thermocouple data) but also extend the test conditions over a wider range to fully develop a predictive empirical tool. Such a tool would provide invaluable information to engineers by reducing safety factors and error tolerances during design considerations.

Bibliography

[1] J. Weil, “Review of the X-15 Program,” NASA, Langley, 1962.

[2] US Air Force, “X-51A Waverider, U.S. Air Force graphic,” US Air Force, Virginia, 2010.

[3] University of Queensland, “HIFiRE Program,” 2012. [Online]. Available: hypersonics.mechmining.uq.edu.au/hifire. [Accessed 10 02 2014].

[4] E. Walth, “Design of the experiment model for the project: "Experimental Study of hypersonic wing/fin root heating at Mach 8",” The University of Queensland, Brisbane, 2011.

[5] L. Gipson, “Glossary,” 5 September 1996. [Online]. Available: http://www.hq.nasa.gov/pao/History/presrep95/bb.htm. [Accessed 21 11 2013].

[6] E. R. Van Driest, “The Problem of Aerodynamic Heating,” *Aeronautical Engineering Review,* pp. 26-41, 1956.

[7] E. R. Van Driest, “On the Boundary Layer with Variable Prandtl Number,” *Jahrbuch der Wissenschaftlichen Gesellschaft fur Luftfahrt,* pp. 66-75, 1954.

[8] G. R. Eber, “Recent Investigation of Temperature Recovery and Heat Transmission on Cones and Cylinders in Axial Flow in the N.O.L. Aeroballistics Wind Tunnel,” *Journal of the Aeronautical Sciences, Vol. 19, No. 1,* pp. 1-6, 1952.

[9] T. Von Karman, “The Analogy Between Fluid Friction and Heat Transfer,” *ASME, Vol. 61, No. 11,* 1939.

[10] H. B. Squire, “Heat-Transfer Calculations for Aerofoils,” British Air Ministry, Rep. and Memo

No. 1986, London, 1942.

[11] J. K. Wideman, J. L. Brown, J. B. Miles and O. Ozcan, "Skin-Friction Measurements in Three-Dimensional, Supersonic Shock-Wave/Boundary-Layer Interaction," *AIAA Journal Vol. 33, No. 5,* pp. 805-811, 1995.

[12] L. H. Tanner and L. G. Blows, "A Study of the Motion of Oil Films on Surfaces in Air Flow, with Application to the Measurement of Skin Friction`," *Journal of Physics E: Scientific Instruments,* pp. 194-202, 1976.

[13] D. Gaitonde and J. Shang, "Structure of a Supersonic Three-Dimensional Cylinder/Offset-Flare Turbulent Interaction," *Journal of Spacecraft and Rockets,* pp. 294-302, 1997.

[14] J. A. Fay and F. R. Riddell, "Theory of Stagnation Point Heat Transfer in Dissociated Air," *Journal of the Aeronautical Sciences, Vol. 25, No. 2,* pp. 73-85, 1958.

[15] I. E. Beckwith, "Local Heat Transfer and Recovery Temperatures on a Yawed Cylinder at a Mach Number of 4.15 and High Reynolds Numbers," National Advisory Committee for Aeronautics, Washington, 1962.

[16] R. J. Stalker, "Recent Developments with Free Piston Drivers," in *17th International Symposium on Shock Waves and Shock Tubes*, 1989.

[17] M. V. Suraweera, "Reduction of Skin Friction Drag in Hypersonic Flow by Boundary Layer Combustion," The University of Queensland, Brisbane, 2006.

[18] R. M. Kirchhartz, "Upstream Wall Layer Effects on Drag Reduction with Boundary Layer Combustion," The University of Queensland, Brisbane, 2009.

[19] P. Jacobs and R. Gollan, "NENZFr," 2012. [Online]. Available: http://www.mech.uq.edu.au/cfcfd/nenzfr.html. [Accessed 05 January 2013].

[20] P. Condie, “User Manual - Test Data Acquisition.VI,” St. Lucia, 2010.

[21] D. L. Schultz and T. V. Jones, “Heat-transfer measurements in short-duration hypersonic facilities,” NATO Advisory Group for Aerospace Research and Development, Oxford, 1973.

[22] Master & Young, “PTA-110 Manual,” Brisbane, 2004.

[23] National Oceanic and Atmospheric Administration, “U.S. Standard Atmosphere, 1976,” National Aeronautics and Space Administration, United States Air Force, Washington, D.C., 1976.

[24] J. D. Anderson Jr., Hypersonic and High-Temperature Gas Dynamics, American Institute of Aeronautics and Astronautics, 2006.

[25] W. H. Heiser and D. T. Pratt, Hypersonic Airbreathing Propulsion, American Institute of Aeronautics and Astronautics, 1994.

[26] A. Higgins, Comparison of Engineering Correlations for Predicting Heat Transfer in Zero-pressure-gradient Compressible Boundary Layers with CFD and Experimental Data, Fishermans Bend: DSTO Defence Science and Technology Organisation, 2008.

[27] F. P. Incropera, D. P. DeWitt, T. L. Bergman and A. S. Lavine, Fundamentals of Heat and Mass Transfer, 6th Edition, John Wiley & Sons, 2007.

[28] R. G. Morgan, I. Lourel and D. R. Buttsworth, “Fast response coaxial type-E thermocouple gauges for the measurement of heat flux in expansion tubes,” University of Queensland, University of Southern Queensland, Brisbane, 2001.

[29] Omega.com, “Physical Properties of Thermoelement Materials,” 2005. [Online]. Available: http://www.omega.com/temperature/Z/pdf/z016.pdf. [Accessed 01 September 2012].

[30] J. D. Cox, D. D. Wagman and V. A. Medvedev, “CODATA Key Values for Thermodynamics,”

Hemisphere Publishing Corporation, New York, 1989.

[31] NASA, "VULCAN," 11 July 2012. [Online]. Available: http://vulcan-cfd.larc.nasa.gov/. [Accessed 4 August 2012].

[32] F. M. White, Viscous Fluid Flow, New York: McGraw-Hill, 1974.

[33] E. R. G. Eckert and R. M. Drake, Heat and Mass Transfer, 2nd ed, New York: McGraw-Hill, 1959.

[34] D. B. Spalding and S. W. Chi, "The drag of a compressible turbulent boundary layer on a smooth flat plate with and without heat transfer," *Journal of Fluid Mechanics Volume 18,* pp. 117-143, 1964.

CHAPTER 6

Appendix

6.1 Instrumentation notes

This section contains general notes about instrumentation and experiment-specific details as referenced in the report.

6.1.1 Thin Film Gauges

This section outlines construction, calibration and quality control procedures for the implementation of thin film gauges. For a discussion on theory and the motivation for their use refer to Section 3.3.

6.1.1.1 Construction

In practice, the construction of the thin film gauges is highly precise work, requiring meticulous accuracy in applying the metal film and the thin gold strips that conduct electrical signals from the connecting wires to the metal film on the gauge. While the application of the metal film (in this case nickel) is greatly facilitated by the Auto 500 Sputtering System, the conducting gold film must be applied by hand using a thin brush and high purity gold paint.

The first step in constructing the gauges is to place 17-19 quartz rods of 2mm width into acrylic tubes with 1cm diameters. The quartz rods and acrylic tube are each roughly 30cm in length. The empty spaces between the rods and acrylic tube are filled with cyanoacrylate glue and allowed to set overnight. The tube is then cut into 6mm segments using a high precision rotary blade. These disks are then glued to flat acrylic plates in lots of 7 (accounting for roughly 120 quartz substrates), and polished on rotating beds with incrementally finer polishing paper grit sizes of 240, 600 and finally 1200. After polishing and carefully inspecting the discontinuities in the quartz after each change in grit size, the disks are polished with a silk bed and 6μm diamond paste. The disks are then submerged in acetone for a period of 6 hours, allowing the cyanoacrylate glue to dissolve. The 6mm segments, which form the gauge substrate material, are then lightly etched in hydrofluoric acid to clean the surface of impurities and soften any remaining discontinuities in the quartz surface.

The substrates are then painted on both lateral sides with gold paste to form the conducting strips as per *b* in Figure 6-1. The painted substrates are then baked at 800°C to allow for the suspension agents in the gold paste to fully evaporate, leaving a thin gold layer on the substrates. Once painted with gold paste and baked to allow the particulates in the paint to evaporate, the substrates are the placed in a mount, with the front end of each sensor facing 0.5mm wide slots. The mounted substrates are then placed in the Auto 500 Sputtering System and sputtered with nickel, where electrical current is used to magnetically force ionised atoms of nickel from a pure nickel target onto the quartz substrates (referred to as DC sputtering). The

Auto 500 Sputtering System is set to sputter 1kÅ of nickel onto the substrate, which will yield an expected resistance of approximately 100Ω across the film – the ideal value for the amplifiers used to convert the resistance into a digital signal. This yields a strip of width 0.5mm and length 2mm as defined by the width of the slots in the mount and the diameter of the substrates.

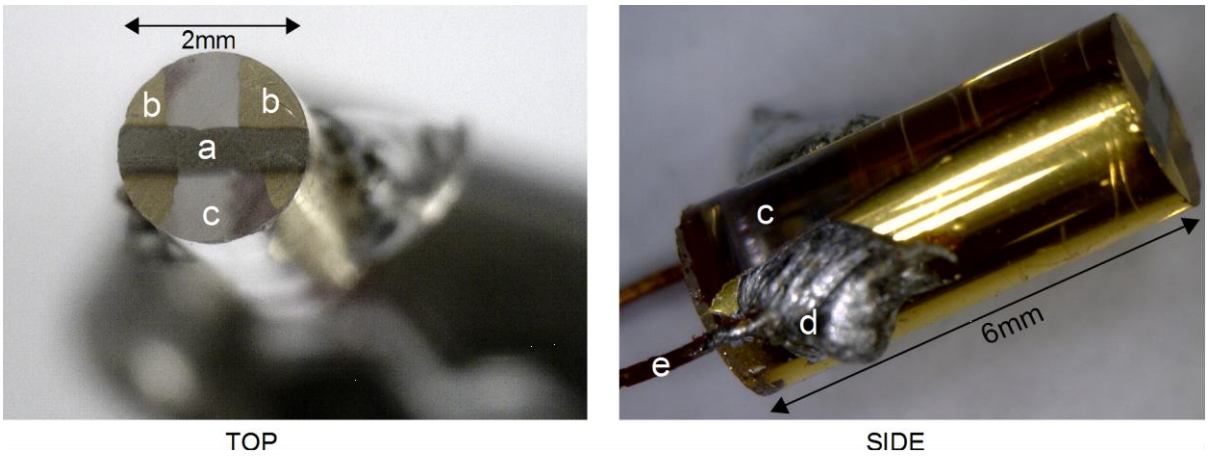

Figure 6-1: Microscopic photograph of the thin film gauges prior to calibration and mounting in the experimental model

Once the nickel strip has been applied, a set of substrates is placed in a separate mount where their entire surface is exposed. Once in this configuration, the substrates are again placed in the Auto 500 Sputtering System and sputtered with a 5kÅ layer of SiO_2 (silica) using RF sputtering – a method by which an electromagnetic field is used to force SiO_2 molecules from the target onto the substrates. While RF sputtering is significantly more time-consuming than the DC ionisation used to sputter nickel, it is necessary when non-conducting materials are to be ionised. Silica is a strong electrical insulator that will shield the gauge from interference by ionised particles in the flow field, as well as affording the sensitive nickel layer a degree of physical protection. The degree to which this insulating layer affects the fidelity of the gauge response was expected to be minimal. Experimental results confirmed this hypothesis as heat readings stabilised well within the timeframe of the test period[26].

6.1.1.2 Calibration

Calibration of the thin film gauges was performed in accordance with standard procedures established at the Centre for Hypersonics, using a calibration oven controlled by a LabView 9 script [20]. The constructed gauges are mounted inside the oven, and run through a predefined temperature profile, with the resistance at each temperature plateau recorded against the actual temperature. The temperature profile used to calibrate the gauges is shown below in Figure 6-2.

[26] As can be seen in Figure 6-8 there is no observed decay or asymptotic behavior during the test time which could indicate a significant effect of the silica layer on heat measurement responsiveness.

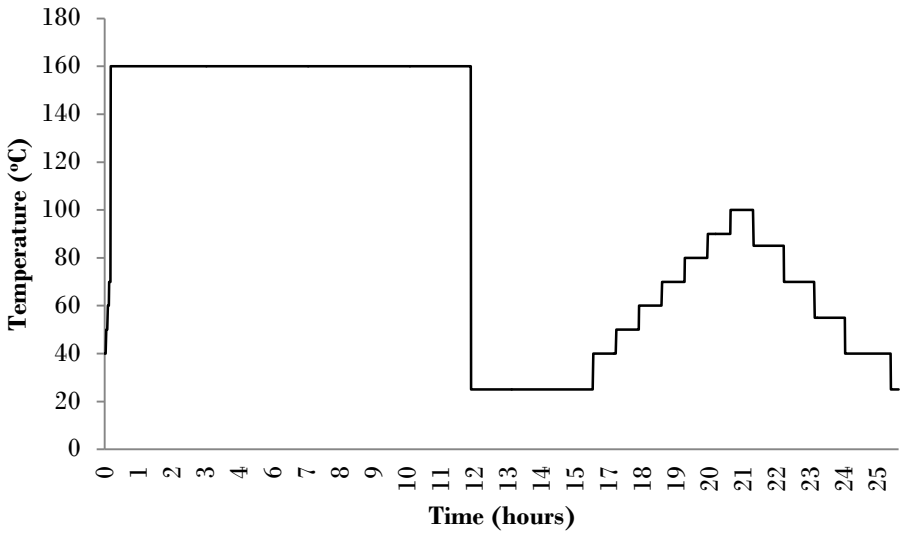

Figure 6-2: Input temperature profile used to calibrate the thin film gauges

The initial heating phase (lasting approximately 11 hours) is designed to anneal the surface of the thermoelectric element and ensure that temperature response will not drift. The necessity of this step is illustrated in a typical plot of gauge response over the calibration profile, shown in Figure 6-3. The response of the gauge can be seen to drift quite drastically during the first 20 minutes, followed by a period of linear decay in voltage response and slight stabilisation after 12 hours near the end of the annealing step.

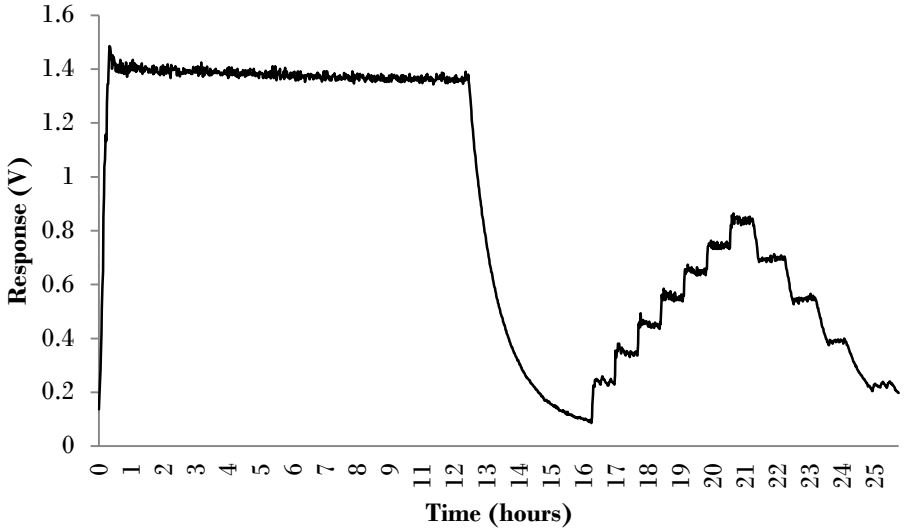

Figure 6-3: Typical calibration response of a gauge, used to establish a relationship between resistance and surface temperature (and ultimately heat flux)

Due to the insulation in the oven, the gradient of downward slopes is softer than for increases in oven temperature. This is taken into account during calibration, and temperatures are only

logged for responses on the temperature plateaus, where the temperature can be safely assumed to be the same for both the oven thermocouple and the gauge.

Once the response is logged for each temperature plateau, the value is adjusted for the lead resistance and amplifier attenuation to yield a resistance value, which is then correlated to the temperature to obtain a sensitivity reading (Ω/K). This sensitivity is in turn compared to the actual temperature responses of the gauge. Gauges with a sensitivity correlation of above 0.995 were considered usable, while gauges with a lower correlation were either discarded or recalibrated (depending on the severity of the discrepancy).

6.1.1.3 Reliability and Quality control

The primary tool for measuring the degradation of the gauges is via observation of the starting resistance, i.e. the resistance of the gauge under room temperature. This resistance should remain sufficiently close to the resistance under which the gauge was calibrated. It was decided to accept variations in resistance of up to 5% before a gauge would be considered invalid. During the test campaign, an effort was made to quickly replace gauges that appeared to experience significant changes in resistance as soon as possible. This was usually done, but due to time restrictions and limitations in accessibility to the gauge recess (especially at higher sweep angles, where the wing covered the recess from behind the recess plate) this was not always possible.

It was found that all gauges usually remained well within the 5% limit in resistance variation, and when they did fail, the change was extremely prominent. This behaviour was expected as the gauges are coated with several hundred nanometres of silicon dioxide, such that any force which would rupture or abrade this protective layer would almost certainly destroy the relatively small layer of conductive nickel underneath it.

Of the 31 gauge recesses on the flat plate of the model, 20 began all shots fully functional, without any detectable error in their resistance or response. Their change in resistance over time is plotted in Figure 6-4 (with the benchmark resistance for each recess reset when a gauge is replaced). It should be noted that the strong correlation is present throughout all of the gauges, including those that failed, and is almost certainly due to changes in either atmospheric conditions during the campaign (which were performed at various times of the day / night) and changes in the vacuum conditions of the dump tank prior to each shot.

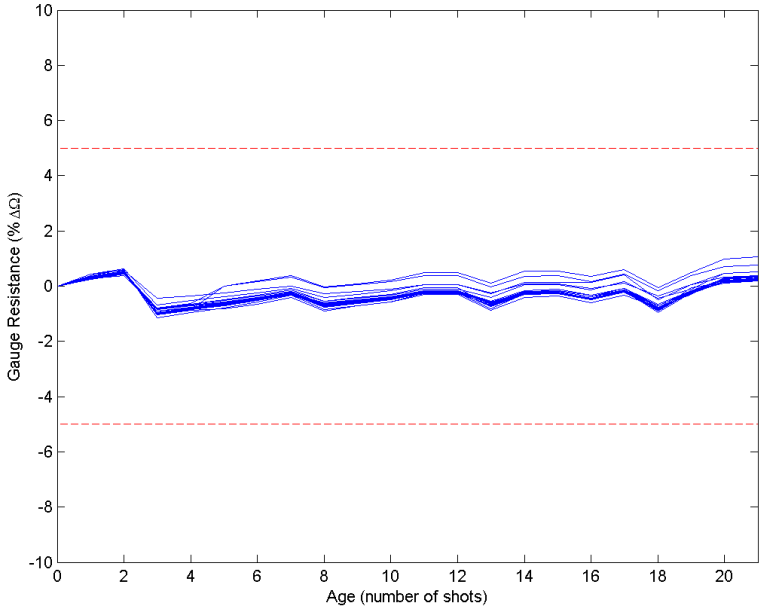

Figure 6-4: Resistance variation from calibrated resistance for all gauge recesses except for 1,5,10,12,14,15,17,19,22,28 and 31 (which contained failed gauges for at least one shot). Red dashed lines represent the 5% error tolerance.

Gauge failure was extremely prominent and always occurred over a single shot, with an order of magnitude change in resistance. This was the only form of failure observed among the gauges, making its detection extremely simple and objective. While the error tolerances were initially decided upon to provide an object tolerance level for drift in resistance, they were never actually relied upon as the failure was so apparent. Figure 6-5 shows the resistance profile of gauge recess 5, which experienced a typical failure and was subsequently repaired (by replacing the gauge).

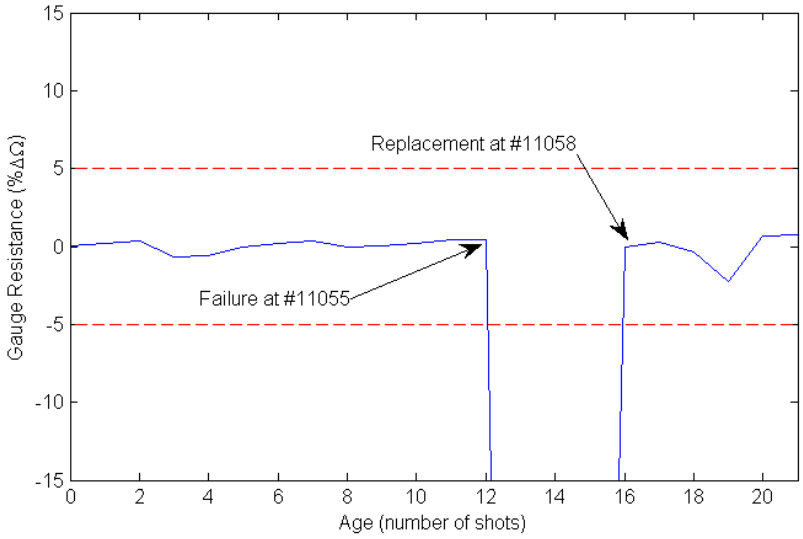

Figure 6-5: Plot of gauge resistance profile of gauge recess 5, exhibiting gauge failure during shot 11054 (detected at resistance check of shot 11055) and repaired profile following gauge

replacement prior to shot 11058 (note that the resistance change is reset to 0% for the new gauge). Red dashed lines represent the 5% error tolerance.

All gauges present on the wing (represented by recesses 50 to 75 in Figure 3-9) experienced open circuit resistances within the first shot, with the vast majority unresponsive before test time was reached. It was decided not to replace the heat transfer gauges on the wing, and instead rely solely on the thermocouple measurements for wing heat flux.

6.1.2 Thermocouples

This section outlines the construction, calibration and quality control measures for the thermocouple sensors used in the present study. For a discussion on the motivation for using thermocouples and the mechanism by which they operate, refer to Section 3.3.2.

6.1.2.1 Construction

In order to obtain heat flux values from the thermocouple voltage, the material properties of the electrode metals and of the mounting materials of the thermocouple itself must be known in order to convert the voltage into a surface temperature and then to obtain heat flux respectively.

Coaxial, E-type thermocouples were chosen for the experiment, due mainly to the relatively similar thermal properties of the materials used. This similarity in material properties reduces the error induced by the assumption of constant thermal properties in the semi-infinite reverse conductivity model used to deduce heat flux from surface temperature[27]. E-type thermocouples are composed chromel and constantan, for the negative and positive electrodes respectively. The sourced thermocouple materials were tested to confirm that the materials yielded the expected response of 63 μV/°C (Schultz & Jones, 1973).

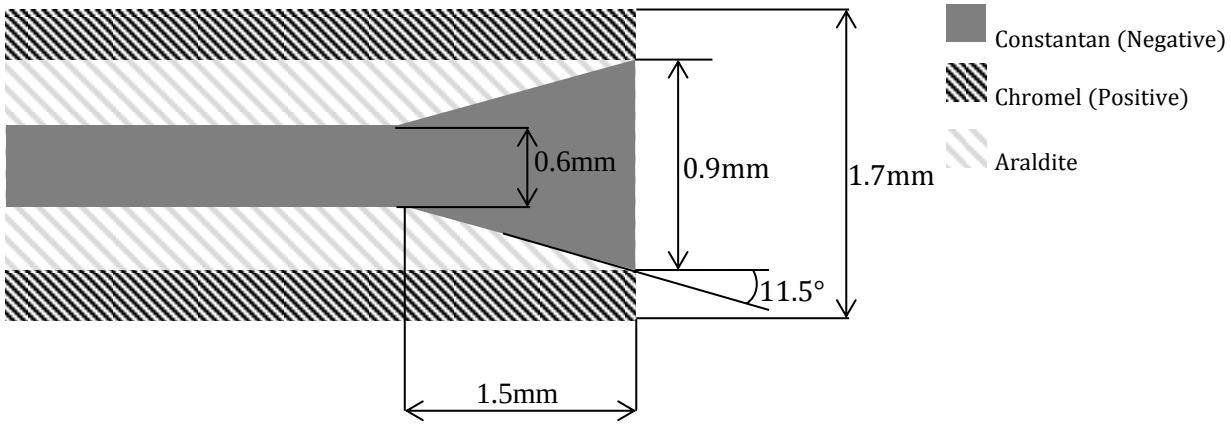

Figure 6-6: Material makeup of the thermocouple sensoring tip and average dimensions provided by Brian Loughrey (the technician responsible for construction of the gauges).

[27] See equation 3.1 for the numerical implementation of the semi-infinite heating solution.

6.1.2.2 Calibration

For the construction of the thermocouples, 14-gauge constantan and 8-gauge chromel were sourced from Industrial Thermocouple Supplies Pty Ltd. To confirm purity of the sourced materials, the 2m lengths of cable were spot-welded together at the tip, and calibrated using a FLUKE 753 Multimeter with E-type calibration settings. A FLUKE 9142 Field Metrology Well was used as the hot well. Results of the calibration are shown in Table 6.1.

Ambient Temp. (°C)	Hot Well (°C)	Response (μV)	Response (μV/°C)
25.4	40	775	53.08
26.2	60	1953	57.78
26.8	80	3060	57.52
26.6	100	4265	58.11

Table 6.1: Constantan-Chromel calibration results

Note that the accuracy of this test was subject to a variety of potential sources of error, such as effects of the welding material used to join the materials, body temperature of the operators handling the cable, and potential inaccuracies in the well and measured ambient temperatures. For this reason the above results were used only used to confirm that the materials were close to the standard properties for E-type thermocouples of 63 μV/°C [21], which were subsequently used.

6.1.2.3 Reliability, quality control and exclusion of data

Unlike the signal from thin film gauges, which is obtained by measuring resistance of the circuit, thermocouples produce their own voltage. A PTA-110 amplifier [22] was used to amplify the thermocouple signal to a range suitable for the T4 Data Acquisition system. Initial thoughts were simply to amplify the signal such that the maximum expected temperature gradient would not exceed the voltage limit for the T4 DAS. This resulted in a PTA-100 amplification setting of 2000 for shots 11043 to 11049. While the severe signal to noise ratio observed in the thermocouples was immediately apparent (see Figure 6-7 below), the cause of the severe distortions was not discovered to be the large amplifier gain until after shot 11049 had been conducted.

The high amplification appeared to intensify distortions disproportionate to the amplifier gain. This was hypothesised to be the result of signal aliasing caused by oscillations in noise exceeding the Nyquist frequency of the data samples. This was not confirmed.

Once the gain was reduced to 500, the signal-to-noise ratio improved drastically and in disproportion to the change in amplifier gain. The improved signal quality is illustrated in Figure 6-8 below.

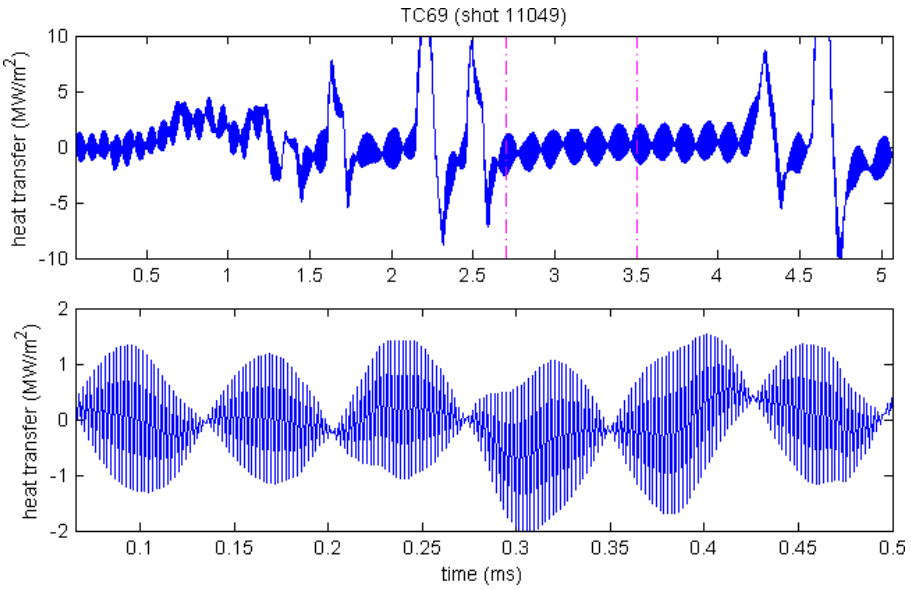

Figure 6-7: Heat transfer response for the thermocouple gauge at recess 69 for shot 11049, where a gain of 2000 was used for the PTA-110 amplifiers. Plot shows the first 5ms of shot data (top) and the first 500µs just prior to arrival of the shock (where response is expected to be to be close to nil)

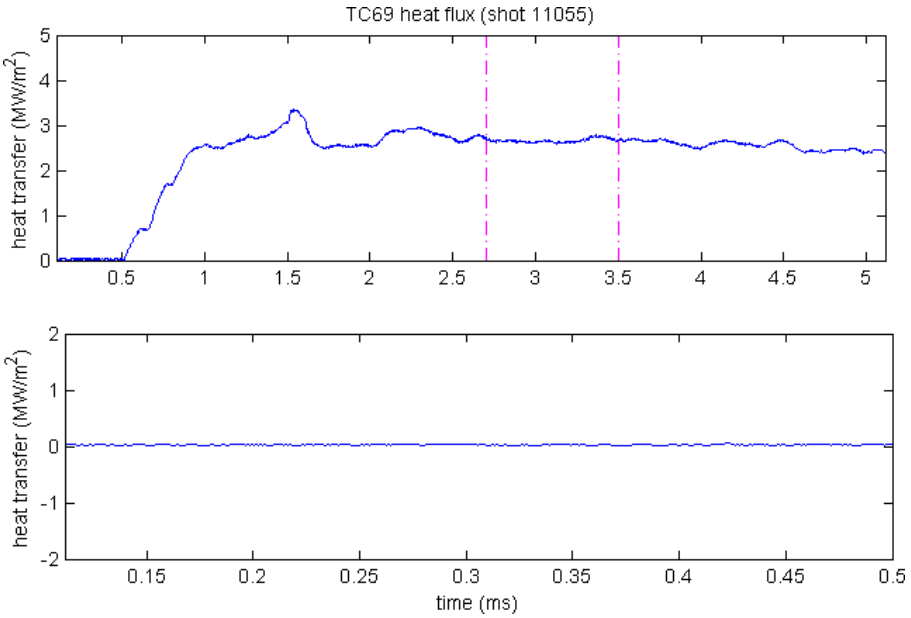

Figure 6-8: Measured heat transfer response for the thermocouple gauge at recess 69 for shot 11055, where gain was reduced to 500 for the PTA-110 amplifiers, after severe signal aliasing observed in prior shots. Plot shows the first 5ms of shot data (top) and the first 500µs just prior to arrival of the shock (where response is expected to be to be close to nil)

Aside from the severe aliasing observed in shots 11049-11055, thermocouple initially appeared good. Many of the gauges experienced reparable failure during the latter period of some of the shots, most likely due to impact with debris or larger oxide fragments that are forced into the

test section. This often resulted in an open circuit response from the thermocouples after some of the shots, despite a complete and reliable reading during test time. The gauges were repaired prior to each shot by lightly rubbing them with 1200 grit 3M Wet and Dry, thereby causing the outer surface of the constantan and chromel electrodes to reconnect (see Figure 6-6).

Gauge failure was occasionally observed during the test time, and in this case the gauge response was marked as invalid and excluded from data analysis.

Despite the apparently stable signal of the gauges subsequent to a reduction in the amplification gain, the heat transfer rates could not be reconciled against the theoretical heat transfer measurements as predicted by the Beckwith equations discussed in Section 2.4.

The thin film gauges on the wing were almost entirely destroyed within the test time of the first shot, and it was subsequently decided not to replace them and instead rely on the thermocouple readings for wing heat flux measurements. As such there is no heat transfer data with confirmable results on the wing.

A summary of the heat flux measurements is provided in Figure 6-9 and Figure 6-10 for low and high pressure conditions respectively, with heat flux of gauges at recesses 64-69 (see Section 6.1.3 for reference) plotted against distance from the centre point of each recess to the wing root (the intersection between the inclined wing and flat plate leading edge in Figure 6-22). Error bars represent the standard deviation of the signal over the test time.

It is worth noting that thermocouples at recesses 64 and 65 (see Section 6.1.3 for reference) failed just prior to arrival of the test time for shots at 55° of sweep for the low pressure conditions (shots 11050, 10051 and 11052). For this reason, recess 65 is missing from the 55° sweep angle results from Figure 6-9.

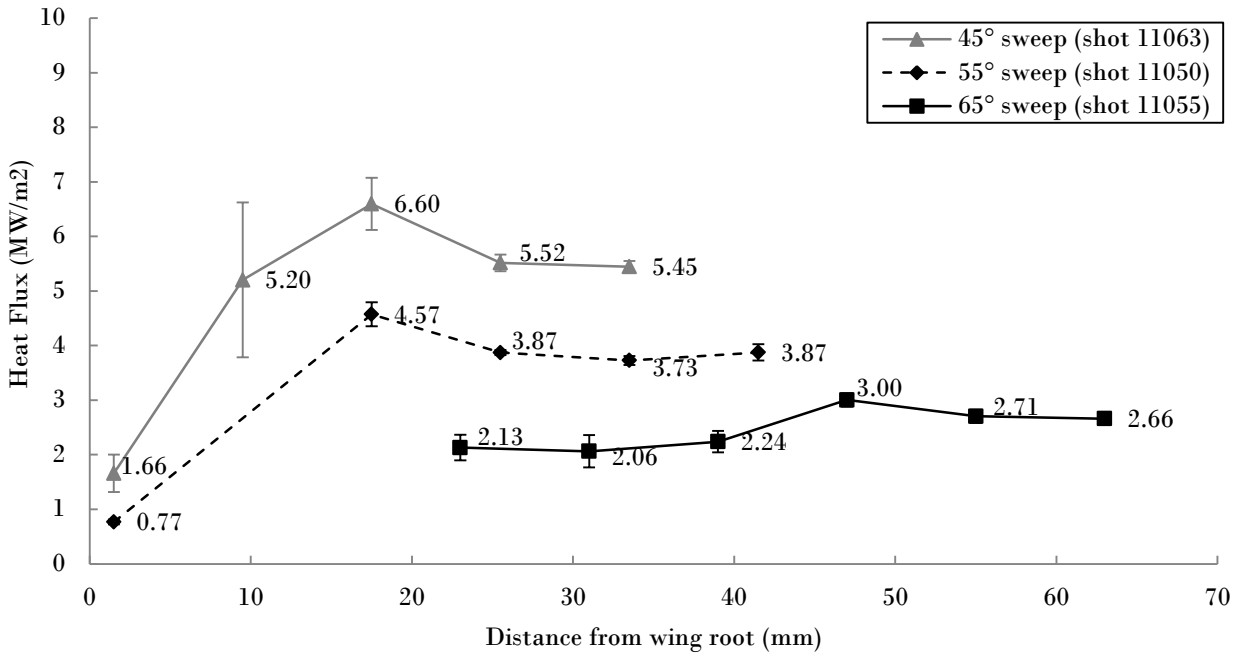

Figure 6-9: Heat flux along the wing plotted against distance to the wing root for low pressure shots at 45°, 55° and 65° sweep angles, with standard deviation error bars.

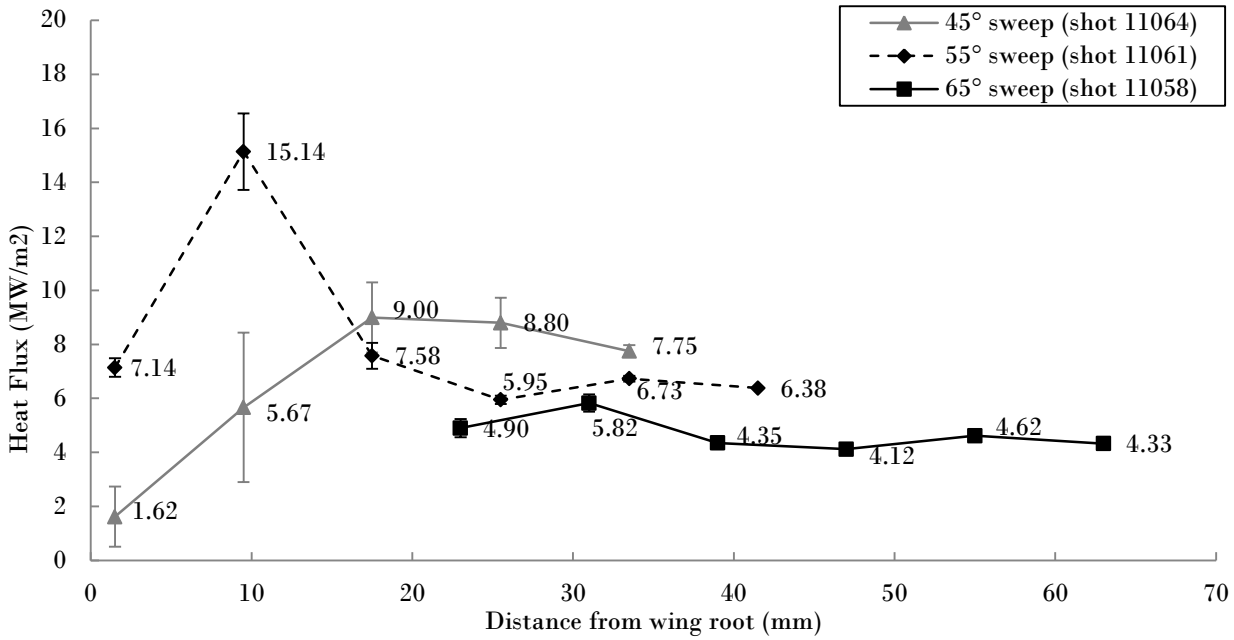

Figure 6-10: Heat flux along the wing plotted against distance to the wing root for high pressure shots at 45°, 55° and 65° sweep angles, with standard deviation error bars.

There are several observations which can be made about these results, which hold across both the low and high pressure shots (Figure 6-9 and Figure 6-10 respectively):

1. There is a distinct peak in heat flux occurring at a distance from the wing increasing with higher sweep angles and decreasing for higher pressure shots.
2. The standard deviation of the measured heat flux is significantly higher for regions near or before the heat flux peak.
3. Heat flux stabilizes as distance from the wing-root increases, at a level inversely correlated to sweep angle.

Despite the higher than expected heat transfer readings, the profile of the heat transfer over the wing is broadly consistent both with theory and the results observed for the heat flux measurements on the flat plate, where the horseshoe heat flux profile confirms the formation of a recirculation region ahead of the wing root. Such a recirculation region, occurring in the vicinity of the intersection of the inclined with and the flat plate leading edge (as illustrated in Figure 6-22), would be expected to generate peak heat flux at a region above the recirculation zone, where the largest velocity gradient occurs. As such, the location of the heat flux peak is an indication of the size of the recirculation zone. That the size of this region can therefore be inferred to increase with increasing sweep angle is also consistent with theory.

Using to the Beckwith application of the Van Driest turbulent solution to swept cylinders[28], the heat transfer at the limit of high distance from the flat plate using the flow conditions derived by NENZFr simulations (Table 6.6) are shown in Table 6.2 below for each shot represented in Figure 6-9 and Figure 6-10.

[28] For the Beckwith adaption of the Van Driest solution to turbulent flow see equation 2.10

Shot number	Condition (see Table 4.1)	Sweep Angle	Beckwith turbulent stagnation heat transfer ($MW.m^{-2}$)	Experimental stagnation heat transfer ($MW.m^{-2}$)
11050	Low Pressure	55°	1.28	3.87
11055	Low Pressure	65°	0.37	2.66
11058	High Pressure	65°	1.11	4.33
11061	High Pressure	55°	3.07	6.38
11063	Low Pressure	45°	2.67	5.45
11064	High Pressure	45°	5.94	7.75

Table 6.2: Heat transfer approximations based on the Beckwith solution to turbulent heat transfer of a swept cylinder [15] for test conditions considered representative for wing heat transfer measurement plotted against heat transfer observed far from the wing root.

While the substantially higher enthalpies of the experimental conditions relative to the US Standard atmosphere at 30km substantially increased the expected thermocouple readings, the results are still as much as 4x what would be expected from theory.

As discussed in Appendix Section 6.1.2.3 , the first 7 shots of the test campaign (shots 11043-11049) exhibited severe signal noise in the thermocouple data (the thermocouples were connected to the PTA-110 amplifiers which produced the noisy signal). As this issue appeared to persist for all of the installed thermocouples, and as all thermocouples and associated wiring appeared to be correctly installed and insulated, it was decided to reduce the signal gain from x2000 to x500 on the amplifiers, which caused the signal to noise ratio to rise. The effect of this is clearly illustrated in the Appendix (6.1.2.3).

While noise seemed to be resolved for shots after 11049, the error in thermocouple data obviously persisted, and could have been caused by;

1. a fault in the PTA-110 amplifiers,
2. amplifier pins corresponding to amplifier settings being incorrectly set, or
3. a wiring, grounding or other unidentified electrical issue, or
4. Incorrectly recorded data, with some unaccounted gain which has yet not been identified.

As 2 separate amplifiers were used to transmit the signal from the 6 thermocouples, it appears unlikely that a fault in the amplifiers would cause such a seemingly consistent error. Causes 2 and 3 appear the most likely, although both are impossible to track retrospectively. It can be said though that the heat flux observed for shots prior to 11049, when the signal was heavily aliased at amplification settings of x2000, the average heat flux still appeared to be broadly in line with the results measured for similar shots. For example, for shots 11045 and 11063 (both low pressure shots at 45° sweep) the heat flux at the downstream thermocouple ranged from 4.5 to 5.9 $MW.m^{-2}$, broadly in line with the 5.45 $MW.m^{-2}$ and approximately twofold the result expected from the semi-empirical Beckwith equations shown in Table 6.2.

It is most likely that an electrical issue was the cause, likely within the model where human error is more likely. An insulation or grounding issue causing a persistent voltage to retard the

voltage readings could explain the error. In either case, while the nominal values of the readings are evidently incorrect, there is nothing to suggest that the heat transfer profile (specifically the peak heat flux locations) itself is not reliable.

6.1.3 Wing and Flat Plate Recess Numbering and Gauge Mounting

In reference to Figure 6-11 and Figure 6-12 below:

- Recesses 1-31 were occupied by thin gauges named HT1-HT31 respectively (although recesses 10,15 and 19 could not be occupied at high sweep angles as the wing angle covered the recesses from the inside of the model).
- Recesses 50-63 on the wing were initially occupied by thin film gauges HT50-HT63, but as most were destroyed during the first shot, it was decided not to utilise these recesses for further measurements.
- Recesses 64-69 were occupied by thermocouple gauges TC64-TC69 respectively.
- Recesses 70-75 remained empty for the duration of the campaign due to limited availability of thermocouple gauges.

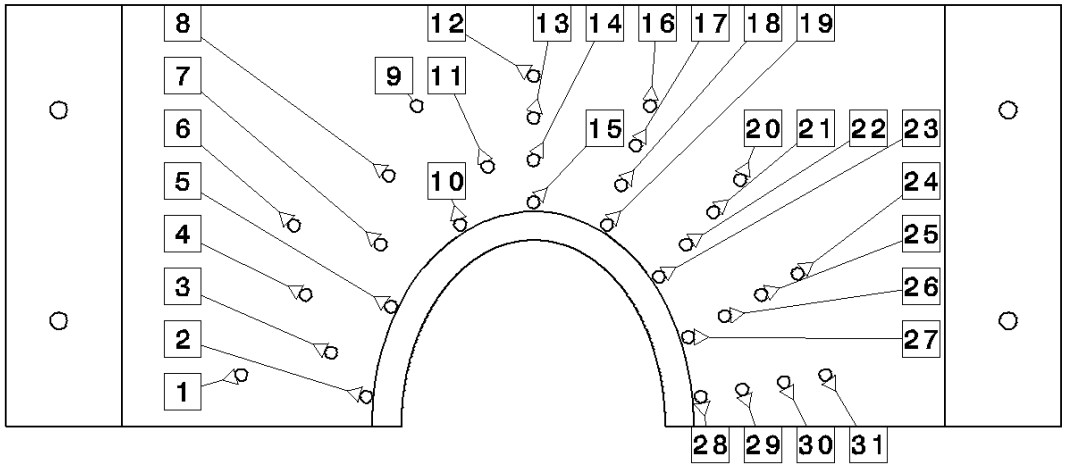

Figure 6-11: Flate plate insert recess numbering (top to bottom is the direction of flow, left to right is port to starboard)

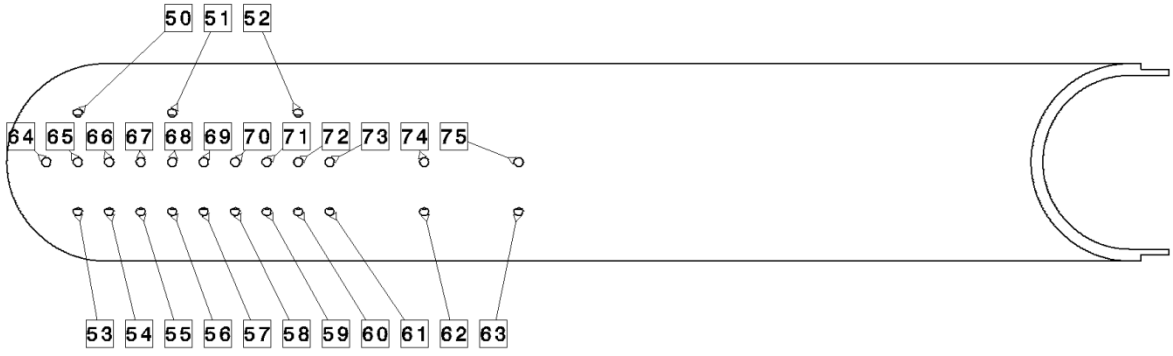

Figure 6-12: Wing hole recess numbering (left to right is direction of flow and from the base of the model extending away, and top to bottom represents port to starboard).

6.2 Experimental Campaign

6.2.1 Conditions

Two primary test conditions, hereafter called the *Low pressure* and *High pressure* conditions were used in the campaign, with the pressures and gases used to operate the T4 test facility shown below in Table 6.3.

	Low Pressure condition	High Pressure condition
Test gas (shock tube)	100 % Air @ 130kPa	100 % Air @ 260kPa
Driver gas (compression tube)	100 % Argon @ 40.2ka	100 % Argon @ 80.5 kPa
Diaphragm	3mm mild steel	6mm mild steel
Reservoir	2.5 MPa	5.8 MPa

Table 6.3: High and low pressure fill conditions used.

The low pressure condition was chosen because the flow resulting from this condition was expected to represent the atmospheric conditions at 30km altitude most closely, given the available sets of conditions for which the tunnel has been certified to operate. The high pressure condition was chosen simply to represent conditions of comparatively higher heat flux, and would be used to assess whether or not the resulting measurements responded as expected.

6.2.2 Shot Summary

During the initial 10 shots of the campaign, a series of low pressure shots was conducted at sweep angles of 45° and 55°. The stability of the resulting voltage traces and schlieren photography indicated that the flow was not turbulent at these conditions. A small trip was constructed to ensure that the boundary layer would transition to turbulence, and the high pressure condition was introduced for the later shots, which included both high and low pressure conditions at 45°, 55° and 65° of sweep. The resulting conditions for each of the 22 shots are shown in Table 6.4.

Shot number	Resevoir (Mpa)	Driver gas (kPa)	Test gas (kPa)	Sweep	Trip
11043	2.5	40.2	130	45	no
11044	2.6	40.2	130	45	no
11045	2.6	40.2	130	45	no
11046	2.6	40.2	130	45	no
11047	2.6	40.2	130	45	no
11048	2.6	40.2	130	55	no
11049	2.6	40.2	130	55	no
11050	2.6	40.2	130	55	no
11051	2.6	40.2	130	55	no
11052	2.6	40.2	130	55	no
11053	5.6	80.5	264	55	no
11054	5.8	80.5	260	55	no
11055	2.6	40.2	130	65	no
11056	5.8	80.5	260	65	no
11057	2.6	40.2	130	65	yes
11058	5.8	80.5	260	65	yes
11059	5.8	80.5	260	65	yes
11060	2.6	40.2	130	65	yes
11061	5.8	80.5	260	55	yes
11062	2.6	40.2	130	55	yes
11063	2.6	40.2	130	45	yes
11064	5.8	80.5	260	45	yes

Table 6.4: Conditions for each of the 22 shots conducted. The blue shaded rows represent low pressure conditions, and the red shaded rows represent high pressure conditions. Shots 11043 and 11053 were the first of the condition, and slight changes were made in subsequent shots to ensure stable conditions during the test times.

6.2.3 Exclusion of shots

6.2.3.1 Incorrect fill conditions

As the first shot of the campaign occurred immediately after a major repair of the piston launcher, it was decided to revert back to the rated, nominal pressure settings for each new condition. Operators of prior campaigns used higher than nominal pressure in order to achieve desired conditions, and in order to avoid potentially damaging the tunnel, nominal conditions were used initially. Shots 11043 and 11053 represented the first shots at the “low” and “high”

pressure conditions (for a description of the conditions, see Table 6.3). Both shots resulted in undesirable conditions, with the diaphragm failing to open completely for shot 11043 and an under-tailored stagnation pressure profile for shot 11053. As a result, these shots were not considered in the results.

6.2.3.2 Duplications

Additionally, where multiple shots of the same condition were performed, only one was selected (based on the conditions, number of surviving thin film gauges and reliability of thermocouple data). This resulted in the further exclusion of shots 11045, 11046, 11047, 11048, 11050, 11051, 11052, 11058, 11060. Due to the persistent failure of a thermocouple in several shots, shots 11050 and 11058 were included to represent the low pressure 55° and high pressure 65° conditions for the wing heat flux results respectively. The resulting array of shots utilised for the study are shown in Table 6.5.

Shot number	Resevoir (Mpa)	Driver gas (kPa)	Test gas (kPa)	Sweep	Trip
11044	2.6	40.2	130	45	no
11049	2.6	40.2	130	55	no
11050	2.6	40.2	130	55	no
11055	2.6	40.2	130	65	no
11056	5.8	80.5	260	65	no
11057	2.6	40.2	130	65	yes
11058	5.8	80.5	260	65	yes
11059	5.8	80.5	260	65	yes
11061	5.8	80.5	260	55	yes
11062	2.6	40.2	130	55	yes
11063	2.6	40.2	130	45	yes
11064	5.8	80.5	260	45	yes

Table 6.5: Shots selected for study. The blue shaded rows represent low pressure conditions, and the red shaded rows represent high pressure conditions.

6.2.4 Non-equilibrium Flow Simulations

The test campaign was composed of the University of Queensland T4 hypersonics facility shots 11043 - 11064. Test conditions based on non-equilibrium expansion calculations using the University of Queensland's NENZFr code [19] are shown in Table 6.6 below.

Shot number	Density (kg/m^3)	speed (m/s)	Pressure (Pa)	Sound speed (m/s)	Dynamic Viscosity (Pa.s)	Kinematic Viscosity (m^2/s)	Temperature (K)	Mach No.	Total Pressure (MPa)	Total Enthalpy (MJ/kg)
11044	0.026378	2469.1	2106.9	334.25	1.74E-05	0.02462	277.1	7.39	12.41	3.10
11045	0.02594	2546.9	2222.3	346.12	1.84E-05	0.02606	297.16	7.36	12.81	3.33
11046	0.02635	2559.1	2283.7	348.11	1.85E-05	0.026303	300.62	7.35	13.10	3.37
11047	0.025173	2549.5	2161.4	346.5	1.84E-05	0.026107	297.83	7.36	12.50	3.34
11048	0.026474	2530.7	2228.2	343.08	1.81E-05	0.025691	291.96	7.38	13.04	3.28
11049	0.026323	2541.1	2238.6	344.85	1.83E-05	0.025906	294.99	7.37	13.01	3.31
11050	0.026112	2550.7	2241.7	346.48	1.84E-05	0.026104	297.79	7.36	13.00	3.34
11051	0.025978	2573.1	2283.5	350.57	1.87E-05	0.026603	304.89	7.34	13.00	3.42
11052	0.026199	2545.4	2238.1	345.63	1.83E-05	0.026	296.32	7.36	13.00	3.33
11054	0.045024	2767.3	4880.7	388.89	2.19E-05	0.031349	375.96	7.12	23.20	4.07
11055	0.024957	2515.3	2067.5	340.38	1.79E-05	0.025363	287.37	7.39	12.22	3.24
11056	0.043801	2738.8	4881.5	394.22	2.24E-05	0.032024	386.53	6.95	20.01	3.98
11057	0.025614	2516.8	2128.2	340.88	1.79E-05	0.025423	288.21	7.38	12.52	3.24
11058	0.045123	2795.7	5013.2	393.62	2.24E-05	0.031949	385.3	7.10	23.67	4.13
11059	0.045469	2751.9	4851.7	385.87	2.17E-05	0.030967	370.08	7.13	23.40	4.02
11060	0.02583	2491.9	2091.6	336.54	1.76E-05	0.024898	280.91	7.40	12.50	3.16
11061	0.046058	2762.6	4966.1	387.86	2.19E-05	0.031218	373.96	7.12	23.80	4.06
11062	0.024454	2485.6	1961.5	334.96	1.74E-05	0.024705	278.26	7.42	11.90	3.14
11063	0.025316	2565.1	2205.2	348.99	1.86E-05	0.02641	302.13	7.35	12.60	3.39
11064	0.044503	2750.5	4744.1	385.69	2.17E-05	0.030945	369.72	7.13	22.80	4.01

Table 6.6: Theoretical conditions during test time based on NENZFr non-equilibrium flow simulations [19]. Shots 11043 and 11053 were excluded as conditions were not nominal.

6.2.5 Symmetry of Incoming Flow

To demonstrate the observed asymmetry, the responses of gauge recesses 9 and 16 (which are each at 22.12cm from the symmetry plane, as shown in Figure 6-13) were plotted for the Low pressure, High Pressure, and with / without trip conditions. These recesses were chosen both because of their position and because they contained the same gauges throughout the entire test campaign, without undergoing significant changes in resistance or any other signs of failure. These recesses were also located sufficiently upstream to be outside of the expected bow shock region.

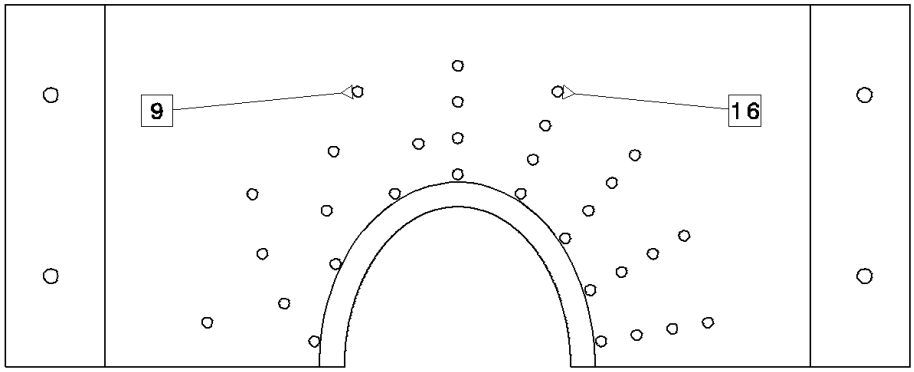

Figure 6-13: Visual representation of the location of gauge recesses 9 and 16, used to assess flow symmetry

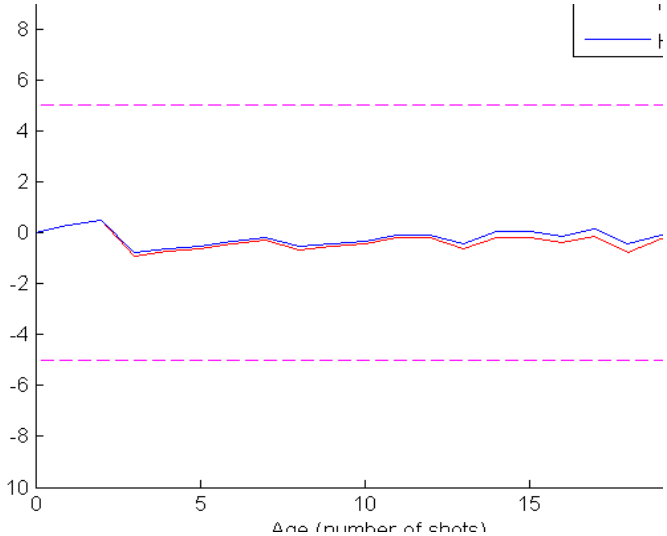

Figure 6-14: Resistance trend for Gauges 9 and 16 (red and blue respectively) plotted against the number of shots the gauge has experienced as well as the 5% tolerance lines (pink dashed lines)

6.2.5.1 Observed asymmetry of flow at upstream gauge locations

Flat plate heat transfer measurements appeared distinctly to increase both with decreasing sweep and with higher flow enthalpies, as can be clearly seen in the visual representations of surface heat flux during the test time in Figure 4-20, Figure 4-21 and Figure 4-22. However, as

noted in Section 4.4, there does appear to be an explanation for the onset of higher heat flux upstream of the wing root, as is particularly evident in Figure 4-22. The cause of this was hypothesised to be the early onset of turbulence due to disturbances to the flow prior to reaching the thin film gauges. This could be caused either by the small, unintentional backward facing step caused by the slightly recessed flat plate insert, as seen in mark *A* in Figure 6-15, or by the additional RTV silicone that had to be used to seal the recessed manufacturing defects present in the flat plate of the model (mark *B* in Figure 6-15).

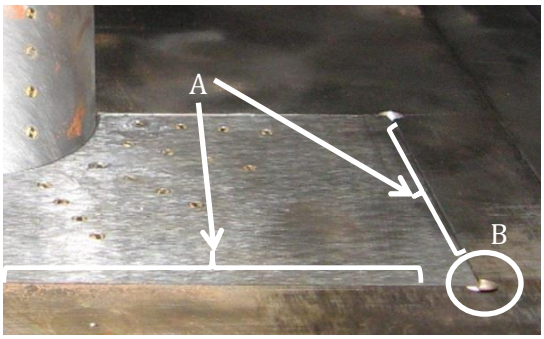

Figure 6-15: Magnified view of the flat plate prior to testing (from Figure 3-6) showing the recess of the flat plate (A) and manufacturing defect present on the four corners of the flat plate insert (B).

To confirm the hypothesis that unintentional surface imperfections were responsible for causing the observed asymmetry in the thin film gauge measurements, the Van Driest laminar and turbulent surface heat transfer rates from Section 2.1 were calculated based on the experimental conditions derived by the NENZFr simulations [19] for the corresponding shot (See Table 6.6). These were then superimposed onto the heat flux readings over the test time for heat transfer gauges 9 and 16 (with reference to Figure 3-8), which correspond to locations on the flat plate where heat flux is distinctly increased for only one side, while still being sufficiently far away from the wing root to not experience the effect of the recirculation region.

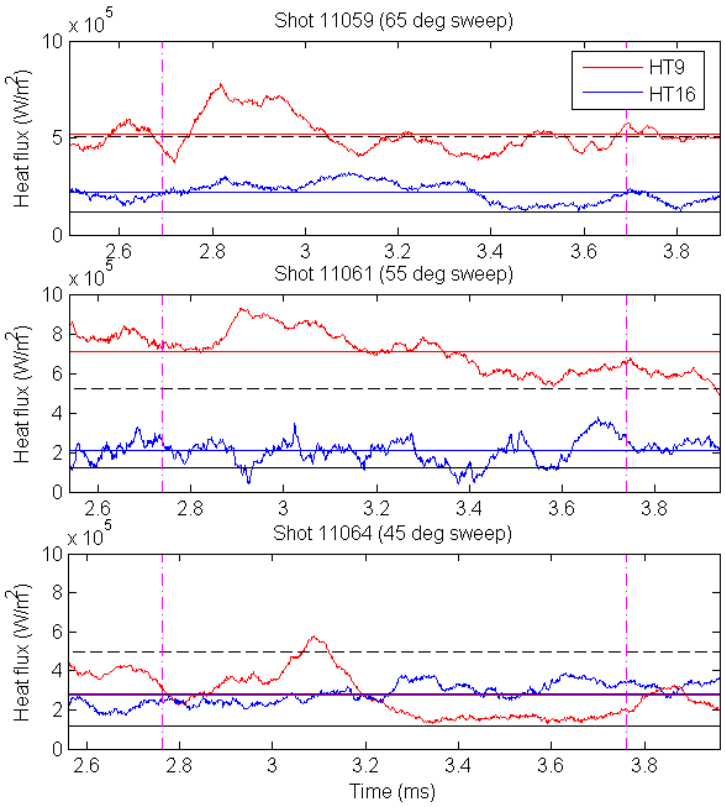

Figure 6-16: Time-accurate heat flux measurements for heat transfer gauge recesses 9 and 16 (red and blue respectively) shown against the test time mean heat flux value (solid lines), Van Driest solutions for laminar and turbulent flow (black solid and dashed lines respectively), and shot test time (pink interrupted lines) for shots high pressure shots with use of a trip.

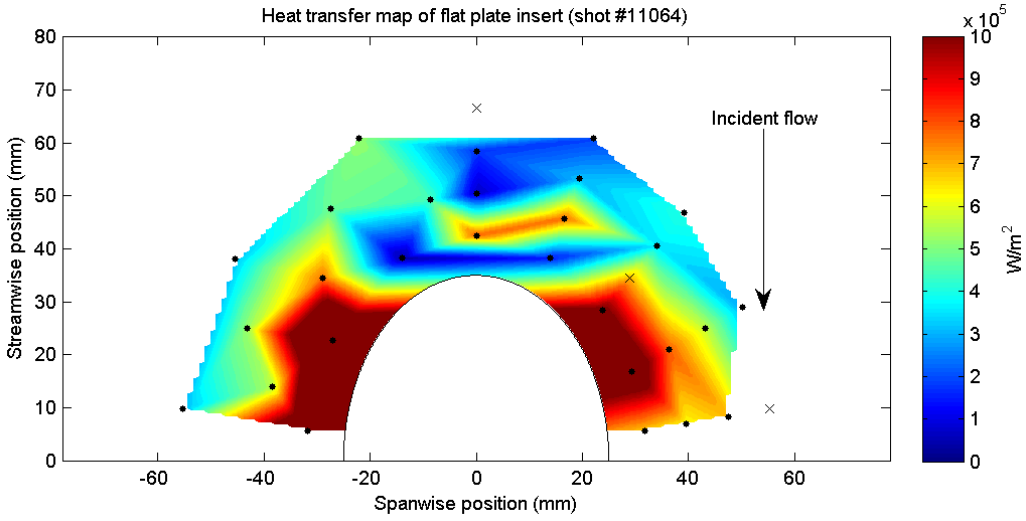

Figure 6-17: Surface contour plot of heat transfer for a 45° sweep, high pressure, tripped condition showing severe asymmetry of the heating rate.

Figure 6-17 demonstrates how flow with a trip appears in terms of the surface heating rate topology. Figure 6-18 shows the same plot but with gauge readings symmetrically superimposed.

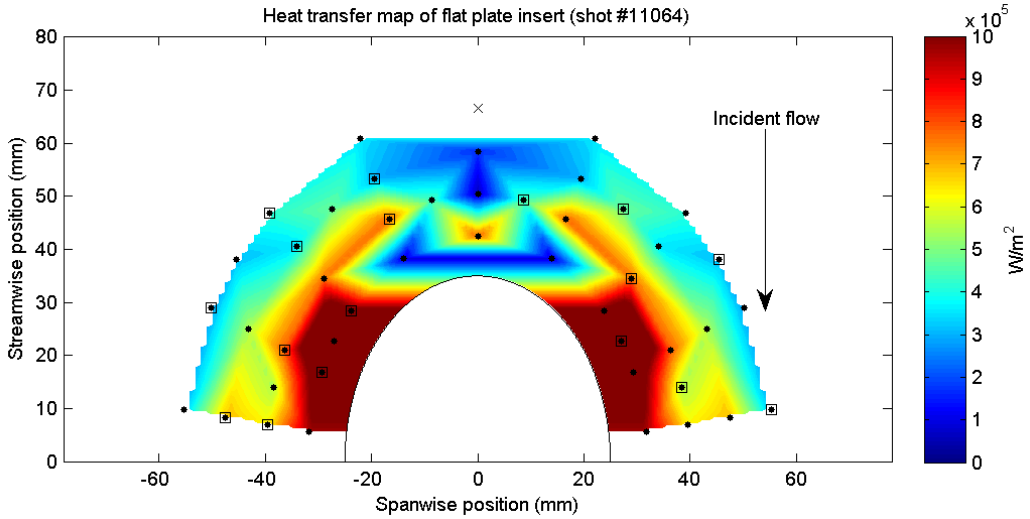

Figure 6-18: Surface contour plot with symmetrical superimposition of gauges for a 45° sweep, high pressure, tripped condition.

While the data is not sufficient to prove that a turbulent boundary layer was in fact present at the location of gauge recess 9 for those shots, it does appear, rather starkly, that for shots where the correlation between gauge recess 9 and 16 is poor the turbulent solution correlates more closely with heat transfer gauge recess 9, and the laminar solution correlates more closely with recess 16. It appears unlikely that such a trend would be observed in a natural turbulence transition on a smooth, symmetric surface, given that gauge recess 9 consistently exhibits a higher heat flux than recess 16 for shots at high pressure conditions or where a trip was employed.

Given that no measurable deterioration in the quality of either gauge was detected during the campaign[29] it was concluded that the asymmetry observed in the results of high pressure shots and shots where a trip was employed was caused by asymmetries on the surface. As the gauges were regularly monitored for obstruction and because gauge 16 does not appear to "lag" behind the response of 9 or exhibit stunted responsiveness (as would be expected if a contaminant covered or obstructed the surface), it was concluded that irregularities on the surface of the model caused incoming flow to transition or at least become perturbed and unrepresentative in those regions.

To further document the observed asymmetry, the responses of gauge recesses 9 and 16 (which are each at 22.12cm from the symmetry plane, as shown in Figure 6-11) were plotted for the

[29] Quality control of gauges is documented in Appendix Section 6.1.1.3

Low pressure, High Pressure, and with / without trip conditions. These recesses were chosen both because of their position and because they contained the same gauges throughout the entire test campaign, without undergoing significant changes in resistance or any other signs of failure. These recesses were also located sufficiently upstream to be outside of the expected bow shock region.

6.2.5.2 Low Pressure without trip (shots 11044, 11049, 11055)

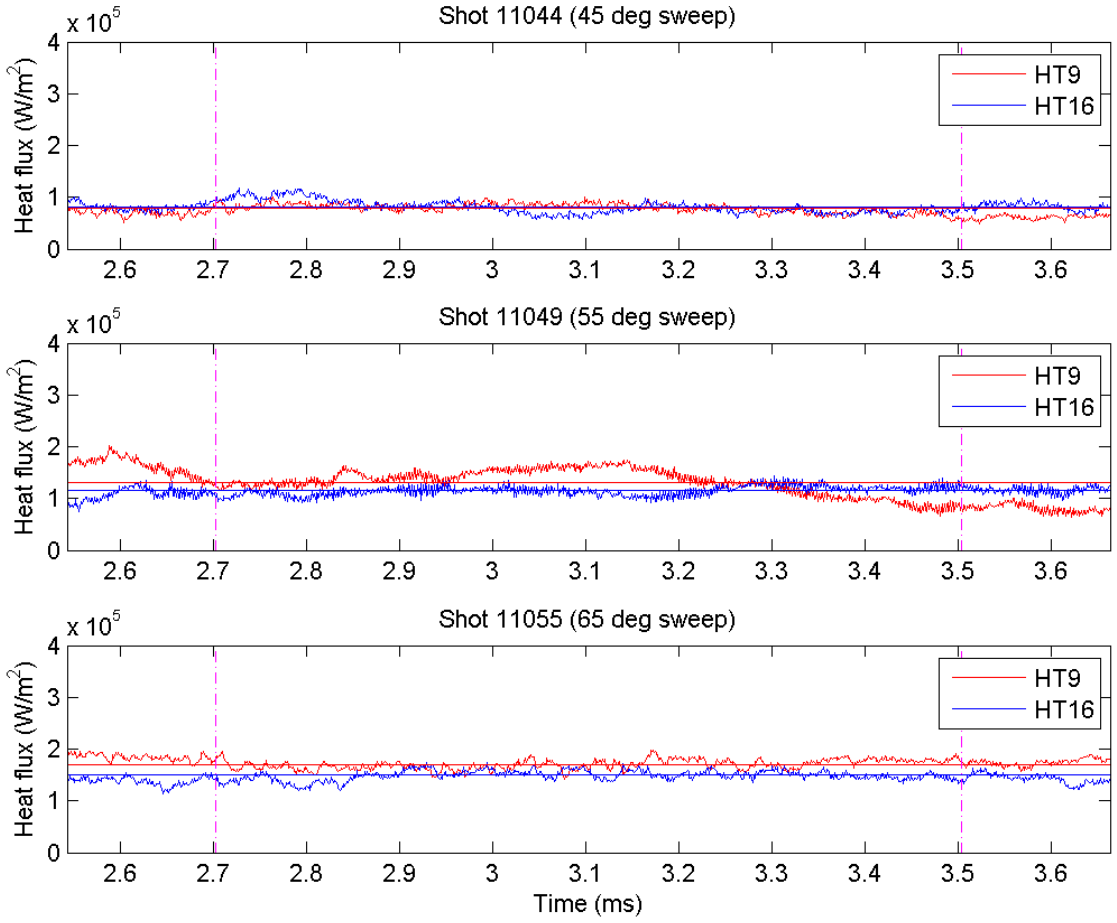

Figure 6-19: Plot of the 9/16 recess pair (red/blue respectively) for low pressure conditions without use of the trip. Mean values are represented by the flat lines and are $0.79 \times 10^5\ W/m^2$ and $0.81 \times 10^5\ W/m^2$ for shot 11044, $1.3 \times 10^5\ W/m^2$ and $1.2 \times 10^5\ W/m^2$ for shot 11049, and $1.7 \times 10^5\ W/m^2$ and $1.5 \times 10^5\ W/m^2$ for shot 11055 for gauges 9 and 16 respectively.

6.2.5.3 High Pressure without trip

Shots 11053, 11054 and 11056 were the only shots conducted at high pressure and without a trip, and all were excluded. Shot 11053 was found to be under-tailored (see Section 6.2.3.1), and shots 11054 and 11056 both experienced unusually high instability, resulting in a lack of confidence in the results.

There are various reasons contributing to instability in a given shot. These are often outside of the experimenter's control and can include anything from human error or oversight on behalf of either the experimenter or operator, minor failures such as o-ring leaks or ruptures, material defects in the diaphragm, wear and tear in tunnel components (most commonly the launcher or piston), and a host of other potential variations inherent in operating such a complex piece of machinery.

Shots 11054 and 11056 were found to be unusually unstable. This may have been related to the rupture of a seal between the nozzle and dump tank which was observed to occur in both instances, although unusually high pressures were not observed in the dump tank prior to firing (suggesting that a significant leak was not the cause).

For this reason, there are no shots at the High Pressure condition with the use of a trip.

6.2.5.4 Low Pressure with trip (shots 11057, 11062, 11063)

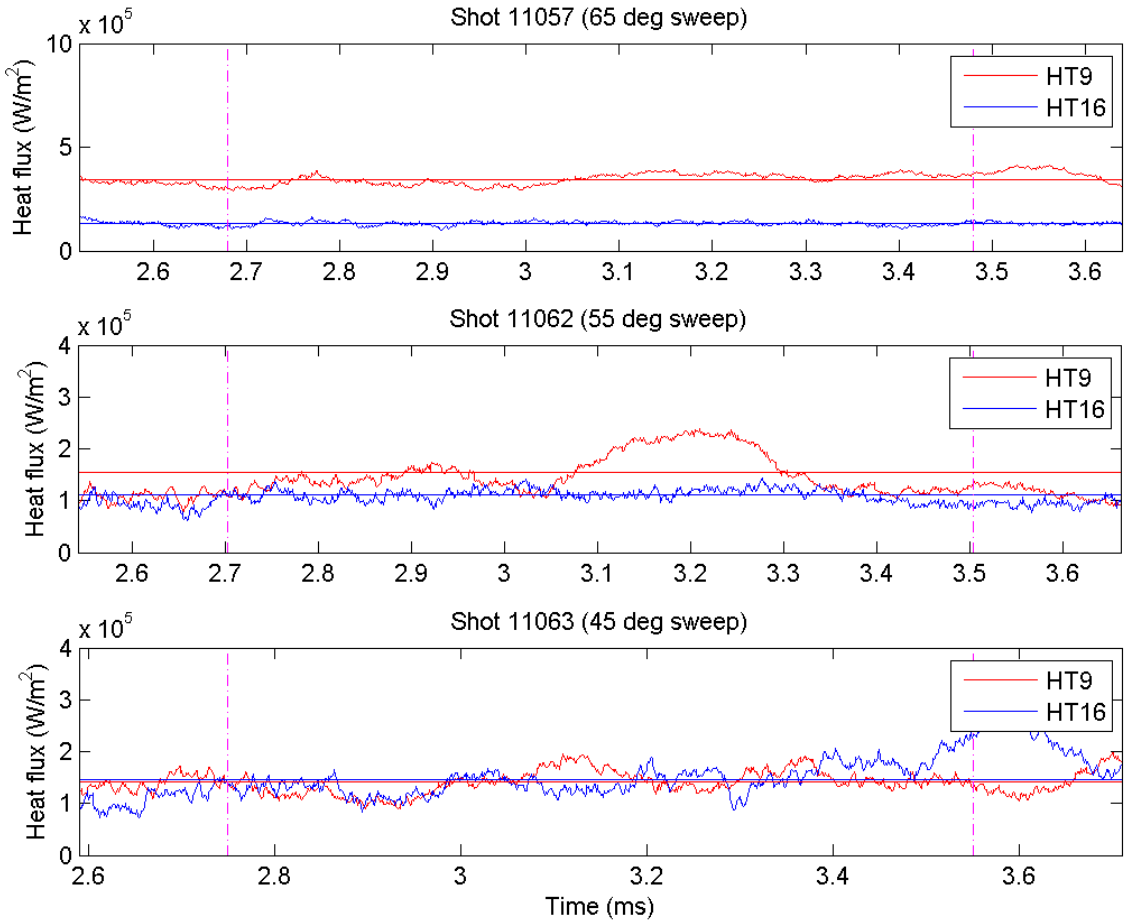

Figure 6-20: Plot of the 9/16 recess pair (red/blue respectively) for low pressure conditions with use of the trip. Mean values are represented by the flat lines and are $3.5 \times 10^5\ W/m^2$ and $1.3 \times 10^5\ W/m^2$ for shot 11057, $1.5 \times 10^5\ W/m^2$ and $1.1 \times 10^5\ W/m^2$ for shot 11062, and $1.4 \times 10^5\ W/m^2$ and $1.5 \times 10^5\ W/m^2$ for shot 11062 for gauges 9 and 16 respectively.

6.2.5.5 High Pressure with trip (shots 11059, 11061, 11064)

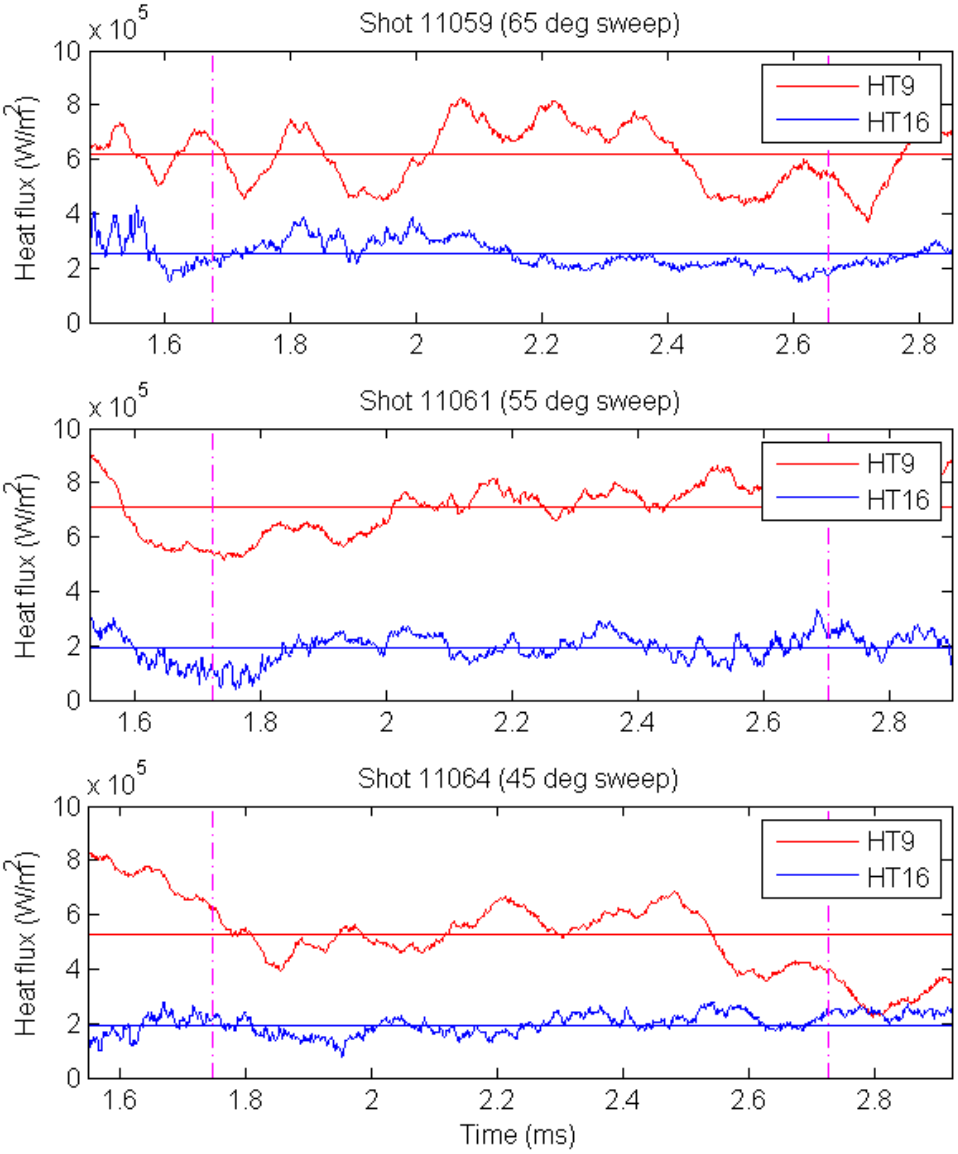

Figure 6-21: Plot of the 9/16 recess pair (red/blue respectively) for high pressure conditions with use of the trip. Mean values are represented by the flat lines and are $6.2 \times 10^5\ W/m^2$ and $2.5 \times 10^5\ W/m^2$ for shot 11059, $7.1 \times 10^5\ W/m^2$ and $2.5 \times 10^5\ W/m^2$ for shot 11061, and $5.2 \times 10^5\ W/m^2$ and $1.9 \times 10^5\ W/m^2$ for shot 11064 for gauges 9 and 16 respectively.

6.3 Theory

Due to the fixed set of shock tunnel test conditions under which the T4 facility is certified to operate, it is not possible to emulate atmospheric flight conditions precisely. This section is intended to provide an overview merely of the analytical tools used to validate and compare experimental results. We will assume ideal atmospheric conditions here for illustrative purposes, and will discuss the application of these equations to actual experimental conditions in Chapter 0.

Figure 6-22 shows a schematic of the experimental model and the upstream edge of the bow shock which forms over the wing.

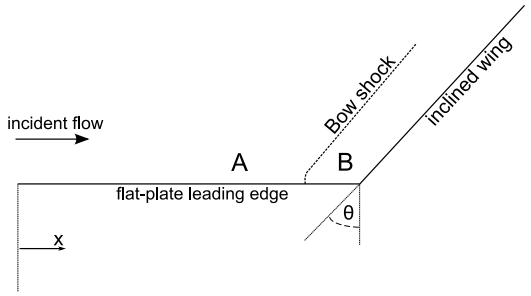

Figure 6-22: Schematic of the wing-root experiment

Region A represents the Mach 8 free stream at 30km altitude. These conditions are based on the 1976 US Standard Atmosphere data [23], and are shown in Table 6.7. The surface heating in this region is characterised by a flat plate boundary layer, and is low relative to that in the interaction region (B) or on the cylinder surface.

Property	**Value**
Density	$0.018\,kg/m^3$
Dynamic Viscosity	1.475×10^{-7} kg/m. s
Speed of Sound	$301.7\,m/s$
Temperature	$226.5\,K$

Table 6.7: Atmospheric conditions at 30km altitude [23]

The cylinder forming the wing can be modelled as a blunt body at an angle to the flow. We can therefore simplify the shock relations by taking the normal component of the incident Mach number, and using the resulting Mach number to predict conditions across the detached shock that will be formed by the cylinder (region B in Figure 6-22).

$$M_{n,A} = M_A \cos\theta \qquad 6.1$$

$M_{n,A}$ in Equation 6.1 is the component of M_∞ normal to the cylinder, and θ is the wing sweep angle. We can calculate the change in conditions across the shock from the oblique shock relations[30]:

$$\frac{\rho_B}{\rho_A} = \frac{(\gamma+1)M_{n,A}^2}{(\gamma-1)M_{n,A}^2+2}$$

$$\frac{p_B}{p_A} = 1 + \frac{2\gamma}{\gamma+1}\left(M_{n,A}^2 - 1\right) \qquad 6.2^{31}$$

$$M_{n,B}^2 = \frac{M_{n,A}^2 + [2/(\gamma-1)]}{[2\,\gamma/(\gamma-1)]M_{n,A}^2 - 1}$$

Taking the ideal gas relationship $\frac{T_B}{T_A} = \frac{p_B}{p_A}\frac{\rho_A}{\rho_B}$ we can furthermore obtain the temperature rise immediately after the shock. Solving the above solutions for a Mach 8 flow through air yields the relative changes in pressure, temperature and density. By multiplying these relative values by the freestream conditions at Mach 8 and 30km altitude based on the US Standard Atmosphere data (as above), we can obtain the absolute values of temperature, pressure, density and Mach number directly behind the bow shock. These are shown for a range of sweep angles in Figure 6-23.

[30] For a review and derivation of these principles see reference [24]

[31] γ denotes the ratio of specific heats and is assumed to be 1.4 for air.

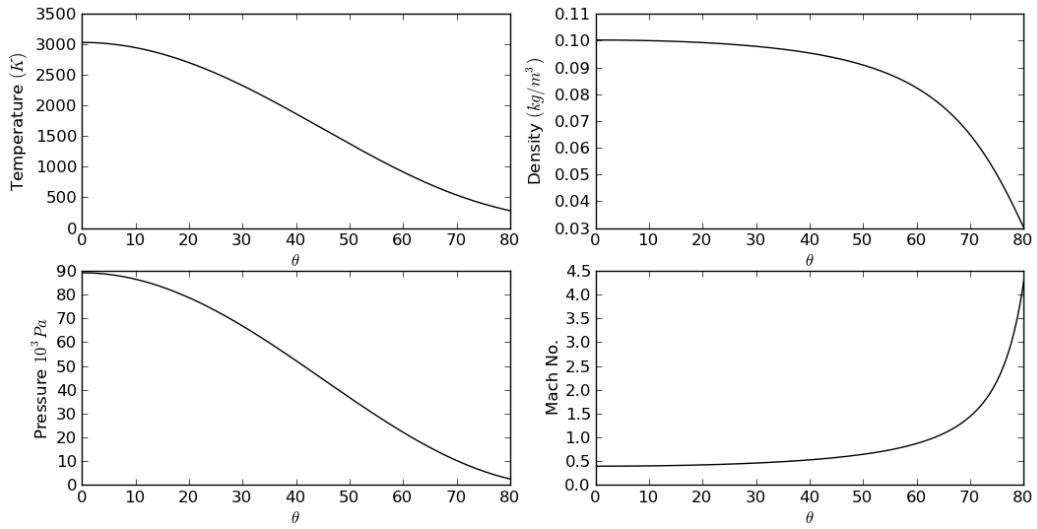

Figure 6-23: Analytical approximation of absolute conditions behind the bow shock of a swept wedge at varying sweep angles at a flow speed of Mach 8, with γ=1.4 and based on the 1976 US Standard atmosphere conditions for 30km altitude.

While it is not possible to solve for the precise heating profile along the wing due to the complex interactions at the wing root, it is possible to estimate the expected magnitude of heat flux at large distance from the root of the wing. At this limit, the heat flux will be equal to that of an infinite cylinder at a corresponding sweep angle. Analytical solutions for precisely such a scenario were derived and experimentally confirmed by Beckwith [15].

In order to produce an approximation for heat flux on the cylinder far from the flat plate, we will use the semi-empirical relations obtained by Beckwith[32], where the derivative of boundary layer edge velocity with respect to distance at the stagnation point, $\frac{du_e}{dx}$ is approximated as per Equation 2.8.

The wall enthalpy is derived for a specific heat capacity of 1000 $J.kg^{-1}.K^{-1}$ for air with a wall temperature of 300 K.

Just as we cannot analytically predict the heating rate near the flat plate for the wing, we also cannot easily predict the heating rates that the flat plate will likely experience near the wing-root interaction zone[33]. However, for flow substantially upstream of this interaction, the model is essentially a flat plate with a sharp leading edge; among one of the simplest hypersonic flow topologies.

[32] The Beckwith solution to stagnation heat flux on a swept cylinder in hypersonic flow is given in Equation 2.10.
[33] The wing-root interaction zone is shown conceptually in region B of Figure 6-22.

Experimental flat plate heating results are therefore simply compared to the Van Driest solutions for flat plates, using Equation 2.4 with Stanton number and recovery factor values modified for laminar or turbulent cases, as discussed in sections 2.1.1 and 2.1.2 respectively.

By solving for the skin friction coefficient using Equation 2.6 and solving for heat transfer using Equation 2.4, we obtain a turbulent heat transfer of $4.85 \times 10^3 W/m^2$ at a distance of 175mm from the leading edge of the flat plate (the location of the first thin film gauge recess) at Mach 8 and 30km altitude based on US Standard Atmosphere data [23][34].

[34] Refer to Appendix Section 6.4.2 for the numerical code and root-finding algorithm implemented to produce that solution (as well as all turbulent heat transfer analytical solutions used in Section 0).

6.4 Code

This section contains relevant code snippets referenced within the report. It does not represent the entire code base constructed or utilised throughout the study, but simply shows some of the numerical representations of analytical relationships that were utilised in the analysis.

6.4.1 beckwith_function.py

```
# This function produces a heat flux approximation at the stagnation point of a swept
# cylinder as per the turbulent stagnation point heating equation by Beckwith (1962).

# All units are SI unless specified otherwise.

# import relevant libraries
import math
import matplotlib.pyplot as plt

# import the stagnation properties and normal shock relations functions used in this script
from stagnation_properties import *
from normal_shock_relations import *
from sutherland_viscosity import *

# immutable constants
gamma = 1.4 # Specific heat ratio for air
R = 287.035 # Gas constant for Air


# Input parameters:
# a      - Free Stream Speed of Sound (m/s)
# M      - Free Stream Mach number
# mu     - Free Stream Dynamic Viscosity (kg/m.s)
# nu     - Free Stream Kinematic Viscosity (m^2/s)
# p      - Free Stream Pressure (Pa)
# Pr     - Prandtl number
# radius - Cylinder radius (m)
# rho    - Free Stream Density (kg/m^3)
# T      - Free Stream Temperature (K)
# T_w    - Wall Temperature (K)
# theta  - Sweep angle (radians)

def beckwith_turbulent_stagnation_heat_flux(a,M,mu,nu,p,Pr,radius,rho,T,T_w,theta) :
    # Free stream velocity
    u = M * a

    # Other relevant constants
    C_p_air = R * gamma / (gamma-1)  # Heat capacity of air at constant pressure

    # Wing diameter - reference length for Beckwith (1962) turbulent heat flux equation
    D = 2*radius

    # freestream stagnation conditions
    T_0 = T * T_rise_stag(M)
    mu_0 = mu_suth(T_0)
    rho_0 = rho*rho_rise_stag(M)

    # Blasius skin friction parameters
    alpha = 0.0228 # Blasius skin-friction coefficient - for Equation 3 in Beckwith (1962)
    n = 4.0 # Blasius skin-friction exponent - for equation 3 in Beckwith (1962)

    # normal component of freestream mach number
    Mn = M * math.cos(theta)

    # freestream chordwise velocity
    u_chordwise = u * math.sin(theta)
```

```
# freestream resultant velocity as per u_R in beckwith
# (free stream velocity in cartesian coordinates)
u_R = u

# conditions immediately behind the bow shock (denoted as per beckwith (1962) by _1
# suffix) the assumption here is that each property can be approximated behind the

# bow shock by the rise from a normal shock at mach number Mn (the normal component
# freestream mach number to the bow shock)
Mn_1 = M_shock(Mn)
rho_1 = rho_rise_normal_shock(Mn) * rho
p_1 = p_rise_normal_shock(Mn) * p
T_1 = T_rise_normal_shock(Mn) * T
mu_1 = mu_suth(T_1)
nu_1 = mu_1/rho_1

# stagnation line conditions (denoted by suffix _s in Beckwith  (1962) and defined
# as the conditions at the stagnation line but at the edge of the prevailing boundary
# layer). Calculated here simply as the stagnated conditions of region 1 (immediately
# behind the bow shock)
rho_1_s = rho_rise_stag(Mn_1) * rho_1
p_1_s = p_rise_stag(Mn_1) * p_1
T_1_s = T_rise_stag(Mn_1) * T_1
mu_1_s = mu_suth(T_1_s)

# Reference conditions (as per Beckwith (1962) these are taken at the wall)
T_r = T_w
mu_r = mu_suth(T_r)

# derivative of chordwise velocity w.r.t spanwise position at region 1.
du_dx = (1/radius) * ( 2.0 * (p_1_s - p_1) / rho_1_s) ** 0.5

# Now work out the turbulent Nusselt number based on Beckwith (1962) equation A17
Nu = \
Pr**(1.0/3.0) * \
( (u_R * D / nu)**(n/(1+n)) ) * \
( (alpha * (p_1_s / p) * (mu_r/mu_0) * (T/T_r)) ** (n/(1+n)) ) * \
( math.sin(theta) ** ((n-1)/(n+1)) ) * \
( (49.0/376.0) * (mu_0/mu) * math.cos(theta) * (D/u) * du_dx) ** (1/(1+n))

# get the thermal conductvity of the air (calorially perfect gas)
k = mu * C_p_air / 0.7

# adiabatic wall temperature is the boundary layer temperature
T_aw = T_1_s

# heat flux is therefore:
q_w = Nu * k * (T_aw - T_w) / D * 1e-6 # (W/m^2)

return q_w
```

6.4.2 get_van_driest_turbulent_cf.py

```
# This function solves for the skin friction coefficient in a turbulent boundary layer
# using the Von Karman / Van Driest turbulent boundary layer heating solution
# (Van Driest, 1956)

# import the scipy library
import scipy
import scipy.optimize

# the residal defines the error at which the root finder should stop
residual = 1e-12

gamma = 1.4

def get_van_driest_turbulent_cf(
    M_bound,\ # Boundary layer edge Mach number
    Re_x,\ # Reynolds number
    T_bound,\ # Boundary layer edge temperature
    T_w,\ # Wall temperature
    ):

    # find A_sq, B, alpha and beta as per equation (7) in
    # Van Driest - The Problem of Aerodynamic Heating (1956)
    A_sq = ((gamma-1)/2)*(M_bound**2)/(T_w/T_bound)
    B = (1+(M_bound**2)*(gamma-1)/2)/(T_w/T_bound) - 1
    alpha = (2*A_sq-B)/(B**2+4*A_sq)**0.5
    beta = B/(B**2+4*A_sq)**0.5

    # define the cf function which we will solve for y = 0
    def vd_cf(cf):
        y = 0.242 * (math.asin(alpha) + math.asin(beta)) \
            / ((cf**0.5) * (0.5 * (gamma-1) * M_bound**2)**0.5) - \
            0.42 - math.log(Re_x*cf,10) - \
            0.76 * math.log(T_w / T_bound)

        return y

    # we now use the bisection method to solve for the skin friction coefficient
    return scipy.optimize.bisect(vd_cf,residual, 100)
```

6.4.3 normal_shock_relations.py

```
# Normal shock relations
# (used with galilean transformation in main code to arrive at oblique shock values)

gamma = 1.4

# pressure rise through a normal shock
def p_rise_normal_shock(M):
    return (2*gamma*M**2 - (gamma-1)) / (gamma +1)

# Mach number behind a normal shock
def M_shock(M):
    return ((gamma-1)*M**2+2) / (2*gamma*M**2 - (gamma-1))

# density rise through a normal shock
def rho_rise_normal_shock(M):
    return (gamma+1)*(M**2) / ( ( gamma - 1 ) * (M**2) + 2)

# temperature rise through a normal shock
def T_rise_normal_shock(M):
    return (2*gamma*M**2 - (gamma-1)) * ((gamma-1)*M**2 + 2) / ( (gamma+1)**2 * M**2)
```

6.4.4 stagnation_properties.py

```
# Isentropic/Adiabatic supersonic stagnation relations

gamma = 1.4

# Stagnation temperature rise
def T_rise_stag(M) :
    return 1 + (gamma - 1) * M**2 / 2

# Stagnation pressure rise
def p_rise_stag(M) :
    return (1 + (gamma - 1) * M**2 / 2) ** (gamma / (gamma - 1))

# Stagnation density rise
def rho_rise_stag(M):
    return (1 + (gamma-1) * M**2 / 2) ** (1 / (gamma-1))
```

6.4.5 sutherland_viscosity.py

```
# calculate sutherland dynamic viscosity
def mu_suth(T):
    mu_ref = 1.716e-5 # reference viscosity
    T_ref = 273.15 # reference temperature
    T_suth = 110.4 # Sutherland constant
    C = (mu_ref / (T_ref **(3/2)) ) * (T_ref + T_suth)
    mu = C*(T**(3/2)) / (T+T_suth)
    return mu
```